DESIGN AND OPTIMIZATION OF ^{6}LI NEUTRON-CAPTURE PULSE MODE ION CHAMBER

A Dissertation

by

KIWHAN CHUNG

Submitted to the Office of Graduate Studies of
Texas A&M University
in partial fulfillment of the requirements for the degree of

DOCTOR OF PHILOSOPHY

August 2008

Major Subject: Nuclear Engineering

DESIGN AND OPTIMIZATION OF ^{6}LI NEUTRON-CAPTURE PULSE MODE ION CHAMBER

A Dissertation

by

KIWHAN CHUNG

Submitted to the Office of Graduate Studies of
Texas A&M University
in partial fulfillment of the requirements for the degree of

DOCTOR OF PHILOSOPHY

Approved by:

Chair of Committee,	Leslie A. Braby
Committee Members,	Marvin L. Adams
	John Ford
	Morag K. Smith
	James T. White
Head of Department,	Raymond Juzaitis

August 2008

Major Subject: Nuclear Engineering

ABSTRACT

Design and Optimization of ^{6}Li Neutron-Capture Pulse Mode Ion Chamber.

(August 2008)

Kiwhan Chung, B.A., Berea College;

M.S., Texas A&M University

Chair of Advisory Committee: Dr. Leslie A. Braby

The purpose of this research is to design and optimize the performance of a unique, inexpensive ^{6}Li neutron-capture pulse-mode ion chamber (LiPMIC) for neutron detection that overcomes the fill-gas contamination stemming from outgas of detector components. This research also provides a demonstration of performance of LiPMICs. Simulations performed with GARFIELD, a drift-chamber simulation package for ion transport in an electrostatic field, have shown that argon-methane mixtures of fill-gas allow maintenance of electron drift velocity through a surprisingly wide range of fill-gas content.

During the design stage of LiPMIC development, the thicknesses of lithium metallization layer, the neutron energy conversion site of the detector, and the thickness of neutron moderator, the high-density polyethylene body, are optimized through analytical and MCNPX calculations. Also, a methodology of obtaining the suitable combination of electric field strength, electron drift velocity, and fill-gas mixtures has

been tested and simulated using argon-methane gas mixtures. The LiPMIC is shown to have comparable efficiency to ^{3}He proportional counters at a fraction of cost. Six-month long baseline measurements of overall detector performance shows there is a 3% reduction in total counts for ^{252}Cf sources, which provides a good indicator for the longevity of the detector.

ACKNOWLEDGEMENTS

Sixteen years have passed since I first set foot on the campus of Texas A&M University. I arrived at Texas A&M University as a young, inexperienced adult, and I am now a husband and a proud father of two kids. There are many people who have helped and supported me during my journey at Texas A&M University. I would like to thank my committee chair, Dr. Braby, for his support and for sharing his wealth of knowledge with me through his instruction and his character. I would like to thank my committee members, Dr. Marvin Adams, Dr. John Ford, Dr. Morag Smith, and Dr. James White, for their guidance and support throughout the course of this research. I would to thank Dr. John W. Poston, Sr. for his support and mentoring during my stay at Texas A&M University. I appreciate the candor and wisdom he so freely dispenses to students.

My research would not be possible if Dr. Phyllis Russo and Kiril Ianakiev did not take a chance on me and hire me as a summer intern at the Los Alamos National Laboratory (LANL) in 2002. Not only have they shared with me their technical expertise, but also with their passion for science, and they instilled in me the knowledge that applying science for the safety and security of this country and the world is indeed ethical and noble.

I would like to thank Dr. Morag Smith and Dr. Ed McKigney for their support and guidance during my stay at LANL. My completion of this Ph.D. research would not be possible without their ceaseless support and day-to-day interactions.

I am grateful to Dr. Martyn Swinhoe and Dr. Mark Makela for their participation and for sharing their expertise in my research. I want to thank Dr. Mark A. Nelson for his enduring friendship and assistance at LANL.

I want to thank my parents for believing in me and for their encouragement and prayers. Finally, I want to thank my loving wife for her patience and devotion.

TABLE OF CONTENTS

Page

LIST OF FIGURES

FIGURE Page

FIGURE Page

LIST OF TABLES

1. INTRODUCTION[*]

Ionization chambers have been in use for many decades. They were one of the first types of electrical counting devices used in nuclear physics experiments. While there have been advances in materials and design improvements for many types of radiation detection instruments, ionization chamber designs have more or less remained constant. Despite their historical and stable design, the ionization chambers are seldom used in pulse mode outside the laboratory setting because the output pulse height and resolution are sensitive to changes in gas composition. This research designs and optimizes the performance of a unique, inexpensive ^{6}Li neutron-capture, pulse-mode ion chamber (LiPMIC) for neutron detection that can overcome the fill-gas contamination stemming from outgas of detector parts. This research also provides a demonstration of performance of LiPMICs. Simulations performed with GARFIELD (Veenhof, 2005), a drift-chamber simulation package for ion transport in an electrostatic field, developed in CERN (European Organization for Nuclear Research), have shown that certain mixtures of fill-gas allow maintaining similar electron drift velocity through a surprisingly wide range of fill-gas compositions. This novel pulse-mode ion chamber is specifically

---

This dissertation follows the style of *Radiation Measurements*.

[*] Part of this section is reprinted with permission from 1) "Homeland security instrumentation for radiation detection at seaports." by Richard Kouzes, 2003. Pacific Northwest National Laboratory Report PNNL-SA-43032, Copyright [2003] by Richard Kouzes; 2) "Mitigation of outgas effects in the neutron-capture ^{6}Li pulse-mode ionization chamber operation." by Kiwhan Chung, Kiril Inakiev, Martyn Swinhoe, Mark Makela, 2005. IEEE Nuclear Science Symposium Conference Record. 3, 1255-1257, Copyright [2005] by IEEE.

designed as one of several cost-effective instruments that have the potential to fulfill the needs for large-scale deployment in a distributed network of remote sensors.

1.1 Motivation and application

The currently available detectors do not allow a large-scale detection capability even at a minimal number of ports of entry for both personnel and goods due to economic constraints imposed by the very high initial procurement and operational costs associated with the detectors. Even a small deployment scale in the order of tens of radiation detectors in traditional deployments can mount very high initial procurement costs. The LiPMIC is expected to allow neutron detection capability for deployment for homeland security and nuclear material control and accountability applications at a performance level comparable to the currently available neutron detectors, such as ^{3}He gas proportional counters (HeGPC), while reducing the initial procurement cost by an order of magnitude (Ianakiev and Swinhoe, 2002). The detector is expected to provide non-invasive interrogation of goods and personnel at borders, ports, strategic landmarks, and buildings for detecting nuclear materials such as plutonium. Fig. 1 shows the porosity of the physical border for the flow of people and goods into the US. The US border has 307 ports of entry where 330,000 cars, 60,000 commercial trucks and containers, 2500 aircraft, and 600 vessels transit daily. The porous US-Canada and US-Mexico borders are targeted for clandestine and illicit activities, and are a major concern in a complex equation of homeland security and counterterrorism (National Commission on Terrorist

Attacks, 2004). The general framework for developing such a detector is repeatedly described in the Objectives 2.1 and 2.3 of the Department of Homeland Security (DHS, 2004a). The objectives state, “Provide operational end users with the technology and capabilities to detect and prevent terrorist attacks, means of terrorism….” The implementation statement in the mission of Office of Defense Nuclear Nonproliferation of the National Nuclear Security Administration (NNSA, 2004) states, “Detects nuclear proliferation and illicit nuclear and radiological trafficking by conducting cutting-edge research and development….” More specifically, the need for a neutron detector platform that is economically feasible for a very large-scale deployment has been stated by a strategic objective of the Office of Science and Technology in the Department of Homeland Security (DHS, 2004b):

> *Develop and deploy state-of-the art, high-performance, low-operating-cost systems to prevent, detect, and mitigate the consequences of chemical, biological, radiological, nuclear, and explosive attacks….*

Detecting illicit nuclear materials before they reach the US soil is considered the primary task for the LiPMICs, but a huge potential exists in domestic safeguard applications. An array of LiPMICs can be installed permanently around the perimeter of and at the site of strategic landmarks, federal buildings, nuclear power plants, and US military bases worldwide. If there is a special event, temporary installation around the site can be maintained for the duration of the event to provide a non-invasive surveillance of the surroundings.

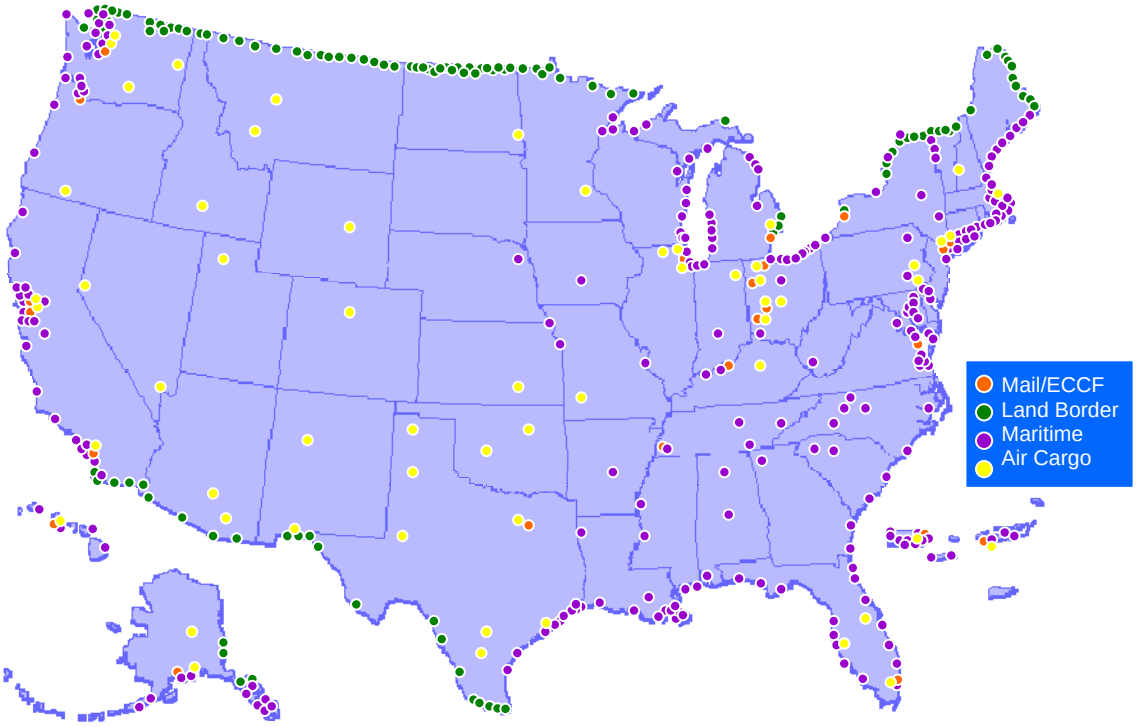

Fig. 1. Various entry points for goods and people to the United States. Copyright [2003] by Richard Kouzes.

1.2 General description of the detector

Fig. 2 is a diagram of a single-cell ion chamber prototype. The high-density polyethylene (HDPE) body is put together as two machined parts and moderates source neutrons to thermal energy range via elastic collisions with hydrogen and carbon nuclei. Ion chambers detect radiation by collecting ion-electron pairs produced from the interactions between radiation and fill-gas atoms. For most neutron detectors there is an intermediate conversion process where the incident neutron energy is converted to charged particles. For LiPMICs incident neutrons are thermalized in the HDPE and interact with ^{6}Li atoms in the metal (depicted with green line in Fig. 2) applied on a nickel-copper substrate

surface (depicted with red line in Fig. 2) which also acts as cathode, and produce the primary charged particles, in a back-to-back geometry, from the $^{6}Li(n,\alpha)^{3}H$ interactions. The resultant primary charged particles, tritons and alpha particles, interact with argon gas atoms and produce electrons and argon ions, the electronic signal carriers. The metal substrate is applied to the bare HDPE walls by proven technologies such as physical vacuum deposition and is less than 10 μm thick. The two HDPE pieces are bolted together with metal rods and are sealed with a gasket at the interface of the HDPE pieces. The chamber contains an argon gas mixture at 1 standard pressure (atm). The prototype chamber is equipped with two gas pipes so that the gas can be changed for measurements with different fill-gas combinations.

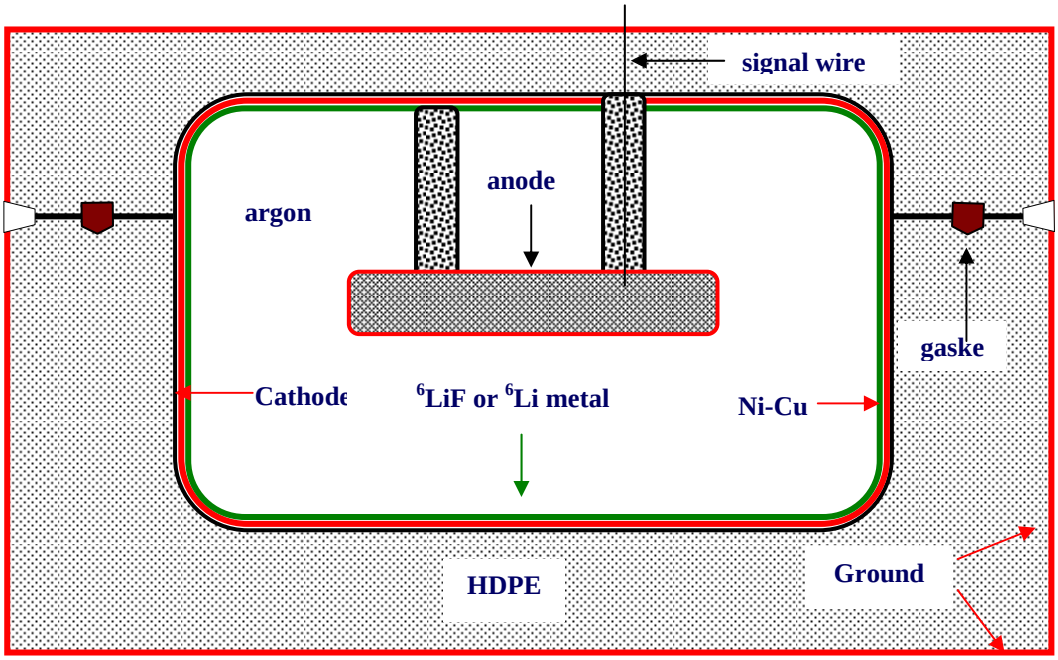

Fig. 2. Design of a single cell prototype. Copyright [2005] by IEEE.

The objective of lowering the initial procurement cost is reflected in the ion chamber design as it relies on readily available mass-production technology as well as utilizing some cost-saving design features in the manufacturing processes. This design of the ion chamber uses HDPE, which serves multiple purposes as the moderator, electrical insulator, and airtight physical shell, as its body, with metallized layer to provide a molecular barrier against possible outgas from the HDPE. A ^{6}Li layer overlaid inside the metallized layer serves as the production site of primary charged particles from thermal neutron interactions. Detailed design work within this context has brought up the issue of mitigating the gasses released from HDPE and other parts inside the active volume of the chamber.

Some of desirable design characteristics are high interaction probability with thermal neutrons to maximize detection efficiency, low gamma sensitivity to disregard environmental and intentional interference from gamma sources, compact size for rapid deployment and easy setup, and continuous operability for several years. Portability and ease of setup are important aspects of the ion chamber because it is intended for quick deployment as needs arise at remote locations. For some deployments, the detectors are expected to be left for long-term remote monitoring, and the lifetime of the ion chambers have been estimated as 10 years because of a limitation imposed upon the detector design by the outgas characteristics of HDPE.

The suppression of gamma signals and increasing neutron detection efficiency are sometimes two opposing goals and detector developers have to find a common ground where the design and operational specifications are mutually satisfied. To maximize the neutron detection efficiency the total neutron counting method, counting both energetic source and thermal neutrons, is used instead of a neutron spectroscopic method. The main difference between the two methods is that a neutron spectrometer has the source neutron interacting directly in the detector volume and can have a direct measurement of the neutron energy spectrum. While this method obtains the energy information of the source neutron, the interaction probability is orders of magnitude low than the thermal neutron interaction probability for most neutron-sensitive materials that it is not always feasible to use this method for concealed nuclear materials. For example, 1 MeV neutron has the total absorption cross section of 0.23 barn, whereas a thermal neutron has 937 barn (Kinsey, 1979). The reduction in the number of thermal neutrons from a shielded source can be compensated by deploying more detectors, which is possible due to the low initial procurement cost of LiPMICs, covering more area where stray thermal neutrons are detected. The total neutron counting method is applied when the neutron energy information is not necessary, or neutron source activity is so low that it can be masked in the natural radiation background. The information for source neutron energy is lost due to repeated interactions in moderator volume, but this method can indicate the presence of nuclear material other than the natural background by detecting larger than normal number of thermal neutrons. The LiPMICs are designed as the first method of

interrogation and rapid, reliable detection of thermal neutron levels above a set threshold can facilitate the flow of commerce and people with minimal interruption.

For LiPMICs additional suppression of gamma signal is not necessary because the atomic composition of LiPMIC is mostly hydrogen, carbon, and lithium so that the interaction probability of gamma rays is considerably lower than any other neutron detector. Other conventional thermal neutron detectors such as ^{3}He proportional counters have considerable metal components such as counter chamber walls and the heavier Z materials have higher interaction probability with gamma rays. The energetic gamma rays expend little energy in the low-pressure argon, and what little energy is expended in the gas is registered in the lower energy portion of the spectrum. This portion of the energy spectrum partially overlaps with electronic noise and will be discarded, before summing up the counts, by using a low energy threshold that minimizes discarding valuable neutron counts. The exothermic interaction with thermal neutron and ^{6}Li nuclei produces 4.8 MeV of combined energy in the detector volume for every neutron conversion. Because of the back-to-back geometry of the primary charged particle production, the entire energy will not be deposited in the detector volume and on the average, close to a half, 2.4 MeV, will be transferred to signal carriers for full-energy deposition episode. The difference in the energy deposition level is enough that the separation of gamma-ray-induced signal from neutron-induced signal is achieved with 95% of the region of interest.

1.3 Competing technologies

Currently, several detector types compete to fulfill the large-scale deployment needs; however, none combines the economic feasibility, performance expectation, and operational continuity better than LiPMICs. The comparable neutron counting systems to LiPMICs are largely divided into two groups: proportional counters and scintillators. For gas proportional counters, there are ^{3}He proportional counters, high-pressure hydrogen recoil proportional counters, and BF_3 proportional counters. For scintillators, there are neutron-converter loaded organic scintillators. Other types of neutron detectors such as ^{6}Li fiber scintillators are yet to be deployed in the field due to various limiting factors; for the fiber scintillator, it's the long decay time of the pulse that requires an unusual pulse processing technique (Specter et al., 1993).

In general, proportional counters achieve their greater sensitivity by amplifying the signal carriers via gas multiplication in the order of 10^3 to 10^6. So far, this additional performance gain has not offset the cost of fabrication, complexity, and sensitivity toward the pressure and composition of the fill-gas. These factors become considerable disadvantages when the detectors are intended for unattended, large-scale deployment. To keep the pressure and composition of the fill-gas in the optimal operational conditions, the fill-gas is usually purged or reconditioned through filters to keep the contaminant concentration within the design specification. This method is achievable in a laboratory, but performing this type of maintenance and operational support in a large-scale field deployment would be prohibitively costly. Another approach to prevent fill-

gas contamination is to fabricate a detector body that is completely sealed off from the contaminants and environment. A conventional fabrication process of ^{3}He proportional counters takes this approach. It takes a series of high vacuum pumping and baking of the detector interior, high voltage insulation at the endcaps, and anode and cathode are assembled and attached in the manufacturing processes to ensure the longevity of the detector operation. This design concept has been proven in many years of operation, and ^{3}He proportional counters have become the de-facto standard of the thermal neutron counting. However, the engineering tasks mentioned to prevent fill-gas contamination, leakage current, uneven static electric field strength, and the restrictive supply of ^{3}He gases worldwide as raw material all contribute to keeping the overall cost of ^{3}He proportional counters prohibitively expensive for large-scale deployment.

The high-pressure hydrogen proportional counters are a type of gas recoil proportional counters that is designed to increase fast neutron interaction probability with the hydrogen-rich fill-gas. Because of the similarity of the mass of incident neutrons and protons, a neutron can transfer its entire energy to the hydrogen nucleus, a proton. The recoil protons can be relatively easy to detect with less consideration for gamma-ray discrimination. However, considerably lower cross-sections for fast neutrons, the low gas density, and low stopping power for recoil protons result in overall efficiency of less than 1% (Knoll, 2000, p. 566) and are limiting factors in using the high-pressure recoil proportional counters. Heavier methane gas can be used as an alternative to hydrogen gas. Because the energy transfer ratio is different between hydrogen and carbon target

nuclei, the maximum energy transfer to the recoil carbon nucleus is approximately 21% of the recoil proton (Bennett and Yule, 1972). Other than the fill-gas composition, gas recoil proportional counters share similarities with the gas proportional counters and have the same sensitivity toward the composition of the fill-gas. Due to its low efficiency and sensitive operation, high-pressure recoil proportional counters are not considered suitable for the large-scale deployment.

Boron Trifloride (BF_3) proportional counters use BF_3 gas at equal or less than the atmospheric pressure. In this gas, the neutron conversion occurs at B-10 atoms through (n, α) reactions. The thermal neutron interaction cross-section for ^{10}B is about 4 times larger than that of the $^{6}Li(n, \alpha)^{3}H$ reaction and the potential to have higher efficiency than LiPMICs exists. While BF_3 is chosen for its high neutron interaction probability of ^{10}B, and overall quality as the proportional counter gas, the molecular makeup of the gas poses problems in the end. The breakdown of BF_3 molecules liberates three fluorine atoms, which have high electron affinity. Free fluorine atoms in the fill-gas volume recombine with electrons and effectively reduce the pulse height amplitude of the signal.

Organic, liquid, and plastic scintillators are other types of detectors that can be used to detect fast neutrons. These scintillating materials are derivatives of pure organic crystals such as anthracene and stilbene. Anthracene has the distinction of having the highest scintillation yield among organic scintillators. However, due to fragility and difficulty in obtaining large sizes, these crystals are not used effectively in pure form. Because the

light photons, the initial signal carriers from radiation interactions, are produced as results of transitions in the energy states in the atoms and not in the lattices, the crystals can be dissolved in a chemical solvent and still maintain their scintillation properties in interacting with ionizing radiation. This development solved the limitation on the crystal size and the varying scintillation yield resulted from incident radiation's orientation with respect to crystal axis. In pure crystal, the scintillation yield can vary by 20-30% depending on the orientation of incident radiation (Knoll, 2000 p. 223). For a liquid scintillator, a unique method of covering all angles of incident radiation is possible: it can submerge samples in its volume during the analysis, capable of reaching 100% counting efficiency. This is particularly useful in counting low-energy beta emitters often found in environmental samples. The liquid scintillators are packaged in a sealed container purged of oxygen because the oxygen present in liquid volume can work as a quenching agent and reduce the photon yield.

Plastic scintillators are developed to allow more stability in material and easier handling of the scintillators while maintaining the scintillation properties unchanged. The plastic scintillators can be considered as organic crystals dissolved in solvent that can be polymerized. Popular solvents used for the polymerization process are styrene, polyvinyltoluene or polymethyl-methacrylate. Plastic scintillators can be fabricated into large, different shapes inexpensively. As the size becomes increasingly large, photon loss within the scintillators needs to be addressed. The use of these scintillators for fast neutron detection is possible, throughout the changes in their physical forms, due to their

hydrogen rich compounds and subsequent prolific production of photons after the neutron-hydrogen interactions. The densely populated hydrogen atoms in liquid or plastic scintillators interact with incident neutrons and the recoil protons expend all their energy in the material within a small radius of interaction sites. The proton recoil scintillators, usually liquid or plastic scintillators, have fast response and are relatively inexpensive.

Unfortunately, extracting pulses of interest may not be straightforward in scintillators because of an intrinsic property of organic scintillators in general. The prompt fluorescence accounts for the vast majority of the signals; however, the delayed fluorescence, is also present. While the delayed fluorescence is a small proportion of the yield, the delayed fluorescence cannot be ignored because its fraction in overall scintillation yield depends on the type of incident radiation (Knoll, 2000 p. 230). For example, the contribution from delayed fluorescence in the scintillation pulses induced from gamma particles as opposed to alpha particles is markedly different. Fortunately, this distinction is useful in eliminating pulses from a certain type of incident radiation entirely using pulse height discrimination. Because of this property of the material, pulse shape discrimination is used to differentiate the origin of pulses and eliminate unwanted pulses.

Employing the advantages of organic, liquid, and plastic scintillators for detection of thermal neutrons, however, would require additional factor. As with other thermal

neutron detectors, the performance of the scintillators can be maximized by adding an element with high thermal neutron cross section such as boron, lithium, and gadolinium. For detection of thermal neutrons, boron is added to plastic scintillators to enhance the thermal neutron interaction probability. While the high density relative to BF_3 is a definite advantage, it has its own share of shortcomings. The optical quality of the plastic scintillators loaded with boron is opaque, and the rate of light yield increase decreases as the scintillator increases in size and as boron concentration increases. Some organic scintillators have much higher scintillation yield per unit energy from prompt fluorescence by secondary electrons of gamma rays than that by recoil protons (Knoll, 2000 p. 565). This behavior is compounded by the density difference between scintillators and gases such as BF_3 used for thermal neutron detection. The dense scintillators allow full energy deposition from secondary electrons produced by gamma rays, whereas in gas detectors the secondary electrons easily escaped the active volume of detectors. The clear pulse height difference between gamma-ray induced pulses and neutron-induced pulses is no longer observed and pulse shape discrimination must be employed to distinguish pulses.

Lithium iodide (LiI) is a type of inorganic scintillator for detecting thermal neutrons. When europium is added as an activator, the scintillation yield can reach one third of that of sodium iodide. As with boron loaded plastic scintillators, the dense material characteristics of lithium iodide allows secondary electrons from gamma-rays to deposit their full energy, and this makes differentiating pulses induced by gamma rays more

difficult. Another inorganic scintillator is zinc sulfide activated with silver (ZnS(Ag)). In this compound, lithium fluoride is added to zinc sulfide and mixed in to thin planes. The thickness of 0.6mm for the material allows escapement of secondary electrons from gamma rays and reject pulses that derived from gamma rays easier.

Increased efficiency and inexpensive, robust material to withstand the environmental conditions are some of the advantages of scintillators. While each scintillator unit can increase its active volume, the unit must be connected to a PMT to process the signal. The cost associated with increasing the number of PMTs is comparable to the initial procurement cost of ^{3}He proportional counters. Not only are the PMTs expensive, they also require well-regulated electricity for their operations. PMTs are designed to multiply the original photons into a large number of electrons in well-controlled stages through many dynodes. The dynodes must maintain their electric properties such as voltage and current to amplify the number of electrons. Having this requirement in the remote sites where regulated power sources may not be available could seriously halt the detector operation. As for the proportional counters, a similar demand of high quality power sources exists because their gas multiplication also relies on maintaining specific electric field strength throughout their operation. Also, a rather high initial procurement cost prevents large-scale deployments of proportional counters.

The LiPMICs avoid the crippling fill-gas contamination issues by operating in less sensitive ion chamber mode, and increase its scalability potential by using simple and

inexpensive electronic amplification as opposed to adding expensive photomultiplier tubes for individual detectors. The combination of a robust design, inexpensive material, and fabrication process allows large-scale deployment of LiPMICs.

1.4 Contribution to the scientific body of knowledge

While the driving force behind this research is the cost-effective application potential, the underlying scientific verification of the ion chamber's performance stability with varying fill-gas composition enables such applications. Previous studies of ion chambers and proportional counters recognized outgas from polymers and its effect on the operation of the detectors, and separated sources of outgas from the active volume of the detectors as much as possible. However, motivated by deployment conditions where it is not economically or operationally feasible to maintain the high purity of the fill gas, this research is intended to develop a new detector design that incorporates outgas as a tolerable component of fill-gas so that the ion chamber can operate without interruption of service for an extended period. While it is expected that the majority of outgas for this detector design may come from the HDPE body, other sources such as embedded electronics and gaskets may also contribute to this phenomenon inside the active volume of the ion chamber.

A unique component of the final detector design will be the application of highly reactive ^{6}Li metal. The 95% enriched ^{6}Li metal is a crucial component in this detector as

the thermal neutron capture and primary charged particle production site. Lithium has never been used in its metallic form in radiation detection instruments. Because of its high reactivity when in contact with moisture, it is necessary to maintain the ^{6}Li metal in a moisture-free environment at all times. The specified thickness of 95% ^{6}Li metal is calculated to balance the production rate and escape probability of the primary charged particles after the neutron-^{6}Li interaction. These unique design features are expected to enable the ion chamber to function without maintenance for an extended period. Due to strict safety regulations at the Los Alamos National Laboratory (LANL), where measurements took place, it was not feasible to routinely refill the ^{6}Li metal lined chambers with flammable gases. Most of the proposed experimental measurements are performed with prototypes with non-reactive ^{6}LiF inside. The primary charged particle production rate may be lower in ^{6}LiF than in 95% ^{6}Li metal, but in other areas ^{6}LiF is a safe and adequate replacement material for most activities in this research.

2. ANALYSIS OF POLYETHYLENE

Building a radiation detector requires knowledge of many different academic disciplines. Because one of the main focus of this research is mitigating the outgas effect and optimizing the overall particle detection processes of the ion chamber, understanding the source of outgas from the primary detector constituents, HDPE, and outgas effect on the operation of the ion chambers are crucial. The analysis of the detector is divided into sections following the sequence of interactions leading to neutron detection. The first stage of particle interaction is the energy moderation of source neutrons within HDPE and transport to the interaction sites in ^{6}Li. General and neutronics properties of HDPE are discussed in this section. The second and third stages, the production of primary charged particles resulting from ^{6}Li(n, α)^{3}H reactions, the reaction of secondary charged particles in the gas and the effect of outgas in the process, respectively, will be discussed in the next section.

2.1 Overview of the properties of HDPE

Plastics are ubiquitous today because of ease of processing and their tremendous range in properties such as molecular weight, molecular weight distribution, flexibility, crystallinity, etc. One can conceive a set of properties and can create plastic with a set of properties very similar to the initial requirements. In the beginning, plastics were considered as colloids, which meant that the material was seen as aggregates of

molecules with a particle size of 10-1000 nm diameter. In 1920, H. Staudinger showed that polymers, including plastics, are made up of macromolecules, very long strains of molecules bundled together (Elias, 2003, p. 5).

There are two major types of plastics: thermoplastics and thermosets. Thermoplastics are light molecule-weight polymer whose molecules are not cross-linked. This configuration allows heating of thermoplastics to form liquids, which can be made into different shapes. Thermosets, on the other hand, begin as liquids and are converted to solids by polymerization to form large molecules. Once polymerization has occurred, the material can not be liquefied. If the structure of the molecular chains is random, the polymer is considered amorphous; if the structure of the molecular chains is a regular and ordered, the polymer is considered crystalline. In practice, a polymer can only be semi-crystalline as its limited molecular structure becomes disorderly after extending for a short dimension. Polyethylene (PE) is a type of semicrystalline polymer.

Polyethylene is an industry name for a group of thermoplastics made up of ethylene polymers. Its high-strength, ductility, excellent chemical resistance, low water vapor permeability, low water absorption, and ease of processing contribute to it being the highest volume polymer in the world (Harper, 2000, p. 1.40). PE is used in creating bottles, house wares, toys, food containers, and garbage and grocery bags. The variation in the density of PE, such as very low-density PE (VLDPE), low-density PE (LDPE), linear low-density PE (LLDPE), and high-density PE (HDPE) in this group is caused by

the structure of molecular chains. If the backbone of the chains has a small number of side branches, then the PE will have high-density characteristics. If the backbone of the chains branches out in many directions, then there will be well-developed side branches and the PE will have low-density characteristics (Harper, 2000, p. 1.42). Many additives are incorporated to produce desired characteristics in polymers. Typical additives include are plasticizers, lubricants, anti-aging additives, colorants, flame-retardants, blowing agents, cross-linking agents, and UV protectants. Considering how many different types of additives are used in making of the polymers, even though they are engineered as a stable compound, breakdown of molecules and chains and the eventual release of material components is inevitable. It is fundamental to the operation of LiPMIC to ascertain the types and concentrations of outgas molecules because the outgassing occurs in the active volume of the detector where the signal collection is taking place.

Table 1 is a partial list of general material properties relevant to the research scope. Vicat softening point is the temperature at which a steel rod of 1 mm^2 of cross section moves 1 mm into the material when the steel rod was pushed with 10 N while being heated at a rate of 50 K/hr (Elias, 2003, p. 108). This test would indicate the temperature at which the LiPMIC body would begin to structurally give away. The steel rods aligning the three HDPE body pieces to form an airtight volume can put this type of force to the body. The thermal deflection temperature is the temperature at which the polymer being heated with 120 K/hr bends 0.33 mm under pressure of 66 pounds per

square inch (PSI) (Elias, 2003, p. 109). The dielectric strength of the material indicates the maximum electric field strength the material can operate as an insulator. A higher dielectric strength indicates the material is more electrically insulating. The optimal operating voltage of the detector matrix is approximately 200V and the insulating property of the HDPE will be more than adequate for electrical safety purposes. For the measurement of water absorption property, the samples are submerged in the water for 24 hours and their weight difference was measured. The linear coefficient of thermal expansion shows that the material expands approximately 0.01% of the length. The linear thermal expansion coefficients for aluminum, concrete, and steel all range in 10-20x10^{-6} in/in/C (Incropera and DeWitt, 2001 p. 537) and are about 5-10 times smaller than that of the HDPE linear thermal expansion coefficient. While the scale of expansion is negligible in most laboratory settings, for large-scale deployment in remote operation may become an important factor to consider. The tensile strength of HDPE shows how much tension the material can withstand when pulled apart axially. Compared to metals used in construction, HDPE is approximately ten times weaker (Avallone and Baumeister, 1996, table 6.2.16); however, given the large bulk of HDPE used per detector matrix, HDPE should be able to withstand years of stress from daily operation when treated with average care.

Table 1
Comparison of general material properties of polyethylene (Harper, 2000)

	Test Method (ASTM)	LDPE (Low Density PE)	LLDPE (Linear Low Density PE)	HDPE	UHMWPE (Ultra High Molecular Weight PE)
Density (g/cm^3)	D792	0.917-0.932	0.918-0.940	0.952-0.965	0.94
Vicat Softening Point (F)	D1525	90-102*	80-94*	126-133+	176-277
Thermal Deflection Temp. @ 66 PSI (F)	D648	104-112	NA	175-196	155-180
Melting Point (F)	D3418	208-239	252-255	266-279	257-280
Dielectric Strength (0.125 in thickness, MV/m)	D149	0.45-1.0	NA	0.45-0.50	0.71
H_2O Absorption (% weight) (24hours)	D570	<0.01	<0.01	<0.01	<0.01
Linear Coefficient Thermal Expansion (in/in/C)	D696	100-220 E-6	NA	59-110 E-6	130-200 E-6
Tensile Strength (PSI)	D638	1200-4550	1900-4000	3200-4500	5600-7000

* denotes data from Polymer Data Handbook (Mark, 1999).
+ denotes Kirk-Othmer Encyclopedia of Chemical Technology (Kirk and Othmer, 2001).

2.2 Thermalization of source neutrons in HDPE

The characteristics of HDPE, $-[CH_2CH_2]-_n$, are well exploited in the nuclear industries for its neutron moderating capability. For LiPMIC, HDPE serves a crucial role as a cost-effective bulk material that can withstand long-term use while thermalizing as many source neutrons as possible to facilitate nuclear interaction with lithium-6 atoms on the surface of the metallized HDPE. Neutrons can generally have either absorption or scattering interactions with atoms in material. When a neutron is absorbed in a nucleus, the nucleus cannot contain the excess mass energy of the neutron and eventually releases the energy in various schemes such as emitting gamma ray, charged particles, neutrons,

and fission fragments. From scattering interactions, the nucleus may be left excited, giving off excess energy, and the scattered neutron may change its velocity as a result. In elastic scattering interactions, the total kinetic energy of both neutron and nucleus is conserved; however, neutron will lose its kinetic energy as a function of mass of the nucleus and scattering angle. In each interaction mechanism, the probability of occurrence is measured empirically and is defined as microscopic cross section. This fundamental concept in neutron interaction is discussed in detail in most nuclear engineering textbooks such as Lamarsh and Baratta (2001) and Duderstadt and Hamilton (1976).

In HDPE, source neutrons have mostly elastic scattering interactions with hydrogen nucleus, and the average transfer of energy is about a half of the kinetic energy due to the close mass ratio between a hydrogen nucleus and a neutron. This average transfer of energy is calculated by starting from the conservations laws of kinetic energy and momentum in a two-particle collision. A full derivation of steps shown in this section, which provides the average logarithmic decreasement of energy in a collision, is available in Kaplan (1962).

Using the law of cosines and a relation of momentum and kinetic energy in classic mechanics, an equation for the scattered particle can be obtained as:

$$E = \frac{E_o(A^2 + 1 + 2A\cos\phi)}{(A+1)^2}, \qquad (1)$$

Where E denotes the kinetic energy of the scattered neutron, E_o the energy of incident neutron, A ratio of target nucleus mass to incident neutron mass and is approximated as accurately as the atomic mass number, ϕ is the angle between the target nucleus and incident neutron in the center of mass system. In Eq. (1), when $\phi=0$, the scattered neutron is assuming the same direction of flight as the incident neutron, the energy of the scattered neutron is $E=E_o$, and there is total transfer of energy. When the scattered angle is $\phi=\pi$, the scattered neutron is bouncing back 180 degree to the original direction of the incident neutron and its energy is zero. Using the relation between the scattering angle ϕ in the center of mass system and the scattering angle in the laboratory setting θ, the following expression can be established (Kaplan 1962):

$$\cos\theta = \frac{1 + A\cos\phi}{(1 + A^2 + 2A\cos\phi)^{1/2}}. \tag{2}$$

Then, the average scattering angle can be obtained by integrating the Eq. (2) over the possible range for ϕ, which is from 0 to π. In Eq. (3), a substitution $x = cos\ \phi$ was made to make the integration easier.

$$\begin{aligned}\overline{\cos\theta} &= \frac{1}{4\pi}\int_0^{\pi} \cos\theta 2\pi \sin\phi d\phi \\ &= \frac{1}{2}\int_0^{\pi} \frac{1 + A\cos\phi}{(1 + A^2 + 2A\cos\phi)^{1/2}} \sin\phi d\phi \\ &= \frac{1}{2}\int_{-1}^{1} \frac{1 + Ax}{(1 + A^2 + 2Ax)^{1/2}} dx = \frac{2}{3A}.\end{aligned} \tag{3}$$

Then, the average scattering angle is used to obtain the average energy loss per collision in the logarithm of the neutron energy. The probability of having an incident neutron of

Energy E_o having an energy between E and E+dE, after one collision, can be expressed as (Kaplan, 1962):

$$PdE = \frac{dE}{E_o\left(1-\left(\frac{A-1}{A+1}\right)^2\right)}. \quad (4)$$

The denominator of the Eq. (4) indicates the range E can have after a collision (Kaplan 1962). Also, by definition, the average decrease per collision in the logarithm of the neutron energy is:

$$\xi = \overline{\ln E_o - \ln E} = \overline{\ln \frac{E_o}{E}}. \quad (5)$$

Then, ξ is the product of the difference in logarithmic energy and the probability PdE integrated in full energy range:

$$\xi = \int_{rE_o}^{E_o} \ln\frac{E_o}{E} PdE = \int_{rE_o}^{E_o} \left(\ln\frac{E_o}{E}\right) \Big/ E_o\left(1-[\frac{A-1}{A+1}]^2\right) dE, \quad (6)$$

$$\xi = 1 - \frac{(A-1)^2}{2A}\ln\left(\frac{A+1}{A-1}\right). \quad (7)$$

When A=1 or A approaches infinity, the right side of Eq. (7) becomes indeterminate. By taking the limits of the function, the function reaches 1 when A=1 and 0 when A approaches infinity. As a result, the energy of the source neutron is continuously halved as it goes through elastic interactions with hydrogen in HDPE. For carbon atoms, the average loss of energy per elastic interaction is approximately 16% and requires approximately six times (Kaplan, 1962) more collisions to thermalize source neutrons. In inelastic scattering interactions, a portion of kinetic energy of neutron is spent on

exciting nucleus and consequently the kinetic energy of outgoing neutron is reduced. For hydrogen atoms, the inelastic scattering interactions do not occur because the hydrogen nucleus does not have excited states. For carbon atoms, the inelastic scattering interactions only occur above the threshold energy of 4.44 MeV for the first excited nucleus state (Firestone and Shirley, 1996).

The modes of interaction source neutrons can take at the atomic level have been described so far. However, the scale of interaction involves many moles of material and one needs to discuss the bulk property of material, building on the concept of microscopic and macroscopic cross sections. While the discussion of macroscopic cross section is just as fundamental as the discussion of microscopic cross section, the discussion will be limited to the discussion pertaining to the comparison of bulk property of materials. The bulk property of a material for neutron moderation can be described in terms of two factors, moderating power and ratio, and are built upon the description on the atomic scale. The moderating power is defined as $\xi\Sigma_s$, a product of macroscopic scattering cross section and the average logarithmic decrease in the energy of a scattered neutron in an interaction (Reilly et al., 1992). The moderating power indicates how effective the material is at reducing the neutron energy.

On the other hand, a material is not suitable as a moderator if the material only absorbs neutrons and act as a neutron poison. While this may be desirable for radiation protection and shielding purposes, it is not desirable for radiation detection purposes. To

quantify the tendency of a material being a good moderator as opposed to an absorber, a moderating ratio is conceived. The ratio of thermalized neutrons – neutrons that "survive" the thermalization processes – to the absorbed neutrons is $\xi\Sigma_s/\Sigma_a$, where Σ_a is the macroscopic cross section for absorption interaction. Glasstone and Sesonske (1967) compared several widely used neutron moderators. Water has moderating power (1 eV to 100 keV) of 1.28, heavy water has 0.18, and PE has 3.26, almost three times that of water. For moderating ratio, water has 58, heavy water 21000, and PE 122. Other materials such as helium, beryllium and graphite were examined, also, but in all practicality, PE has a good balance of average logarithmic decrement energy and low macroscopic absorption cross section while keeping the cost of moderation low.

2.3 What is outgas?

An outgas is the "migration of molecules of a chemical from a material into its surroundings" (Fang et al., 1991). Some sources of outgas are intended as additives in or as integral parts of the materials, or left trapped during the production processes; however, as the materials break down through aging processes, such as weathering by ultraviolet radiation and chemical reactions within the bulk material, or through structural failure, components start to come apart and are released molecularly. Other sources such as water vapor, carbon dioxide, and nitrogen, which are abundant in the atmosphere, enter the polymer from the outside, permeate through the structure, and desorb from other surfaces. Outgassing is mostly a slow process that does not provide

visible evidence readily, but its cumulative effects are sometimes obvious. Whether sources of outgas originate within the polymer structure or outside, their migratory processes can be explained in terms of gas dynamics such as the diffusion coefficient, the permeability coefficient, and solubility.

As some chemicals make contact with an exterior surface of polymer, their components are dissolved in the polymer. The dissolution of penetrants, as they are called in the field of polymer science, depends on many variables such as interaction between outgas components and the polymer, concentration, temperature, pressure, particle size of the components, and the morphology of the polymer structure, i.e., the distribution of shapes and sizes of open spaces, which are determined by presence and degree of cross links (Neogi, 1996). The dissolution process reaches a critical point, when the vapor pressures of the penetrant inside the polymer and outside are equalized, and diffusion takes place in the bulk material. Diffusion is defined as a manner of transport of material through random molecular motions (Crank, 1975). As outgas molecules are diffusing through the structure, they may be absorbed back into the structure as sorption process predominates, or slow down by the friction force present in the polymer structure. In general, the diffusion coefficient is a complex function of particle morphology, structure of polymer chains such as composition, crystallinity, and level of cross-linking, and the temperature (Kiparissides et al., 2002). A large-diameter molecule of penetrant would experience high friction as it tries to move its way among the polymer chains. In a semicrystalline polymer, an amorphous part is considered more tolerant for diffusion than the crystalline

part, as the crystalline structure becomes a barrier for the penetrants (Kiparissides et al., 2002). The third parameter, permeability, is considered a product of diffusion and solubility. The diffusion coefficient is a kinetic factor, representing the dynamic process in penetrants and polymer system, while solubility represents the thermodynamic factor in the interaction among penetrants and polymer.

Outgas phenomena are quite common in every day life and their effect on people are sometimes benign or even positive. When a new car is purchased, the car smells like a new car and it is one form of validation for money well spent. What people smell are outgases from volatile organic compounds (VCO) in the interior parts of the car. One informal investigation revealed presence of 75 VCOs in the air inside new cars, with the sources of the outgas varying widely from leather seats and carpet to headliners. Outgas is usually an unintended, undesirable property, which product designers and end users would like to see minimized as much as possible. For electronic parts and materials used in satellites, National Aeronautics and Space Administration (NASA), takes great care to test them for outgas properties in extreme temperatures and in vacuum so that the electrical contacts and parts function as they are meant. Outgas in printed-circuit boards can lead to unstable electrical contacts and make instruments malfunction. If epoxy used to hold parts together outgases and loses its adhesiveness, the result can be irrecoverable in space. For manned missions, outgas characteristics take additional importance because even a trace amount of outgas can accumulate in a closed-air system in a space shuttle or space station and build up to an unhealthy level. To uniformly test electronics

parts, a standardized method of testing for outgassing was introduced as American Society for Testing and Materials (ASTM) E595-84. It has been a widely accepted method, and in its current form as E595-07, revised in 2007, E595 reports the total mass loss (TML) and the mass of collected volatile condensable materials (CVCM) (ASTM, 2007).

For high-energy physics communities, outgassing from the detector interior and the breakdown of fill-gas in gas detectors under intense radiation and electric fields have been identified as a part of aging and have been noted many times (Titov, 2004). With the development of Large Hadron Collider (LHC), gas detectors used in the experiments are exposed to great "hadron fluences up to $10^{15} – 10^{16}$ cm^{-2}" (Titov, 2004). This concern is not limited to European Organization for Nuclear Research (CERN), where the LHC is being built. Particle accelerator energy outputs and luminosity are becoming greater and radiation detectors have to be able to handle the amount of radiation physically and electronically. It has been noted by Charpak et al. (1972), Va'vra (2003) and others that the formation of deposits on electrode surfaces, caused by the breakdown of fill-gas molecules, resulted in abnormal electric field strength near the anode and subsequent degradation of wire chamber performance. Attempts to use different fill-gases such as Ar(Xe)-CF_4-CO_2 and Ar-CO_2-O_2 have been somewhat successful in minimizing the polymerization of electrode surfaces, but brought on other problems such as chemically damaging gold-plated anode wires (Romaniouk et al., 2003; Krivchitch et al., 2003) and

becoming more sensitive to trace amount of silicone compound often found in high vacuum lubricants (Ferguson et al., 2002; Romaniouk et al., 2003; Capeans, 2003).

Another example of outgas comes from liquid. The carbonated beverages, including beer, are packaged in carefully engineered, multi-layer bottles and cans to maintain optimal carbonation and product freshness. For soft drinks, the diffusion and permeation rates of carbon dioxide through the usual packaging of polyethylene terephthalate (PET) are carefully measured to ensure that the consumers do not received bottles of beverages that are depleted of carbonation. For beer, the additional factor of oxygen migration from the outside, which would make beer oxidized and spoiled, requires that they continue to use either aluminum cans or glass bottles. For this reason, the permeation coefficient for oxygen required for beer packaging is 20 times smaller than that of the soft drink (Elias, 2003, p. 90). In this case, the carbonation was under pressure and maintaining the carbonation dissolved in the liquid as long as possible was a deciding factor in choosing the length of shelf life for the products.

2.4 Previous research on gas dynamics in polymers

The diffusion model of gases has been studied for more than two centuries, but the gas dynamics in polymers has been studied for about 60 years. In this time, the advancements in both material science and polymer studies allowed the prolific use of polymers in every day life and at the leading edge of technology. Due to increasing use

of polymers from food packaging to state-of-the-art satellites, the gas dynamics in polymers has been documented very well for the most part. Michaels and Parker (1959) investigated small molecules' dependence on polymer structure using environmental, noncondensable penetrants such as nitrogen, oxygen, and carbon dioxide. The morphology of the polymer samples used in Michaels and Parker's research varied in crystallinity from 43 to 82 per cent. The authors stated that the solubilities obeyed Henry's Law, within the limit proposed by the law. Henry's Law correlates directly the solubility of a penetrant in liquid to the partial pressure of the penetrant in gas. This finding justified and allowed the application of the unsteady-state diffusion equation to isotropic crystalline polymers (Michaels and Parker, 1959). Michaels and Bixler (1961) expanded Michaels and Parker's idea further by testing light hydrocarbon gases such as methane, ethane, propane, etc. For these penetrants, the solubility remained proportional to the ratio of amorphous material present in the bulk material, if the bulk material was considered as having two-phase volume consisting of amorphous and crystalline polymers. In a different journal article, Michaels and Bixler (1961) showed that the diffusion coefficients for carbon dioxide, nitrogen, oxygen, and methane are a function of temperature and crystallinity of the polymer. To incorporate the effect of crystallinity of the polymer, they introduced a geometric impedance factor and a chain immobilization factor. In 1960, Rogers et al. conducted an extensive investigation of gas dynamic properties of 19 organic gases in polyethylene. They concluded that the solubility was an exponential function of sorbed vapor concentration of penetrants and

that the polymer swelling was a factor in increasing the diffusion coefficients for heavy organic gases such n-hexane and n-heptane.

Interesting study with hydrocarbon gases showed that certain hydrocarbon species seems to have little effect on the gas dynamics of another hydrocarbon specie (Robeson and Smith, 1968). This idea was utilized in finding the right mixture of fill-gas so that contamination of fill-gas would be mitigated as much as possible. Robeson and Smith provided an explanation for this phenomenon. Robeson and Smith found that the permeability and diffusion coefficients of ethane-butane mixtures are exponential and linear functions of butane concentration. They attributed this to butane “plasticizing” (Robeson and Smith, 1968) the polymer material preemptively because butane’s solubility is an order of magnitude higher than that of ethane. Li and Long (1969) expanded testing of hydrocarbons and tested for both solubility and permeability of nitrogen and light hydrocarbon gases. They showed that the permeability of liquid and gases in polymer material is dependent on penetrant concentration. Li and Henley (1964) have shown that the permeability is dependent of pressure as long as Henry’s law constant is independent of pressure. The pressure at which Henry’s law constant becomes dependent on pressure was found to be above 120 PSI-absolute (Li and Henley, 1964). Kulkarni and Stern (1983) obtained diffusion and solubility coefficients for carbon dioxide, methane, ethylene, and propane and confirmed that the solubility remained constant, independent of pressure up to 40 atm, and within the Henry’s law limit.

However, some studies have been in disagreement with current established laws, and with previous research. Castro et al. (1987) investigated the solubility of n-butane, n-pentane, n-hexane, and n-heptane vapors in PE as a function of temperature, between 258 and 318 K and up to a relative pressure of 0.95, normalized with the vapor pressure of pure hydrocarbon compounds. In the study, Castro et al. (1987) showed that the solubility is not just dependent on temperature, but also on pressure. To characterize the discrepancy, the authors incorporated molecular weight, temperature, and pressure, into an expression for solubility and the experimental results confirmed the derivation. Perhaps, it is previous investigations such as one performed by Castro et al. (1987) that gave impetus for Mattozzi et al. (2005) to investigate the effect of polymer structure on the diffusion of n-hexane in polyethylene. Mattozzi et al. argued that the low diffusion coefficients of small molecule penetrants in a low-crystalline polymer sample are the result of a different aspect ratio than the one used to characterize the crystal shape used in the Fircke model, which assumes crystals to be oblate spheroids (Mattozzi et al., 2005).

Not all research on gas dynamics has concentrated on the free-volume theory. While free-volume theory has had success in explaining diffusion coefficients of small molecules in amorphous polymers in terms of temperature and the penetrant concentration, Pace and Datyner proposed that the free-volume theory grossly ignored the molecular structure of the polymer-penetrant system. They tried to explain diffusion as physico-chemical properties of polymer-penetrant system. Pace and Datyner

published three articles (1979a, 1979b, and 1979c) in 1979 to establish a statistical mechanical model for diffusion. Lastly, Doong and Ho (1992) sought to combine the best properties of free-volume theory and Pace-Datyner's molecular theory into their own diffusion model. For a comprehensive survey of gas dynamics in polyethylene, Kiparissides et al. (2002), Fang et al. (1991), and Flaconneche and Klopffer (2001) provide a good starting point.

3. ANALYSES OF DETECTOR PHYSICS COMPONENTS*

For the next step in the multiple stages of particle interactions, components of neutron detector physics, including detector-specific variables, are investigated to provide an initial framework on which simulation and experimental work begin. Previously, general, neutronics, and outgas properties of the bulk material of the detector, HDPE, have been described. These findings are largely applicable to the thermalization of source neutrons, and it is appropriate to understand in depth how interactions after the thermalization processes occur in the lithium metallization layer and in the fill-gas. Choosing appropriate designs and components based upon these findings is essential in expediting the detector development process and in optimizing the performance of the detector. Some of the findings discussed in this section are neutron conversion process, heavy charged particle interaction, detector geometry, and fill-gas. The results are then used in creating simulation models for better understanding of the ion chamber performance and are verified with experimental measurements.

* Part of this section is reprinted with permission from "Large area neutron detector based on ^{6}Li ionization chamber with integrated body-moderator of high density polyethylene." by Kiril Ianakiev, Martyn Swinhoe, Kiwhan Chung, Ed McKigney, 2004. IEEE Nuclear Science Symposium. Conference Record. 1, 456-460, Copyright [2004] by IEEE.

3.1 Neutron conversion process and total cross-section

If source neutrons successfully survive elastic collisions with mostly hydrogen and carbon atoms and avoid capture in the HDPE moderator, their energy is reduced to the thermal energy range, which is at the thermal equilibrium with surrounding atoms and molecules. Neutrons are said to be at thermal equilibrium when their energy is calculated to be 0.025 eV at the standard temperature and pressure (STP). At the STP, 1 atm and 273 K, they have the highest probability to interact with elements that can facilitate thermal neutron interactions. Some of the widely used thermal neutron reactions are $^{10}B(n, \alpha)^{7}Li$, $^{6}Li(n, \alpha)^{3}H$, and $^{3}He(n, p)^{3}H$. Thermal neutron interactions are exothermic reactions, and a $^{6}Li(n, \alpha)^{3}H$ reaction produces the highest energy output of the three. The total energy output, Q-value, of 4.8 MeV, 2.1 Mev for α-particle and 2.7 MeV for ^{3}H, allows easier discrimination against gamma emitters such as ^{137}Cs and ^{57}Co. The other two reaction types, $^{10}B(n, \alpha)^{7}Li$, and $^{3}He(n, p)^{3}H$ have the Q-value of 2.8 MeV and 0.76 MeV, respectively. On the other hand, the thermal neutron cross section for ^{6}Li is lowest of the three at 940 barns while ^{10}B and ^{3}He have thermal neutron cross sections at 3840 barns and 5330 barns, respectively. A comparison of thermal neutron cross sections and Q-values associated with the three neutron conversion reactions would seem there is no clear winner among the three; after all, ^{6}Li, having the highest Q-value, has the least probability of interaction at 940 barns. However, if one seeks signs for the presence of neutron emitters, then using a conversion reaction of lower Q-value could allow the neutron-induced pulses to be overwhelmed in a sea of gamma ray pulses. Therefore, one would prefer to have higher Q-value interactions so that even a fewer number of pulses

distinguished from gamma ray pulses in the energy spectrum will indicate unmistakably the presence of neutron emitters.

When thermal neutrons interact with ^{6}Li atoms, they form compound nuclei for a brief moment. Neil Bohr proposed the concept of compound nucleus in 1936 and explained a compound nucleus as a stage in nuclear reactions. Bohr stated that a nuclear reaction occurs in two steps. In the first step, an incident particle is absorbed by the target nucleus and forms a compound nucleus. The incident particle penetrates through the Coulombic barrier of the target nucleus and collides into the surface of the nucleus. In the second step, the compound nucleus is fragmented by ejecting a particle such as proton or neutron and the remaining nucleus. The compound nucleus may exist as long as 10^{-15} to 10^{-14} seconds (Kaplan, 1962 p. 453), and it randomly distributes the kinetic energy of the incident neutron and the binding energies of the constituents of the compound nucleus. This additional energy can be considered as excitation energy and is calculated as the difference between the sum of individual masses of incident neutron and target nucleus and the mass of compound nucleus and the kinetic energy of the incident neutron. For thermal neutron interactions, the kinetic energy of a thermal neutron is negligible. The excitation energy, however, cannot be retained indefinitely, and the compound nucleus breaks into fragments. One interesting note is the range of lifetime of compound nuclei is between 10^{-15} and 10^{-14} seconds. It takes a thermal neutron to cross a radius of a nucleus in approximately $2x10^{-18}$ sec. While the lifetime of the compound nuclei and the thermal neutron crossing of an atomic radius are incredibly short durations, the

compound nucleus stays in existence three orders of magnitude longer after the ‘integration’ of a thermal neutron into a compound nucleus – the thermal neutron crossing the radius of the target nucleus. In this relatively long existence, the compound nucleus shuffles the excitation energy around and stays in the elevated energy state where the excitation energy is withheld for the duration. The virtual state or level of the compound nucleus is the elevated energy state where the compound nucleus is withholding the excitation energy. A virtual level is dissolved when a compound nucleus is broken up by ejecting a nucleon. While the excitation energy is the sum of kinetic energy of the incident neutron and mass excess, the reaction probability depends on the excitation energy matching a virtual level of the compound nucleus. This is because the incident neutron has to penetrate through the Coulombic barrier of the target nucleus, and there are certain values of incident particle energies where the penetration of Coulombic barrier, hence, the formation of a compound nucleus, is more probable than other energy values due to excitation energy resonating with an energy level inside the nucleus.

If a nuclear reaction occurs and a compound nucleus is formed, then the total energy and momentum of the two moving fragments are conserved before and after the fragmentation. Because of the conservation of kinetic energy and momentum, a compound nucleus is broken up into reaction products, the primary charged particles, ^{3}H and α particles, in a 180°, back-to-back geometry where one is likely embedded in the ^{6}Li metallization layer. In this geometry, it is only possible to obtain pulses derived from

one of the two reaction products at a time. Even the surviving primary charged particle may expend some energy escaping from the ^{6}Li metallization layer.

The resonance theory provides an explanation for the physical phenomenon of nuclear interactions, but the concept of cross-section provides an expectation value of the interaction probability. While the individual cross-section can be obtained experimentally, the collective cross section of the detector as a unit, the total cross section, can be obtained from atomic cross section. Based upon MCNPX (Hendricks and McKinney, 2005) simulation and analytical calculation the optimal thickness is found to be approximately 30 μm (The calculation and discussion of the optimal thickness is deferred until SIMULATION section where it is integrated better with the MCNPX (Monte Carlo N-Particle eXtended)optimization process of HDPE thickness). At this thickness, there is only 60% total escape probability for the primary charged particles per incident neutron. This factor is taken into consideration when total cross section is calculated for LiPMIC. The total cross section can be thought of as the collective cross section the detector is presenting to an incident neutron. Total cross section is derived as the following:

$$\begin{aligned} &(Areal\ Density) * (Surface\ Area) = Total\ Mass \\ &(\frac{Total\ Mass}{Mole\ Mass}) * N_A = Number\ of\ Atoms \\ &(Number\ of\ Atoms) * (\frac{Cross\ Section}{Atom}) = Total\ Cross\ Section \quad [cm^2]. \end{aligned} \tag{8}$$

The relationship between total cross section and macroscopic cross section can be established with the following derivation:

$$Total\ Cross\ Section = (\rho * x * A) * \frac{N_A}{M_w} * \sigma$$

$$= \rho \frac{N_A}{M_w} * xA * \sigma = N * V * \sigma \qquad (9)$$

$$= N * \sigma * V = \Sigma_t V.$$

The total cross section is the product of macroscopic cross section and volume of the interaction site. The similar total cross section values shown in Table 2 between HeGPC and LiPMIC indicate that two detectors are not much different from each other on the theoretical limit of interaction probability when a thermal neutron reaches the interaction site. The calculation of total cross section is a little different for HeGPC where the total number of He atoms is derived by the effective volume of the He gas at 4 ATM inside the tube.

Table 2
Interaction parameters for thermal neutron interactions

	^{3}He gas prop. Counter (HeGPC)	^{6}Li neutron-capture pulse mode ion chambers (LiPMIC)
Interaction Site	^{3}He Gas @ 4 ATM @ 30 cm	^{6}Li metal @ 30μm
Interaction mode	^{3}He(n,p)^{3}H	^{6}Li(n,t)^{4}He
Q-value	0.765 MeV	4.8 (t:2.7; α:2.1 MeV)
Thermal neutron cross section	5330 barns	940 barns
Active Area/Vol.	150 cm^3	700 cm^2
Areal density	0.54 mg/cm^2 (thickness =r)	1.38 mg/cm^2
Total reaction cross section	86 cm^2	63* cm^2

*Effective total reaction cross section is the product of total reaction cross section and escape probability (60% @ 30 um of ^{6}Li).

3.2 Charged particle interaction in gas

Because the primary charged particles, ^{3}H and α particles, are emanating from a plane of ^{6}Li metallization layer, and the conservation of momentum and kinetic energy dictates the ejection of the fragments in a 180°, back-to-back geometry, it is inevitable to have one of the particles embedded in the ^{6}Li metallization layer. In addition, depending on the depth of formation of the compound nucleus within the metallization layer, the amount of energy the surviving particle will carry to the active volume of the detector will vary. Swinhoe calculated in an unpublished report in 2003 the ranges of α and ^{3}H particles from $^{6}Li(n, \alpha)^{3}H$ reaction in ^{6}Li metal to be 128 μm and 22 μm, respectively. Contrary to neutrons, the primary charged particles interact with matter mostly through Coulomb forces between the positive charge and the negative charges of the orbital electrons of the surrounding atoms. Heavy charged particles with 100 MeV or higher energy can have inelastic collisions with target nucleus, but the charged particles with such high energy are not encountered through $^{6}Li(n, \alpha)^{3}H$ reactions. Cosmic rays may have protons and subsequently muons that are energetic above 100 MeV, but the background radiation, including the contribution from the cosmic rays, for experiments has been recorded at 2 counts per second, which is statistically insignificant. Hence, it is reasonable to assume that the majority of the energy expenditure of the primary charged particles is with orbital electrons.

As the primary charged particles pass through the active volume, the orbital electrons in the vicinity feel the Coulombic attraction. Varying level of attraction, which is indicated

by the proximity of the interaction between the primary charged particles and the orbital electrons, will effect whether the electron will be stripped away from the atom or just excited to a higher energy level, only to be de-energized to the original energy state later. These interactions influence the primary charged particles to lose velocity in the process. The great mass difference between the primary charged particles and electrons dictates that even the maximum energy transfer to an electron is quite small. However, the primary charged particles interact with numerous electrons simultaneously and the net effect of the simultaneous interactions continuously slows down the particle. Eventually this process ends and the primary charged particles come to a stop. In a detector with a finite dimension, this means some primary charged particles do not expend their full energy in the volume. While collection of full electronic pulses is not usually practiced, designing the thermal neutron detector dimensions to be much smaller than the full range of the primary charged particles increases wall effect to limit full energy deposition and decreases the scale of pulse-height spectrum. This decrease will in fact reduce the efficiency of LiPMICs because pulses registering below a lower energy threshold are discarded as a way to eliminate the contribution from gamma rays and electronic noise.

The charged particle interactions can be classified as soft collisions, hard collisions, and Coulomb force interactions with nucleus. The soft collision occurs when the impact parameter, b, the distance between an incident, charged particle and the center of target atom, is much larger than the atomic radius, a. In this type of interactions, the incident particle interacts with the target atom as a whole, and transfer small amount of energy to

excite or ionize the target atom. This is the most prevalent type of the three, and it accounts for about a half of the energy expended by the charged particles (Attix, 1986, p. 161). The hard collision is a type of interaction where impact parameter is similar to the atomic radius, creating a collision where the incident particle collides with an orbital electron of the target atom. In this collision, the ejected electron absorbs the energy of the incident particle the most and becomes energetic enough to cause additional Coulomb force interactions. This type of electrons is called delta rays and has a short range near the track of the original charged particle. While the delta ray may have a short range, the resultant products from interactions with delta ray may travel some distance. If a delta ray knocks off an inner-shell electron, a characteristic x-ray or Auger electron is produced, and there is no distinction whether they are produced through photon interactions (Attix, 1986, p. 163). Energy expenditure wise, the amount of energy spent in hard collisions is comparable to that of the soft collisions. The third type of interaction is the Coulomb force interactions with nucleus. This occurs when the impact parameter is smaller than the atomic radius. This type of interactions does not happen in significant quantity for the α and ^{3}H particles produced from $^{6}Li(n, \alpha)^{3}H$ interactions because the energies of these particles are not sufficient enough to break through the Coulomb force of the nucleus. This type of interaction is significant for electrons, though. The electrons in close proximity to the nucleus when they interact are deflected elastically for most of the time, and this is the reason for electrons' particularly tortuous path in high-Z materials (Attix, 1986, p. 164).

The modes of interaction for the primary charged particles described previously can now be applied to understand the range and energy loss characteristics of the tritons, the main contributor of the signal pulses. Swinhoe calculated that the pulse contribution from surviving α particles is approximately 25% in the optimized ^{6}Li metallization thickness of 30 μm. If one assumes that a triton emanates from the ^{6}Li metallization without expending its energy, then a 2.7 MeV triton creates on the average 105,000 ion pairs in argon gas at STP. The W value – the average energy expended to create an ion pair – of argon gas at STP has been observed to be 26.3 eV (ICRU, 1979). The triton creates the ion pairs in its range continuously as described by the continuous modes of interaction through Coulomb force. A mean range is the distance where an initial particle count is reduced by one-half in a medium. The mean range of a 2.7 MeV triton is derived to be 6.39+-0.05 cm, based upon an experimental range value of 11.40 +-0.09 mg/cm^2 (Wolke et al., 1963). These values are used in GARFIELD to simulate the gas dynamics in detector models. The distribution of ion pairs along the track of a triton is not uniform. This is related to the stopping power of the argon gas for the triton particles because the stopping power is defined as the differential energy loss for the particle per pathlength traveled. Pathlength is the actual distance a particle travels, and range is the effective penetration depth a particle reaches as it meanders in the medium through various tracks. The mass collision stopping power for a heavy charged particle is defined as the following:

$$\left(\frac{dT}{\rho dx}\right) = k\left[\ln\left(\frac{2m_o c^2 \beta^2 T'_{\max}}{I^2(1-\beta^2)}\right) - 2\beta^2\right], \qquad (10)$$

where $k \equiv \frac{2Cm_o c^2 z^2}{\beta^2}$, $C \equiv \frac{\pi N_A Z}{A} r_o^2$, and (11)

$$T'_{\max} \approx 2m_0 c^2 \left(\frac{\beta^2}{1-\beta^2} \right). \quad (12)$$

As shown in Eq. (10), the mass collision stopping power is dependent on many variables. Constant C is the number of electrons per gram of the medium (Attix, 1986, p. 167). Z is the atomic number of the medium, z is the charge of the incident particle, A is the atomic mass unit of the target atom whose electron the incident particle interacts with, and N_A is the Avogadro's number. β is the velocity in fraction of the speed of light and r_o is the classical electron radius. I is the average excitation potential of the target atom. The influence of medium on the stopping power is present with variables I and Z. As the atomic number A increases the stopping power decreases. Also, as the average excitation potential increases, the stopping power decreases also. The influence of particle charge is addressed with variable z. While the variables are useful in calculating the stopping power of a particle that is traversing through media of different composition, when the particle stays in a medium, then these variables become constant. However, the particle velocity expressed as a fraction of the speed of light changes constantly as it interacts with numerous electrons simultaneously, and the stopping power changes with the changing velocity. The change in stopping power for a 2.7 MeV triton traveling in argon is plotted in Fig. 3 and corresponding ion pair production is plotted in Fig. 4. If one assumes a triton is emanating from the ^{6}Li metallization layer such that it collides with a detector wall without expending its full energy, then one can

assume the accumulation of ion pairs will be lower, also. Hence, the electronic pulses derived from the triton will register in the lower scale than the full energy pulses. This is called wall effect. Another process that prevents full energy deposition is the self-absorption of the primary charge particle as it tries to emanate from the ^{6}Li metallization layer. Because these two processes and the angle at which the primary charged particles emanate, it is not trivial to ascertain which process is responsible for less than full energy deposition. Although it is not necessary to analyze the shape of the spectrum for LiPMICs since they detect total counts of thermal neutrons, one needs to understand the behavior of the detectors and the information being conveyed in a pulse height spectrum.

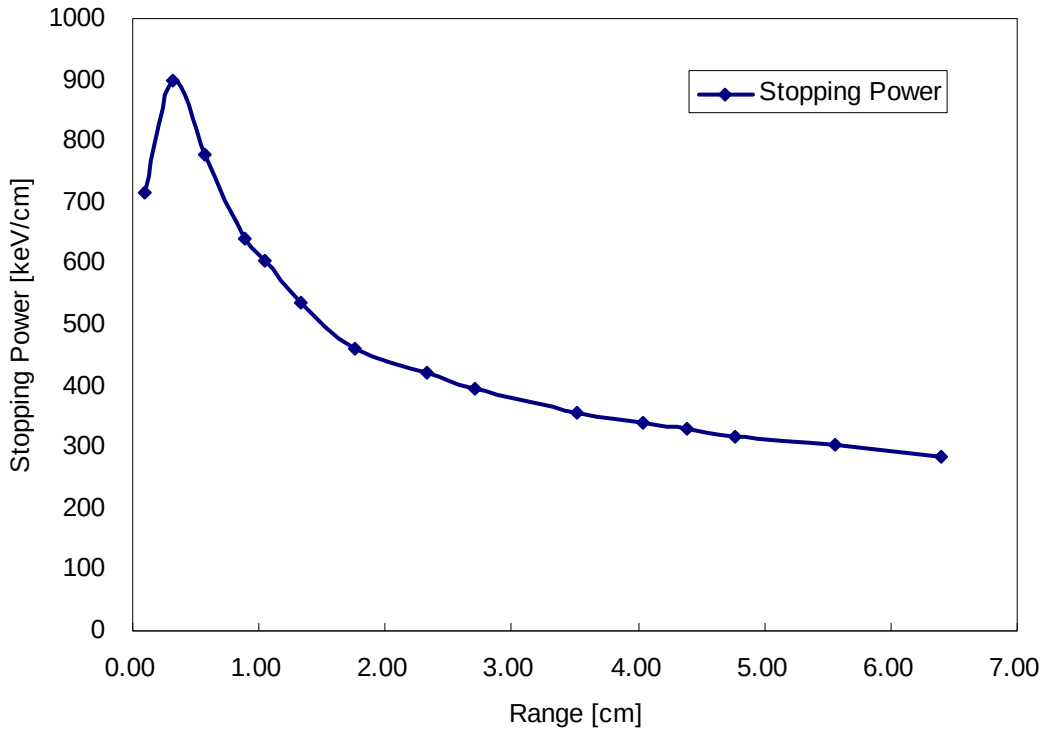

Fig. 3. The stopping power of a 2.7 MeV triton in argon.

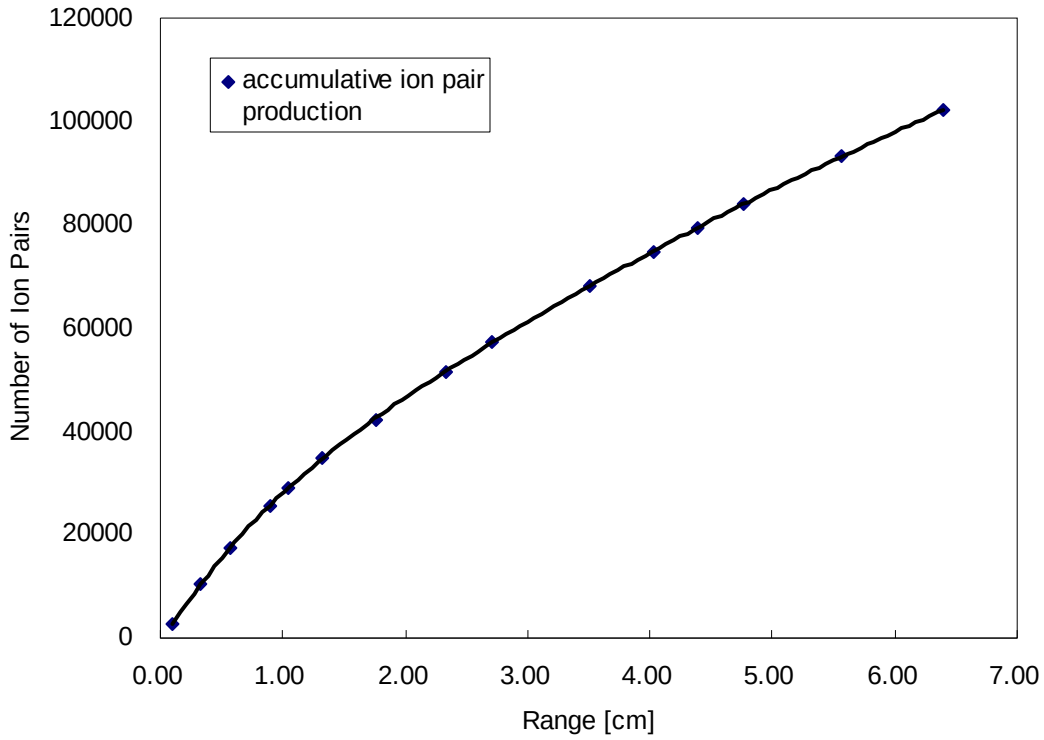

Fig. 4. Accumulative ion pair production for a 2.7 MeV triton in argon.

3.3 Detector geometry and electrode shape

The three main criteria that influence the detector geometry and electrode shape are production and survivability of the α and ^{3}H particles from $^{6}Li(n, \alpha)^{3}H$ interactions, and uniform electric field strength in the active volume of the detector for efficient ionization chamber operation. Ultimately, the detector geometry and the electrode shape are designed to keep the production and survivability of the ion pairs high as much as possible. Unfortunately, there are other issues such as ease and lower cost of fabrication that have to be considered. To provide maximum area of neutron conversion for the detector, several shapes are discussed, but a cuboid shape with rounded corners became

a clear winner for its ease of fabrication and by providing surface area of over 700 cm^2 per cell. The rounded corners were implemented to provide higher survivability of the primary charged particles as they emanate from the corner surface.

Initially, the shape of the anode was a small ball, and the shape of cathode was a deep cuboid vessel. However, this setup was providing electric field strength better suited for the proportional counter mode of operation than ion chamber operation where uniform electric field strength was required. As can be seen in Fig. 5, the quasi-spherical geometry and the shape of electrodes are markedly different from the final single-cell design depicted in Fig. 2. The design in Fig. 2 is a cuboid vessel with a plate suspended in the middle of the volume as the anode. The design (Fig. 5) in the second iteration has electric field strength increasing $1/r^2$ around the anode, and this intensity of the field can match that of a proportional counter. On the other hand, the final detector geometry design shows that all surfaces, with an exception of rounded corners, have a parallel surface at a constant distance so that the electric field strength is uniform in that volume of the detector. It is sufficient to state at this point that keeping the electric field strength uniform so that the electrons drifting toward anode with a minimal, specified velocity is a necessary condition to keep the detector operating within the design specification. Further discussion is deferred to the next section.

Fig. 5. Second iteration of single-cell prototype. Copyright [2004] by IEEE.

3.4 Choice of fill-gas

There are numerous criteria in choosing the composition of fill-gas, which directly influence the ionization and transport phenomena of signal carriers. The first criterion to consider is the W-value, the average energy expended to create an ion pair. As described for different modes of interaction in gas, the W-value is the average energy spent to create an ion pair. In the process, energy spent in creating excitation and delta rays, which trigger additional ionizations on their own, are factored in to increase the W-value. This initial number of conversions from primary charged particles to signal

carriers becomes the foundation of the detector response regardless of how the number of signal carriers is amplified later. Choosing a stable gas medium with a lower W-value is particularly important in spectroscopy because the detector resolution is intrinsically dependent on the average number of ion pairs created by the incident particle. If one operates a proportional counter, then the criteria for fill-gas are longer. Proportional counters often require fill-gas that can operate in low voltage, provide high gas multiplication, proportionality, and withstand high count-rate. Fortunately, LiPMICs do not have to meet these requirements for continuous operation. Because LiPMICs have highly reactive ^{6}Li metallization inside, a noble gas such as argon is a good candidate. Although it is not just argon's unique characteristic, the W-value for argon does not differentiate the type of incident particle. For example, the number of ion pairs created by a 0.51 MeV electron and a proton is nearly the same. This feature is particularly useful for LiPMICs because their pulses are contributed by tritons and alpha particles. The slight disadvantage in using pure argon is that it is somewhat slow, the longer drift time of electrons leads to a longer shaping time, which makes the detector more vulnerable to microphonic interference. Adding other type of gas to speed up the electron drift velocity has other consequences such as increasing the effective W-value of the fill-gas. The W-values of methane are approximately 29 eV for alpha particles and 27 eV for gamma rays, which shows that methane behaves differently with different types of particles.

Choosing a fill-gas often is a balancing act to keep desirable characteristics while reducing other characteristics of a detector. For LiPMICs, the outgas species migrating into the active volume and changing the fill-gas composition is seen as the major obstacle in achieving life expectancy of the detectors.

4. SIMULATIONS*

Having defined and calculated various design components for a single cell detector prototype, simulations are performed using MCNPX, GARFIELD, and OPERA (Vector Fields, 1999). Electrostatic field configuration, neutron interaction rates, and charged particle transport in gas are the three areas where simulation and modeling are necessary for establishing baseline of research and for comparison with the experimental results. Currently, there is no single simulation package that encompasses the several stages of energy conversion from source neutrons to primary signal carriers, electrons. To cover the wide span of the interaction modes, the three major simulation packages are selected for their accuracy and ready adaptability for the research needs.

Performing simulations is an inexpensive and time-efficient way to investigate a wide range of detector responses. The specific tasks for simulations are to evaluate the thicknesses of HDPE in different locations of the detector matrix for optimal thermalization process, to evaluate optimal thickness of ^{6}Li metallization layer for the maximum production of the primary charged particles, and to obtain gas dynamic

* Part of this section is reprinted with permission from 1) "Large area neutron detector based on ^{6}Li ionization chamber with integrated body-moderator of high density polyethylene." by Kiril Ianakiev, Martyn Swinhoe, Kiwhan Chung, Ed McKigney, 2004. IEEE Nuclear Science Symposium. Conference Record. 1, 456-460, Copyright [2004] by IEEE; 2) "Mitigation of outgas effects in the neutron-capture ^{6}Li pulse-mode ionization chamber operation." by Kiwhan Chung, Kiril Inakiev, Martyn Swinhoe, Mark Makela, 2005. IEEE Nuclear Science Symposium Conference Record. 3, 1255-1257, Copyright [2005] by IEEE.

conditions and electric field strength mapping that support maintaining of a range of stable drift velocity throughout changes in the fill-gas composition. The range of simulations duplicates the entire range of transport interactions in reality even though there are disjoints in the chain of simulations. These disjoints are solved by applying analytical calculations. The combination of MCNPX, GARFIELD, and OPERA represents an ensemble of capable simulation packages in their respective fields. MCNPX has been developed by the Los Alamos National Laboratory, and heralded as the de-facto standard in simulating neutron interactions in many different systems such as nuclear reactor fuel rods and radiation therapy using radionuclides. MCNPX has been steadily increasing capabilities by extending applicable energy range, by improving the accuracy of the results by updating to the most recent confirmed nuclear data, and by adding relevant interaction mechanisms such as photonuclear reactions and multiplicity counting of fission neutrons.

The limitation of MCNPX is that its domain of interest mostly lies with neutron interactions. One example of such limitation is that MCNPX does not have the knowledge of what primary charged particles are produced after neutron-^{6}Li interactions. The scope of application for MCNPX terminates with interaction probability in the neutron-^{6}Li reactions; after thermalized neutrons interact with ^{6}Li atoms, the MCNPX does not recognize the products of the interactions and can not simulate the interaction of the primary charged particles with fill-gas atoms. This disconnect is bridged by

performing analytical calculations as McGregor suggested in his detailed analysis published in 2003.

After the thermalization of source neutrons and conversion of thermal neutrons to primary charged particles, the creation of secondary charged particles, namely, the argon ions and electrons are simulated using GARFIELD with analytical assumptions establishing certain parameters. The purposes of using GARFIELD are to find the fill-gas composition at which the electron drift velocity is stabilized and to obtain the time-arrival distribution of signal carriers and their subsequent induced charges. The parameters that influence the electron drift velocity include fill-gas composition, temperature and pressure of fill-gas, and electric field strength. All the conditions can be readily simulated using GARFIELD; however, the electric field strength must be simulated with OPERA, a dedicated electric field simulation program, to make sure the electric field strength present in the complex geometry of the prototype would be accurately characterized. Then, the equivalent field strength is applied in the analytical geometry using the built-in function of GARFIELD. The complexity in the geometry arises in the rounded corners of the cathode and anode and the electric field strength and the finite-element discretization is the mostly widely available method to map the active volume of the detector.

While it would be desirable to have a simulation package that can provide seamless modeling capability for the entire process, taking the strength of each simulation

program, employing it where it is intended for use, and judiciously applying known boundary conditions and analytical calculations produce in accurate and adequate modeling results. These results are verified in experiments.

4.1 ^{6}Li metallization thickness optimization

In order to evaluate the thickness of the ^{6}Li metallization layer for optimal production of the primary charged particles, calculation of optimal HDPE thickness is put aside for later. For ^{6}Li metallization thickness optimization, thermal neutrons are simulated to stream directly to a bare ^{6}Li metallization layer of varying thickness without a HDPE moderator so that source neutrons at thermal energy are arriving at the ^{6}Li metallization layer unimpeded for the maximum interaction probability. This approach may seem unrealistic, but this takes into consideration the purpose of optimization: finding the ^{6}Li thickness that maximizes the production of primary charged particles after interacting with the ^{6}Li atoms. By optimizing the thickness of the ^{6}Li metallization layer first, the result is independent of the effectiveness of the thermalization process in HDPE. This result is then used to evaluate the thicknesses of HDPE in the next step that would bring about similar, if not better, production of the primary charged particles through the efficient thermalization processes within HDPE.

In this series of MCNPX simulations, the thickness of the ^{6}Li metallization layer is varied from 10 to 100 μm to obtain the thickness value that would give the highest

reaction rate. The MCNPX simulations give results in terms of reaction rate per thermal neutron incident upon the ^{6}Li metallization layer. It is understandable to see that the reaction rate increases proportionally with the ^{6}Li metallization layer thickness. As the thickness is increased to 100 μm the reaction rate increases to approximately 28%. This pattern is depicted in blue reaction rate plot in Fig. 6. However, this behavior paints only a half of the picture; one also needs to understand the escape probability of the product particles after the reaction.

After having successfully calculated which thermal neutron interacts in the ^{6}Li metallization, MCNPX doe not have the information about what interaction particles are produced and whether these resultant particles escape through the ^{6}Li layer, which is the value one ultimately desires from these simulations. Hence, the escape probability is calculated analytically. This calculation is performed by Swinhoe in an unpublished report in 2003 and is based upon a study published by McGregor in 2003. The total escape probability (red plot in Fig. 6) – the escape probability of both triton and alpha particles – is inversely proportional to the ^{6}Li metallization layer thickness. Fig. 6 shows the total escape probability is sharply decreased from 90% to less than 50% between 10 to 40 μm, and it does not deteriorate as drastically as the initial reduction to additional thickness of the ^{6}Li metallization layer beyond 50-μm thickness.

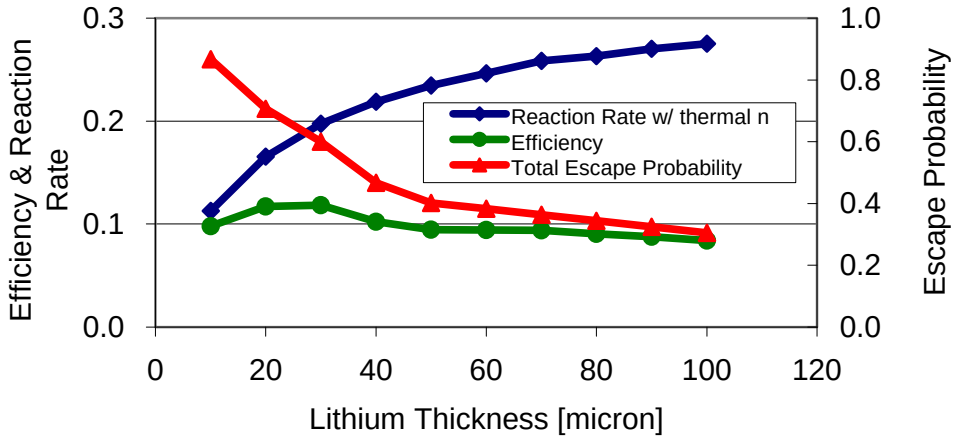

Fig. 6. Reaction rate, total escape probability, and efficiency. Copyright [2004] by IEEE.

According to an unpublished report by Swinhoe in 2003, the individual escape probability of α and ^{3}H particles, shown in Fig. 7, is "the fraction of area of a sphere of radius r that is outside" the ^{6}Li metallization layer. If the interaction site is deeper into the ^{6}Li metallization layer than the range of the triton, for example, then the triton may not escape the ^{6}Li metallization layer regardless of its angle of trajectory. On the other hand, if the neutron interaction site is exactly on the surface of ^{6}Li metallization layer (t=0), then there is one-half probability that the tritons would escape to the active volume. The range of a triton in ^{6}Li is calculated to be 128 μm, and alpha's range is calculated to be 22 μm. The total escape probability has the unit of primary charged particle per reaction. The product (green plot in Fig. 6) of the two values, reaction rate and total escape probability, then, become primary charged particle per incident source neutron, which is effectively the efficiency value. The 10-μm ^{6}Li metallization layer has the highest total escape probability at 90%, but the reaction rate is the lowest at approximately 12%. On the other hand, the 100-μm ^{6}Li metallization layer has the

lowest total escape probability at 30%, but the highest reaction rate at 28%. The product of the two contradicting behaviors come to a maximum value between 20 and 30 μm, where the balance between reaction rate and total escape probability results in the highest efficiency. The ^{6}Li metallization layer thickness between 20 and 30 μm is found to be the optimal thickness for the combination of primary charged particle production rate and its survivability.

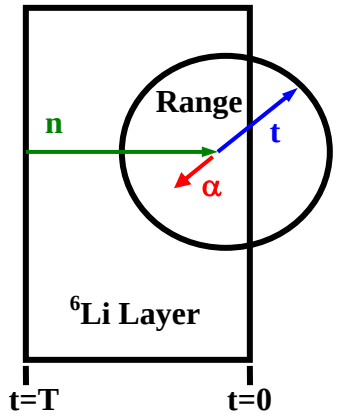

Fig. 7. Simplified diagram of neutron interaction in ^{6}Li and escape of reaction products.

4.2 HDPE thickness optimization

Having optimized the ^{6}Li metallization layer for optimal production of the primary charged particles, HDPE thickness is optimized. It is noted that this series of simulations is performed with a matrix detector of 18 cells (2 layers of 3x3 cells), depicted in Figs. 8 and 9. Other simulations are conducted on a single cell platform; however, because of the thermalization in HDPE influences all detector cells, it is necessary to conduct simulations using a detector array as a basic unit of deployment. Fig. 8 shows different

thickness of HDPE within its structure. There are 5 different locations in HDPE where thickness is be varied. The different parts of HDPE are named as the following:

Front: The closest piece of HDPE facing source neutrons
Interlayer: The piece of HDPE between layers of individual detector cells
Back: The piece of HDPE below the second layer of detector cells
Intercell: The piece of HDPE between individual detector cells in the same layer
Edge: The piece of HDPE around the perimeter of the matrix detector

^{252}Cf is used to provide fission neutrons streaming orthogonally toward the front surface of the detector matrix. The volume outside the detector matrix is defined as vacuum and any source neutrons that scatter out of the detector volume are considered to be lost.

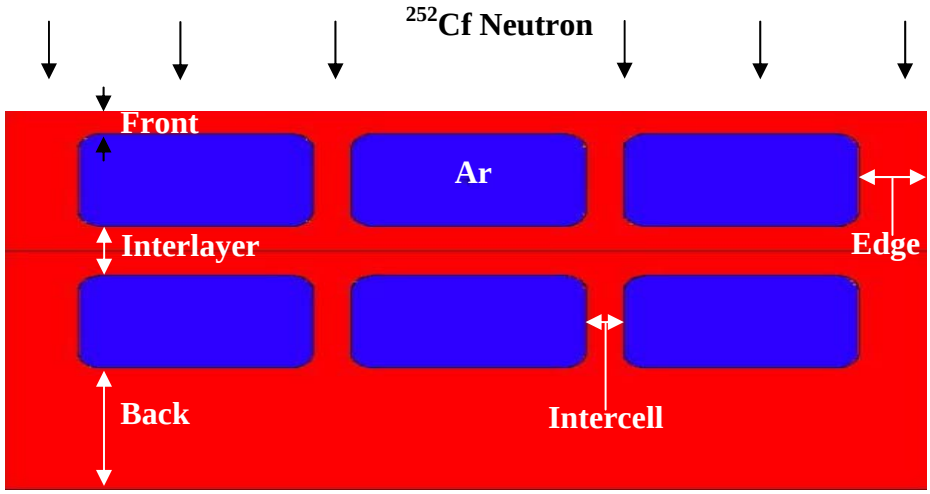

Fig. 8. Diagram of HDPE thickness optimization setup. The source neutrons are streaming down toward the front surface of the detector array orthogonally.

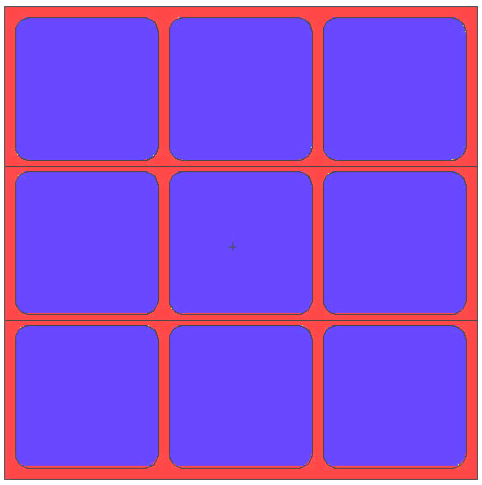

Fig. 9. Top view of detector matrix for simulation setup.

To obtain the change in efficiency as a function of a thickness variable in each series of MCNPX calculation shown in Fig. 10, a thickness variable is varied from 1 cm to 10 cm; for example, the plot labeled ‘Intercell HDPE variation’ in Fig. 10 is obtained by varying the thickness of ‘intercell’ HDPE from 1 to 10 cm, while keeping the rest of the thickness of different parts constant at 1 cm. By applying the same methodology to other variables, the initial optimized set is obtained as 5 cm for front, 10 cm for back, 8 cm for interlayer, and 4 cm for intercell. The first optimized set is tested again by varying the front HDPE thickness. Even though the optimized set of HDPE thickness is obtained, one would not apply the values directly in the detector body fabrication due to engineering constraints that may arise during the installation of detector electronics and wiring, fill-gas valves, and exterior casing. It is decided to reduce the HDPE thickness marginally without reducing the efficiency greatly. The final dimensions of the HDPE matrix thickness are 2 cm front, 8 cm back, 4 cm interlayer, 2 cm of intercell, and 4 cm

of edge HDPE thickness. Overall, the efficiency of the matrix detector in this configuration of HDPE thicknesses is obtained at 12.5%. This efficiency is comparable to the efficiency of 4-atm ^{3}He proportional counters with a similar cross-sectional area of HDPE.

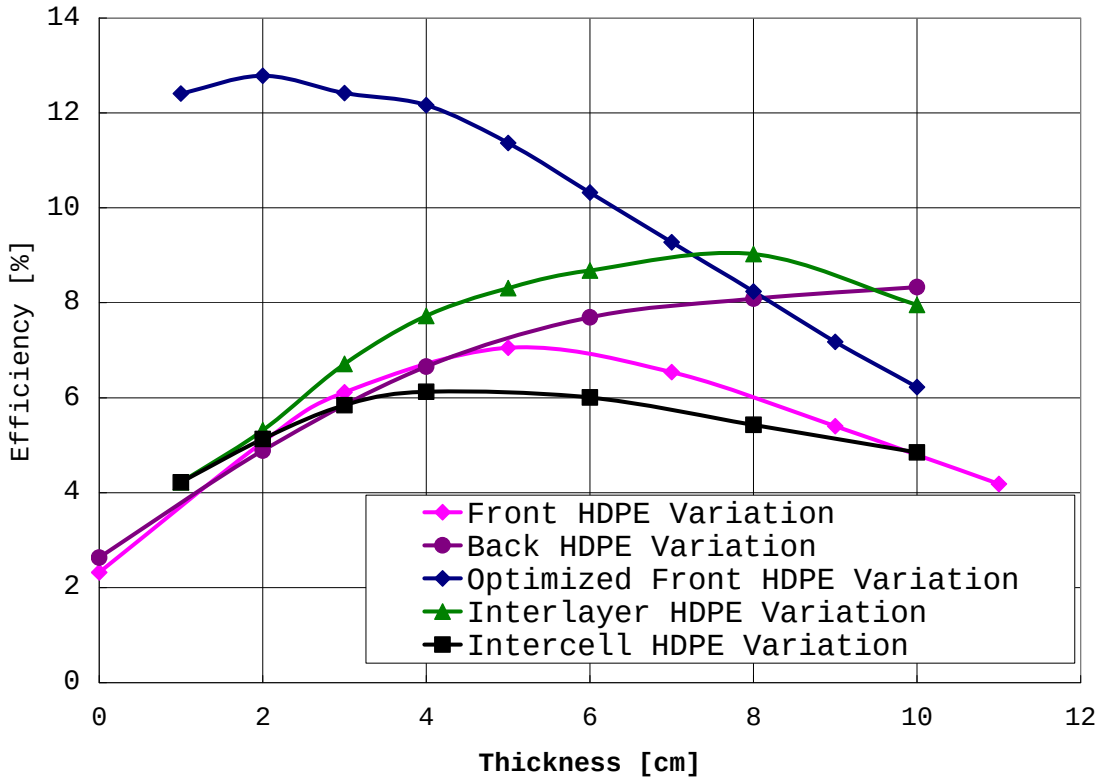

Fig. 10. HDPE thickness optimization. The optimized thicknesses are front: 2cm; back: 8cm; interlayer: 4cm; intercell: 2cm, and edge: 4cm.

After having established the thickness of HDPE and ^{6}Li layers are optimized for the production of primary charged particles, a series of simulation, shown in Fig. 11, is performed to observe how efficiency would change with moderated neutron sources. The optimized dimensions of the matrix detector, including the optimal thickness of ^{6}Li,

are used with moderated neutron sources of 1 keV, 10 keV, 100 keV, and unshielded ^{252}Cf. Having 2 cm front HDPE thickness resulted in efficiency values of 16%, 15%, and 14.5% for the 1 keV, 10 keV, and 100 keV monoenergetic neutron sources, respectively. This is indicative of the optimal front HDPE thickness that allows enough low energy neutrons to survive, but also allows fission neutrons to be sufficiently thermalized for interactions. The energy range between 1 keV and ^{252}Cf neutrons span 4 orders of magnitude; however, the efficiency does not differ by more than 4%. This is due to the large bulk of HDPE built as the body of the detector matrix serves as sufficient moderator for a wide range of neutron energy.

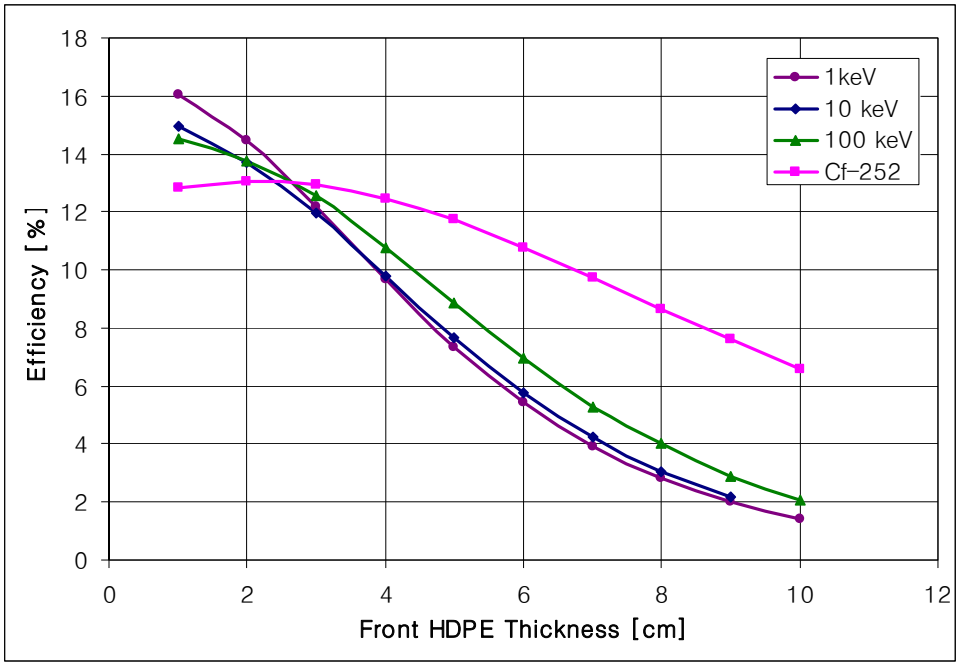

Fig. 11. Performance of matrix detector with neutron sources of varying energy levels.

4.3 Analytical calculation

Before GARFIELD could be employed, certain assumptions are made to bridge the gap between MCNPX and GARFIELD. MCNPX does not recognize the creation of tritons and alpha particles; MCNPX stops after calculating the interaction between thermal neutrons and ^{6}Li atoms and has no idea what particles are produced in the interactions. On the other hand, GARFIELD only creates electrons and does not have primary charged particles creating electrons in a gas medium. This gap can be bridged by using 2 assumptions; First, tritons are born with full 2.7 MeV and second, they expend all of their energy in the gas. Based upon the two assumptions, GARFIELD can now be programmed to produce approximately, on the average, 100000 ion pairs per triton track.

4.4 Triton track, time arrival distribution of electrons, and induced charge

After ^{6}Li(n,α)^{3}H interactions occur in the ^{6}Li metallization layer and primary charged particles are ejected in the fill-gas mixture, the interactions between either triton or alpha particle and fill gas atoms are simulated with GARFIELD (Veenhof, 2005). GARFIELD is used to simulate the transport properties of electrons such as mobility, diffusion coefficient, Townsend number, etc. The accuracy of GARFIELD was verified with the data accumulated at CERN (Peisert and Sauli, 1984). Magboltz in GARFIELD is the specific module used for this calculation, and it solves the Boltzmann transport equation by backward prolongation and Gauss-Seidel iteration (Biagi, 1995). GARFIELD has the capability to solve simple electric field configurations by analytical methods, and it is

used initially with a parallel plate geometry, which GARFIELD can simulate in its entirety. In this manner, GARFIELD can produce a set of data that can be verified with experimental results.

Fig. 12 depicts drifting of electrons randomly selected from one triton moving at 5° inclination with respect to the electrodes. The triton is emanating from the cathode plane positioned at (x=-3, y=0) and makes a track at 5° inclination. Because triton's speed is approximately 300 times faster than the electron drift velocity, it can be assumed that the electrons are created almost instantaneously along the tracks. This occurs regardless of the orientation of the triton tracks. For electrons that are born from a triton track parallel to the electrodes, they drift similar distances to reach the anode, and this tight arrival distribution is shown in Fig. 13. Fig. 13 shows less than a 2 micro-second width of time arrival distribution of electrons as they drift similar distances. Figs. 14 shows the simulated induced charge from the triton track simulated in Figs. 12. As expected, the induced charge in Fig. 14 has a steep rise time where almost all electrons drift in a tighter time period.

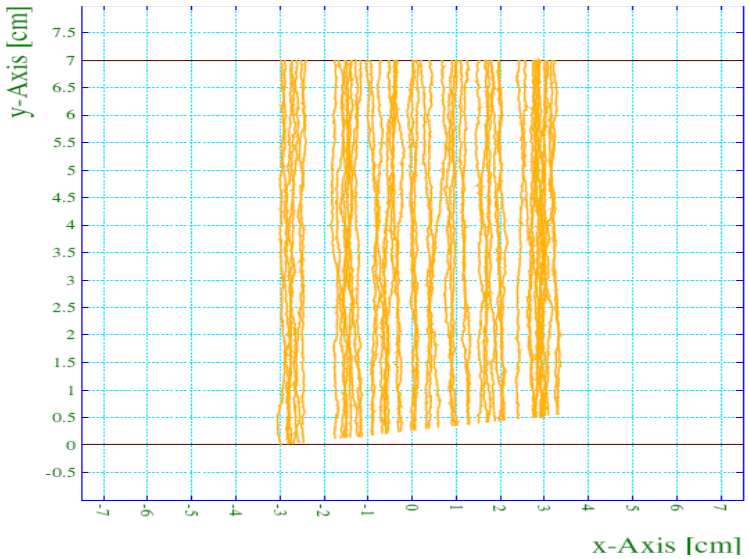

Fig. 12. An arbitrary triton track set at 5° inclination from the plane of cathode and the drift of free electrons created from interactions with the triton. The cathode is the lower horizontal line and the anode is the upper horizontal line.

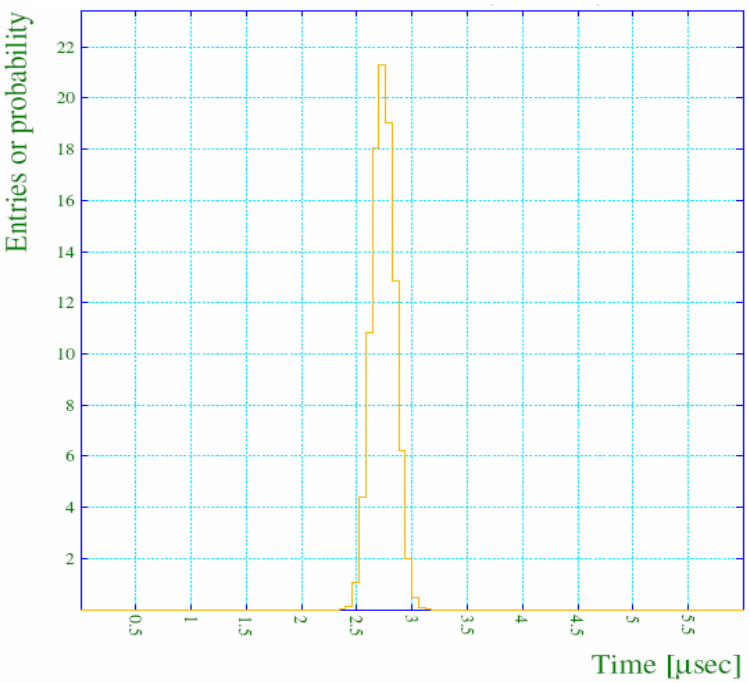

Fig. 13. Time arrival distribution of electrons for a triton track at 5° inclination. Electrons arrive from approximately 2.5 µsec to 3.2 µsec in a rather tight distribution.

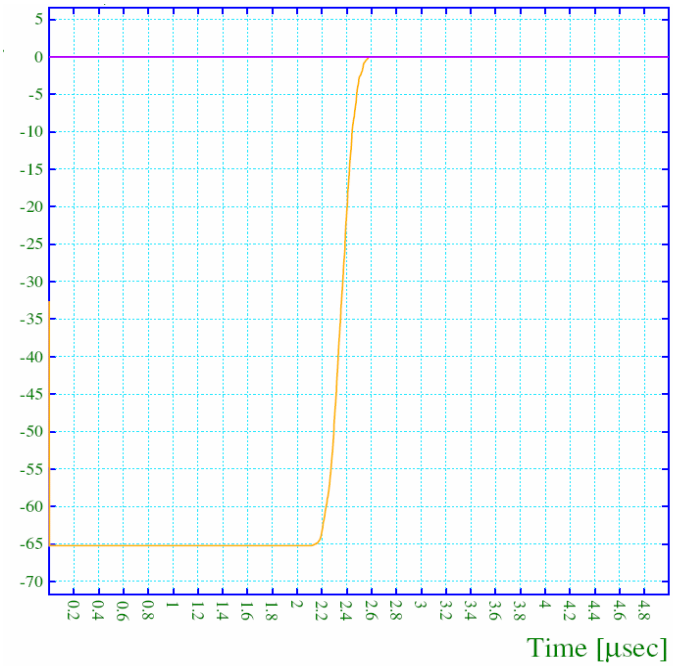

Fig. 14. Induced charges from a triton track at 5° inclination. The induced charges start to accumulate from 2.2 μsec and reach the full pulse plateau at 2.6 μsec.

Contrary to a triton track that is almost parallel to an electrode, Fig. 15 depicts a triton moving orthogonal to the electrode planes. A triton track is starting from the cathode (x=-3, y=0) and makes a rather straight path toward the anode serendipitously. During the process, there are electrons created near the track and because of the triton's speed, the electrons are seemingly created all at the same time. However, due to their location of creation, Fig. 16 shows electrons have much varied distances to drift and consequently have a wider distribution of the arrival. The plot in Fig. 17 shows a wider distribution of electrons, signal carriers, and hence, has a slower rise time.

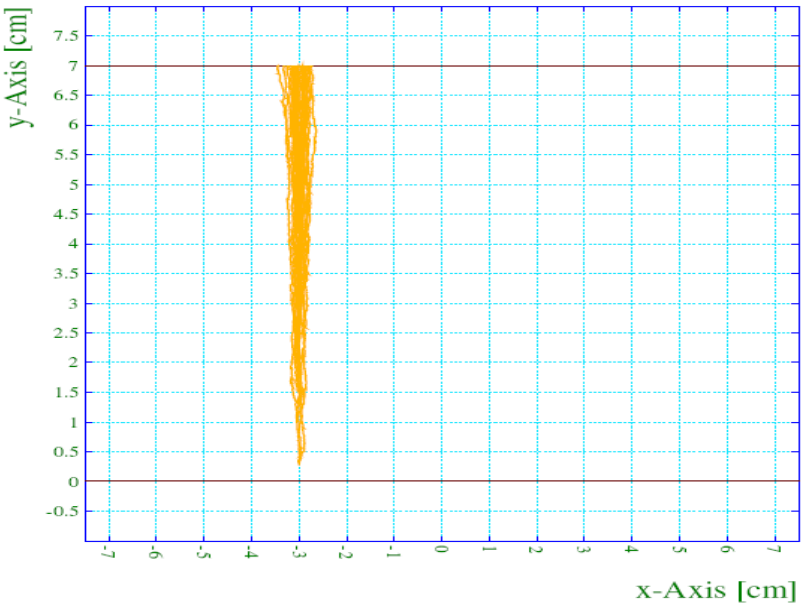

Fig. 15. An arbitrary triton track set normal from the plane of cathode and drift of free electrons created from interactions with the triton. The cathode is the lower horizontal line and the anode is the upper horizontal line.

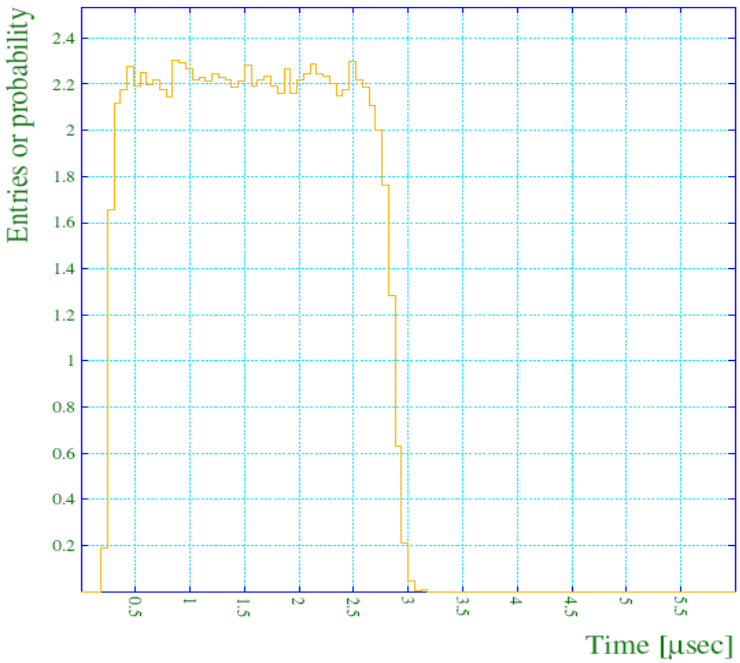

Fig. 16. Time arrival distribution of electrons for a triton track at 90° inclination. Electrons arrive from 0.2 µsec to 3.2 µsec in a much broader distribution than Fig. 14.

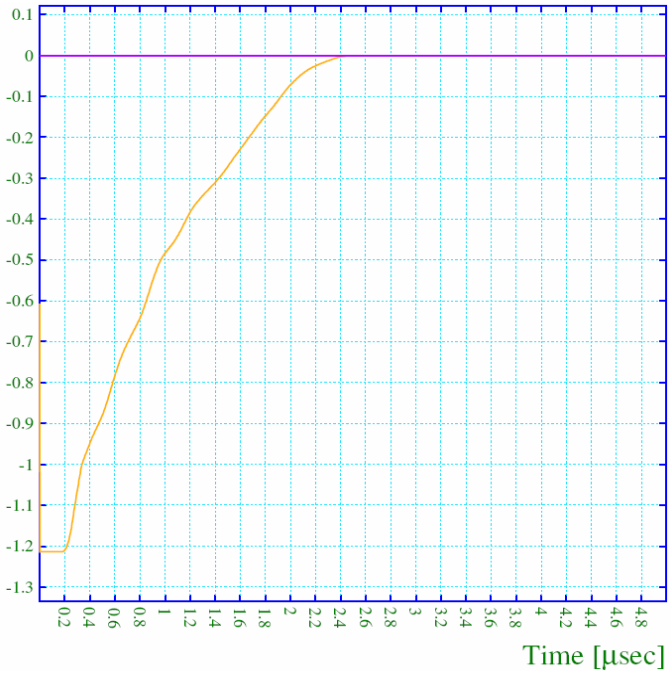

Fig. 17. Induced charges from a triton track at 90° inclination. The induced charges start to accumulate from 0.2 µsec and reach the full pulse plateau at 2.4 µsec.

Overall, one can assume that the electrons will drift in approximately 3 µsec, regardless of the orientation of the primary charged particle track, and that the induced charge will be collected fully in 2.8 µsec. These finding can benefit the designing of detector electronics to suit the need for charge collection efficiency.

Fig. 18 is a summary of electron drift velocity calculated with GARFIELD in argon-methane gas mixtures. The interesting feature in this plot is the convergence of electron drift velocity for different concentrations of methane between 0.06 and 0.09 V/cm/Torr. The information in Fig. 18 can be rearranged to show the direct correlation between the electron drift velocity and methane concentration in Fig. 19. The electron drift velocity

remains relatively constant for the field strength range between 4% and 15% of methane concentration. This indicates that electron drift velocity is affected minimally by the accumulation of methane in fill-gas. The electronics can maintain the same shaping time when the drift velocity is stable. The significance of this finding is that an ion chamber, when properly designed, can operate with accumulation of additional contamination in the fillgas. By obtaining the outgassing composition and rate, the ion chamber can be designed so that the appropriate drift velocity is maintained for the maximum detector lifetime.

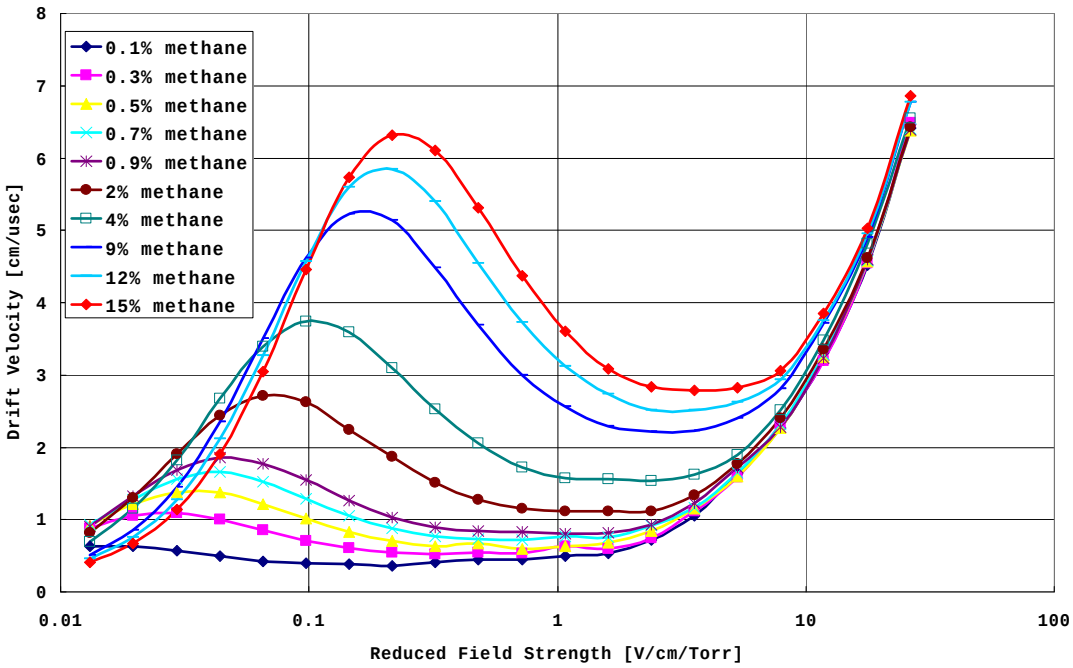

Fig. 18. Stability of electron drift velocity through a range of field strengths and methane concentrations. Copyright [2004] by IEEE.

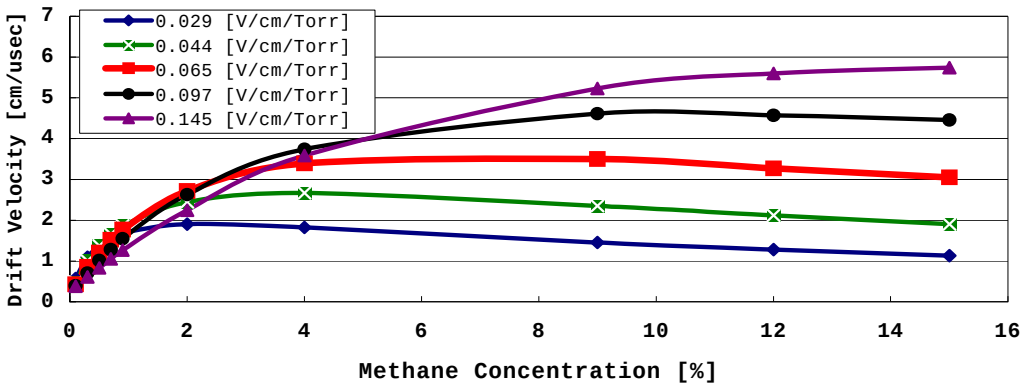

Fig. 19. A better plot of electron drift velocity as a function of methane concentration. Copyright [2004] by IEEE.

While Ar-CH_4 mixtures exhibit the convergence of electron drift velocity rather nicely, the outgas phenomenon of HDPE is complex, and the outgas can consist of multiple species of hydrocarbon fragments. Fig. 20 is a contour plot of electron drift velocity as a function of ethane and methane concentration at 0.09 V/cm/Torr. In this plot, if the fill-gas is preloaded with 1% methane, then the addition of ethane in the fill-gas greatly changes the electron drift velocity from 1.5 to 3.5 cm/μsec. The detector electronics would not be able to adjust to this much change in the velocity, and the detector would be operating at less than optimal condition. However, if the fill-gas is preloaded with 3% of methane, then the addition of ethane does not affect the electron drift velocity and the detector electronics can accommodate the change of velocity. This methodology of preloading the fill-gas with hydrocarbon species may be able to mitigate the deleterious effect of other species.

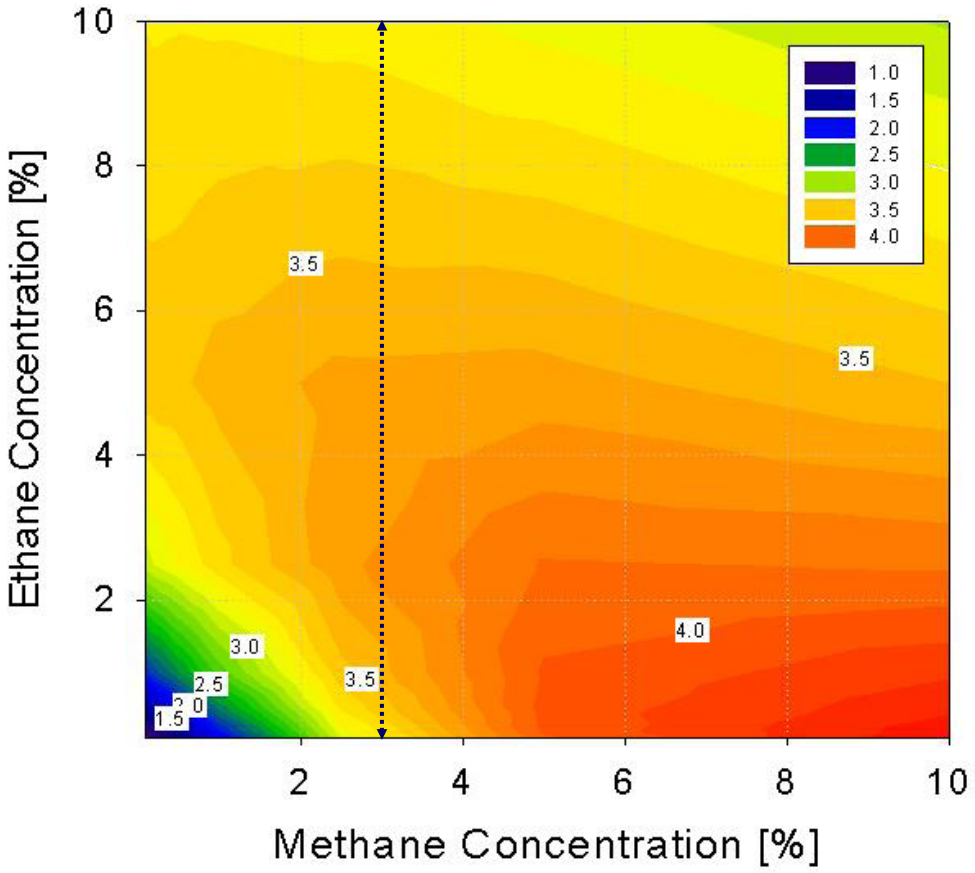

Fig. 20. Electron drift velocity in the presence of methane and ethane. Copyright [2005] by IEEE.

4.5 Finding a suitable combination of electric field strength and fill-gas mixtures

GARFIELD has limited ability to obtain the ion transport properties in the fill-gas due to its inability to calculate complex electric field configurations. The electric field mapping of the active volume of the LiPMIC, which GARFIELD can not handle due to the lack of conversion code to 3-dimensional field map values, is tasked to an electrostatic simulation package called OPERA. Fig. 21 is the 3-dimensional inside view of a single-cell showing the rounded corners and edges of both cathode and anode surfaces and

ceramic stand-offs supporting the anode. Fig. 22 shows the voltage applied in the plane of z=0. The optimal voltage to maintain the stability of drift velocity for electrons is calculated to be 160V. In comparison with proportional counters, which routinely use 2000-3000V for their operation, 160V allows much smaller energy foot-print and extends the possibility of deploying LiPMICs in remote monitoring.

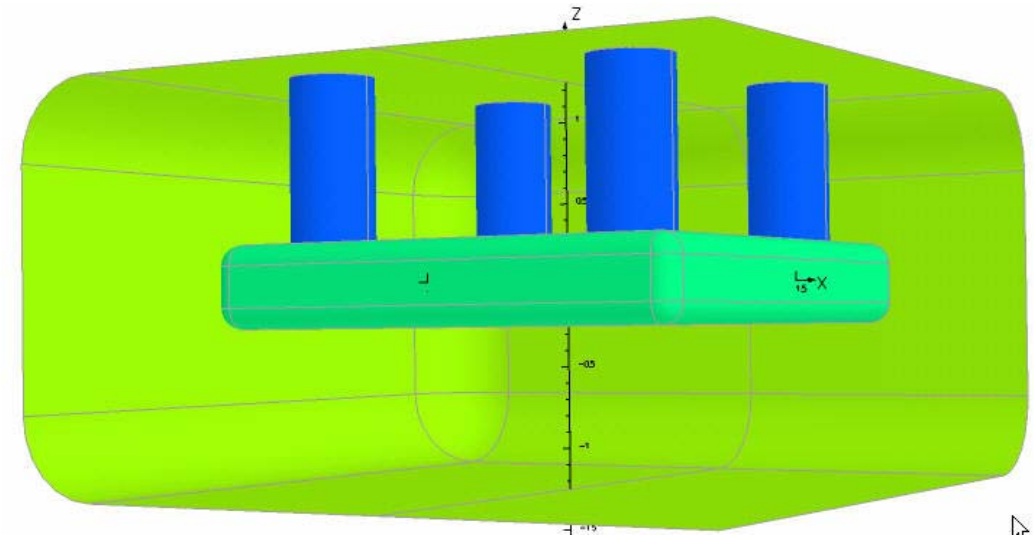

Fig. 21. Three-dimension cutaway view of detector volume.

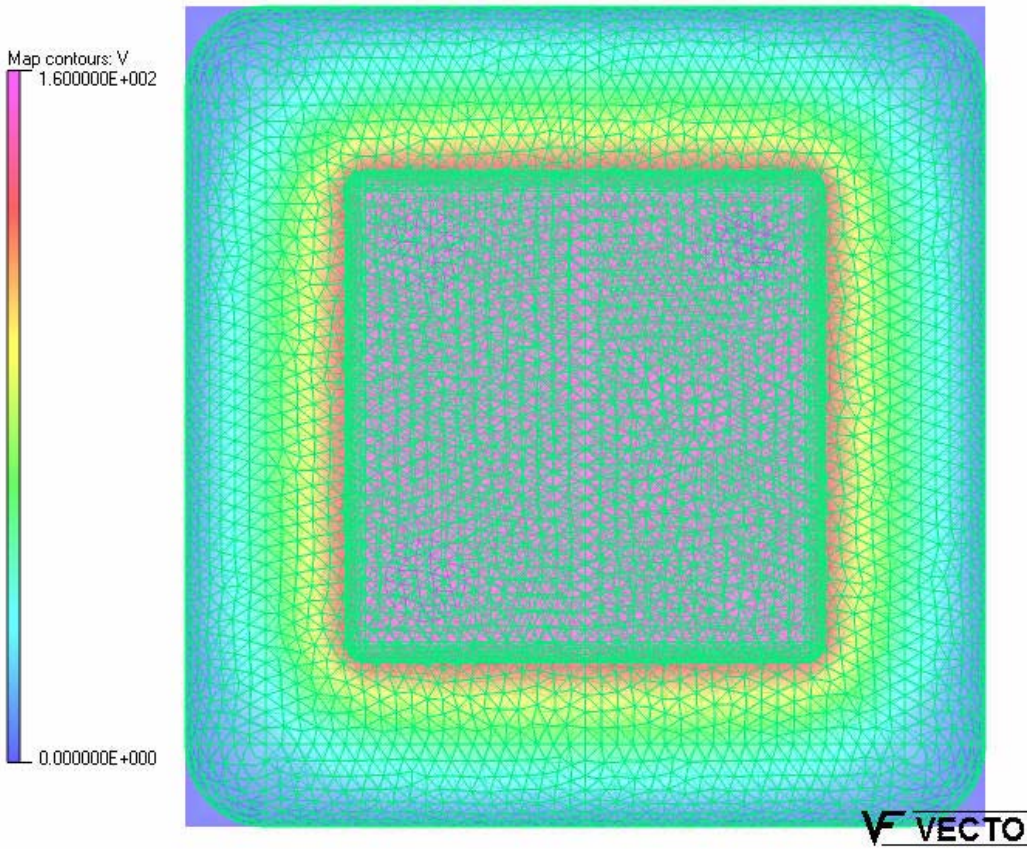

Fig. 22. Contour map of applied voltage at Z=0 plane.

It is fundamental for the detector operation to ensure that the majority of the active volume of the detector cells has the minimal electric field strength to maintain the desired electron drift velocity. Unfortunately, it is not possible to have completely uniform electric field strength as corners of anodes show intense concentration of electric field lines. Figs. 23 and 24 show the electric field strength calculated using finite-element mapping. Both figures show that the majority of the plane is at uniform electric field strength, indicating that there exists an electric field conducive to ion

chamber mode of operation. Table 3 shows the field strength at majority of the detector volume surpasses the minimal field strength required for stable electron drift velocity.

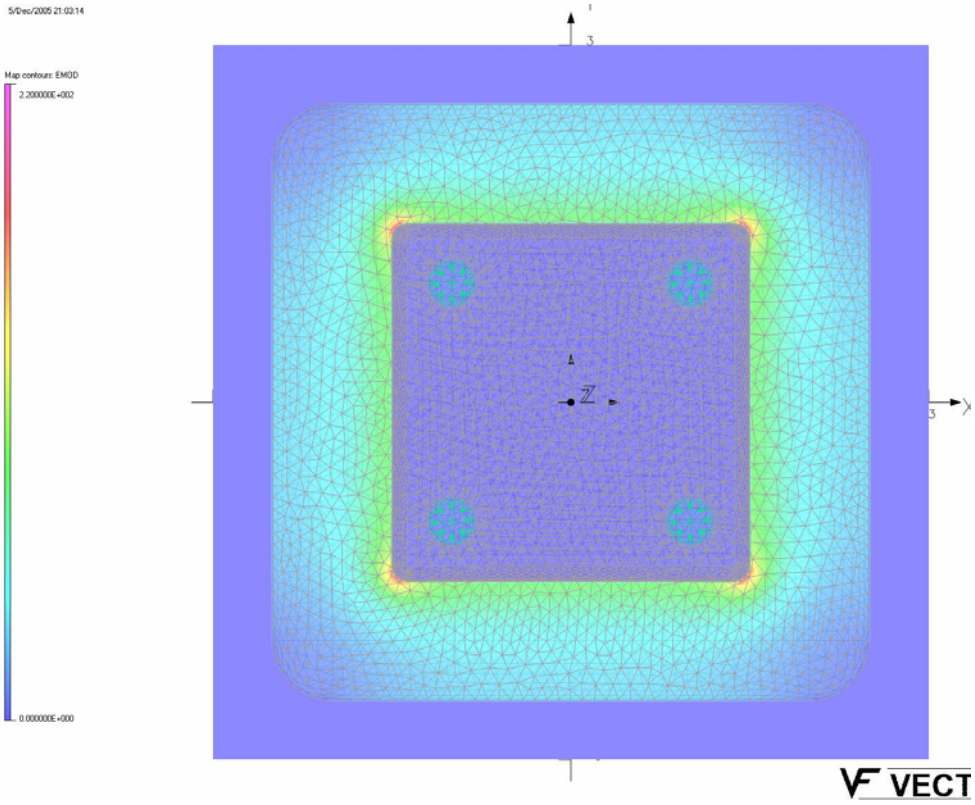

Fig. 23. Normalized contour map of electric field strength at Z=0 plane.

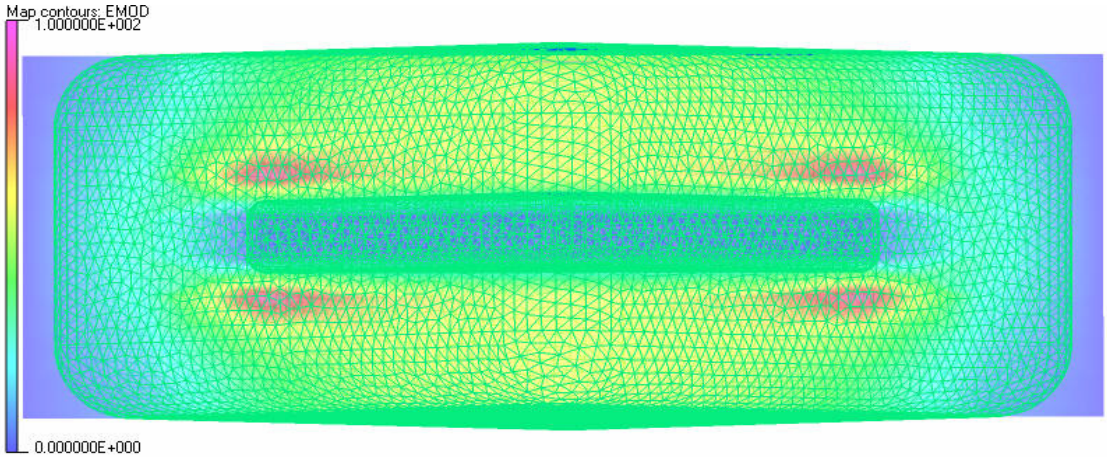

Fig. 24. Normalized contour map of a diagonal plane. The closest corner is shown in the middle of the figure.

Table 3
Reduced electric field strength with bias voltage of -130V at various points in the detector volume

x,y=(0,0)											
z	-1.25	-1.00	-0.75	-0.50	-0.25	0	0.25	0.50	0.75	1.00	1.25
V/cm/Torr	0.0662	0.0666	0.0673	0.0682	0.0001	0.0000	0.0001	0.0714	0.0671	0.0633	0.0616
x,y=(0.65, 0.65)											
z	-1.25	-1.00	-0.75	-0.50	-0.25	0	0.25	0.50	0.75	1.00	1.25
V/cm/Torr	0.0629	0.0643	0.0671	0.0706	0.0722	0.0075	0.0086	0.1029	0.0693	0.0466	0.0371
x,y=(0,1.0)											
z	-1.25	-1.00	-0.75	-0.50	-0.25	0	0.25	0.50	0.75	1.00	1.25
V/cm/Torr	0.0608	0.0626	0.0667	0.0726	0.0761	0.0000	0.0004	0.0797	0.0656	0.0554	0.0514
x,y=(1.4, 1.4)											
z	-1.25	-1.00	-0.75	-0.50	-0.25	0	0.25	0.50	0.75	1.00	1.25
V/cm/Torr	0.0378	0.0415	0.0531	0.0826	0.2774	0.0045	0.3346	0.0849	0.0404	0.0248	0.0196
x,y=(2.2, 2.2)											
z	-1.25	-1.00	-0.75	-0.50	-0.25	0	0.25	0.50	0.75	1.00	1.25
V/cm/Torr	0.0036	0.0047	0.0080	0.0108	0.0129	0.0138	0.0126	0.0102	0.0072	0.0042	0.0023
x,y=(2.0, 2.5)											
z	-1.25	-1.00	-0.75	-0.50	-0.25	0	0.25	0.50	0.75	1.00	1.25
V/cm/Torr	NA	NA	0.0063	0.0102	0.0124	0.0130	0.0119	0.0096	0.0065	0.0031	0.0000
x,y=(2.5, 0)											
z	-1.25	-1.00	-0.75	-0.50	-0.25	0	0.25	0.50	0.75	1.00	1.25
V/cm/Torr	NA	NA	0.0217	0.0336	0.0413	0.0441	0.0407	0.0327	0.0222	0.0109	0.0001

The different simulation tools assembled for this portion of the research should provide an independent set of estimates for the performance of the ion chamber. Starting from the source neutrons, the HDPE thickness is optimized for efficient moderation of source neutrons to thermal energy range at the position of ^{6}Li. The thickness of the ^{6}Li metallization layer is tested to balance the primary charged particle production rate and escape probability of the particles from ^{6}Li metallization layer. To simulate the interactions among charged particles and fill-gas atoms, GARFIELD is used. GARFIELD is also used to find a range of fill-gas concentration and electric field strength that provide a stable electron drift velocity. Then, having found the range, electric field strength was mapped and tested using OPERA.

5. EXPERIMENTS*

The experiments conducted in this research are largely divided into three categories: characterization of outgas, fabrication and testing of detector body, and nuclear measurements. Characterization of outgas involves composition analyses and quantification of outgas rate. The characterization took 8 months of data collection and an analysis performed by Evans Laboratory in Sunnyvale, CA. During this time, HDPE shell for a detector matrix was machined and tested for vacuum integrity. This required maintaining a high vacuum state, and testing with ^{4}He leak detectors. The shell was fitted with custom-made gaskets and other components to ensure the structural and vacuum integrity were maintained during nuclear experiments. Having obtained the outgas rate and composition, and a detector matrix capable of holding vacuum for an extended period, ^{6}Li metallization was applied at Sion Power, Inc., in Tucson, AZ. The detector matrix was then ready for nuclear measurements. The detector matrix was tested for gamma sensitivity, for vulnerability against microphonic noise, for the effect of shaping time on count rate and pulse height spectrum, baseline measurement, and comparison with MCNPX calculations.

* Part of this section is reprinted with permission from "Mitigation of outgas effects in the neutron-capture ^{6}Li pulse-mode ionization chamber operation." by Kiwhan Chung, Kiril Inakiev, Martyn Swinhoe, Mark Makela, 2005. IEEE Nuclear Science Symposium Conference Record. 3, 1255-1257, Copyright [2005] by IEEE.

5.1 Outgas rate and composition analyses

One of the novel design aspects of the detector array is the use of HDPE bodies as an integral part of the detector. Conventional gaseous thermal neutron detector designs would have a clear separation of the moderating part and the wall of the gas volume of the detector where thermalized neutrons interact with fill-gas atoms. However, in this detector design, the separation of energy-moderating volume and the active volume of the detector where charge collection occurs is established by 8-μm thick metallization layer. The advantage of this design is that the use of an integral polyethylene body allows employing widely available manufacturing methods to mass-produce inexpensive polymer bodies. Unfortunately, it also brings on contamination of fill-gas by outgas from the body. The outgas can cripple the detector operation, even with detector being air-tight, by altering the fill-gas composition from within and by forming negative ions and disrupting the processes in creating secondary electrons, which are the main signal carriers. Therefore, ascertaining the outgas composition and rate to establish a window of tolerance are fundamental in designing operational specification.

First, outgas rate measurements were performed under vacuum, using the pressure gradient to accelerate the process; without the use of vacuum, it would have required prohibitively long experiments to collect measurable amount of outgas. The inside dimensions of the outgas chamber (Fig. 25), which was a section of a cylindrical pipe capped with two metallized polyethylene pieces, were 9.73 cm and 10.16 cm in length. The total surface area subject to outgas, which is the interior surface area of the chamber,

was calculated as 270.91 cm^2 and the volume of the chamber was calculated as 755.18 cm^3. This chamber was evacuated by a turbo vacuum pump attached to a residual gas analyzer (Stanford Research Systems, RGA-100).

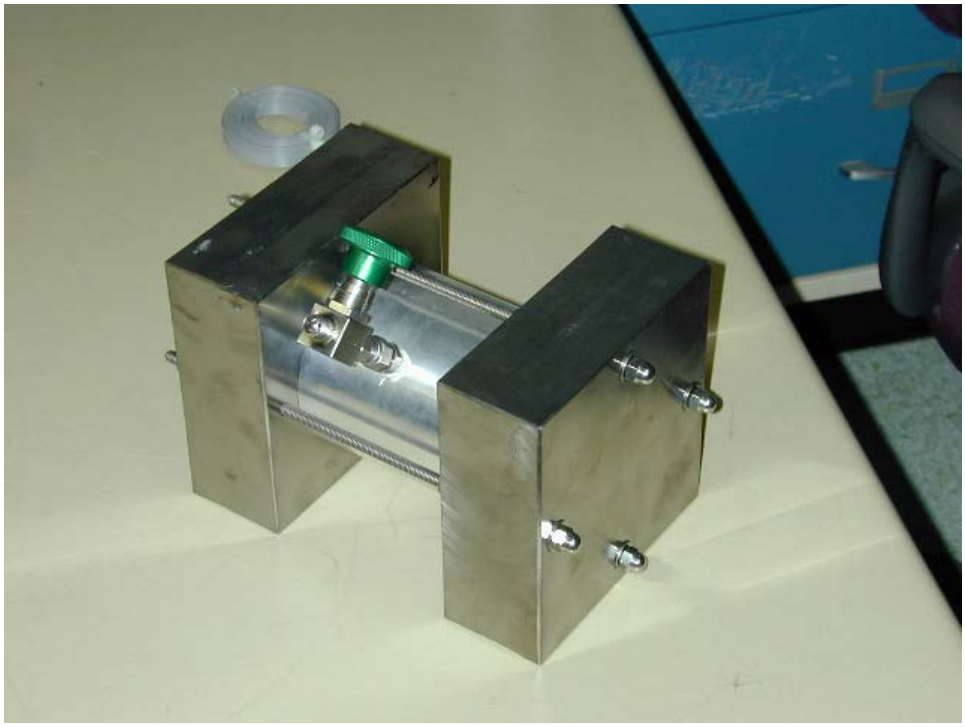

Fig. 25. A cylindrical chamber with HDPE ends used to obtain outgas data.

The chamber was pumped out to 10^{-8} torr of vacuum over 24 hours and the inside pressure was recorded with a Mensor Digital Pressure Gauge Series 2101 to obtain the outgas accumulation. The outgas would come mainly from the two walls of metallized polyethylene end pieces and the stainless steel wall. During 238 days of monitoring, there was 3.9 torr of pressure accumulation inside (Ianakiev et al., 2004). Fig. 26 shows that there are two outgas rates for this configuration. Most published results of outgas of

HDPE indicate one outgas rate, while many polymers exhibit two outgas rates, the initial rate being much larger of the two. For this sample, the first outgas rate was 0.052 torr per day during the first 34 days. Then the outgas rate was reduced to 0.011 torr per day for the next 204 days, the remainder of the measurement period. The combined outgas rate for the entire observation period was calculated as 0.016 torr per day. This total accumulated outgas rate can be converted into a standard outgas rate by considering the surface area of outgas and the volume of the outgas chamber. Then, the overall outgas rate of 9.6×10^{-10} torr-liter/(cm^2-sec) was obtained. It is approximately 2 orders of magnitude lower than a published outgas rate data, 2.6×10^{-7} torr-liter/(cm^2-sec), of bare polyethylene. When the overall outgas rate takes outgas contribution from the cylinder wall into consideration, which is made out of stainless steel, then the outgas rate drops further to 5.3×10^{-10} torr-liter/(cm^2-sec). This reduced rate clearly shows outgas of the polyethylene is reduced in this configuration.

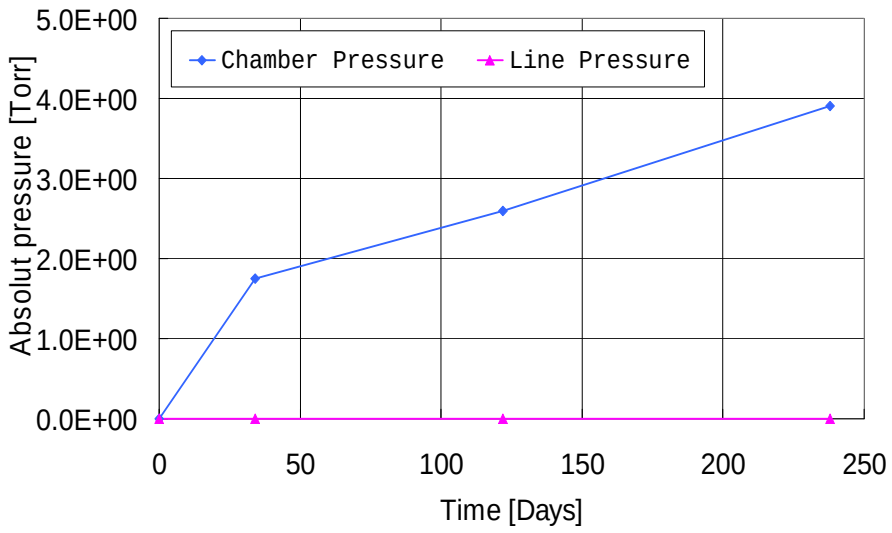

Fig. 26. Pressure accumulation inside the outgas chamber. Copyright [2005] by IEEE.

A partial explanation of the reduced outgas rate can be attributed to the metallization layer, whose scanning electron microscope image is depicted in Fig. 27. Fig. 27 shows complete coverage of metallization layer on the surface of polymer, however, one can see dark lines that indicate cracking of the metallization surface. The 8-micron thick metal film may act as an atomic barrier and hinder the migration of outgas from the polymer lattice to the vapor phase, thereby reducing the outgas.

Unfortunately, this explanation cannot fully explain the 2 orders of magnitude reduction in the outgas rate. It is conceivable that the metallization aided in reducing the flow of outgas, but a bulk of credit can be given to the partial pressure of outgas molecules inside the polymer matching the low partial vapor pressure in the vacuum to slow down the diffusion of the outgas components (de Segovia, 1999). The long-term outgas rate, which reflects the second, stable outgas rate of approximately 0.3 torr/month would allow approximately 10 years of continuous operation when electron dynamics were simulated using GARFIELD (Chung et al., 2005). However, this outgas estimate is considered to be a grossly conservative estimate due to the condition in which the long-term outgas rate is derived. As stated previously, this outgas measurement had to be performed under vacuum. Having such a drastic pressure gradient across a piece of 4.5 cm thick piece of polyethylene for over 200 days became a great driving condition for the penetrants. The magnitude of this factor would be unlikely to be encountered in real detector operation, and the ensuing outgas rate should be considered as the upper limit of outgas rate for the polymer.

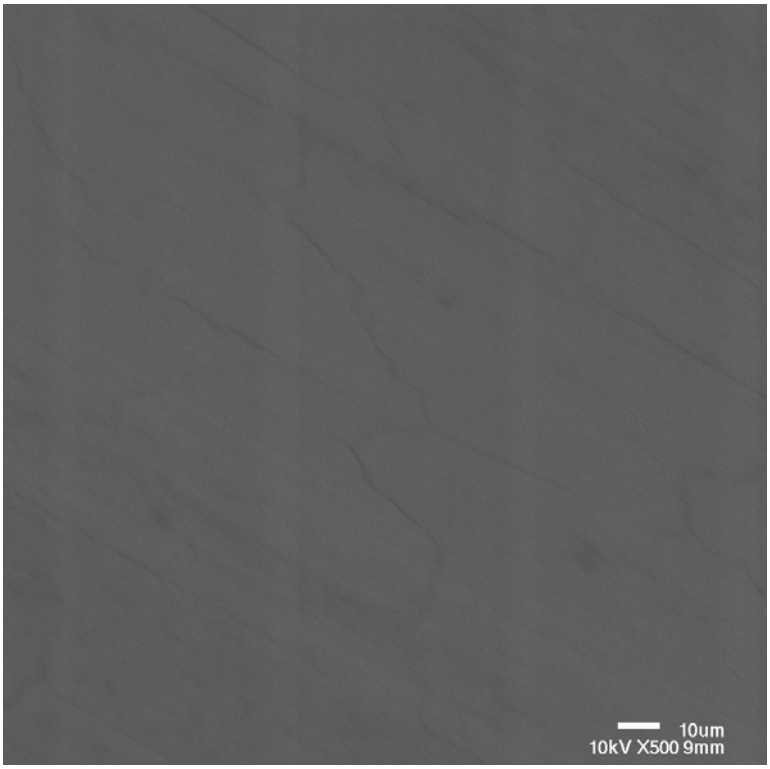

Fig. 27. A scanning electron microscope image of improved nickel-stainless steel metallization on polymer surface.

With the upper limit of outgas rate quantified, the components of the outgas were identified using two different methods. The first method was performed using a residual gas analyzer (RGA). The advantage of this method is that the setup of the system is rather compact and simple so that analyses can be performed on site, attached to the outgas chamber, with minimal calibration as shown in Fig. 28. There is no need to take a sample and send it to an off-site laboratory for results. The analyses using a Stanford Research Systems RGA-100 indicated the outgas was mostly made up of environmental components (Fig. 29) such as water (43.92%), carbon dioxide (6.239%), nitrogen (39.37%), argon (1.081%), and oxygen (9.389%). Fig. 26 may seem a classical plot of a

leaky chamber, but the chamber was tested for leaks with a helium leak detector extensively.

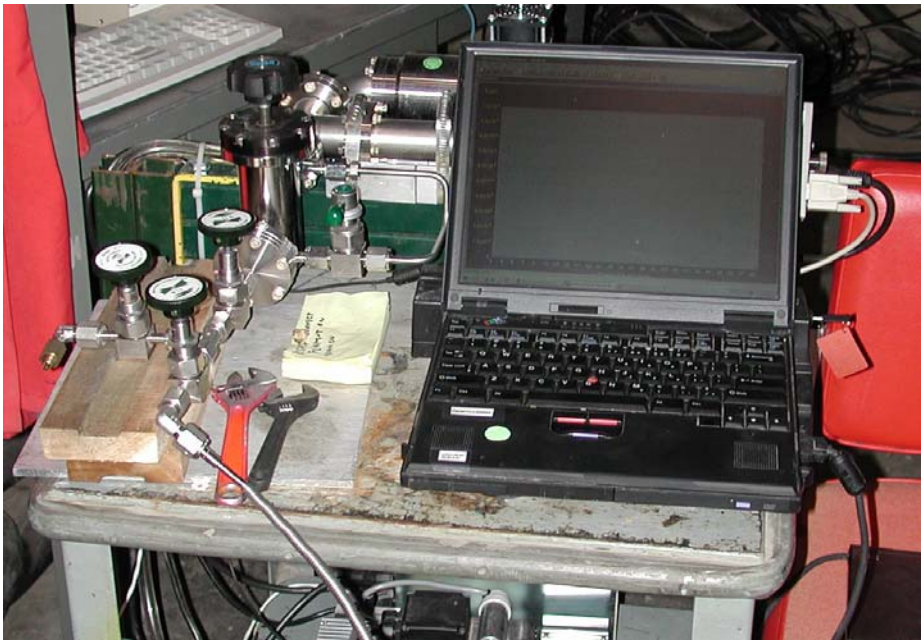

Fig. 28. Residual gas analyzer setup with a laptop front end.

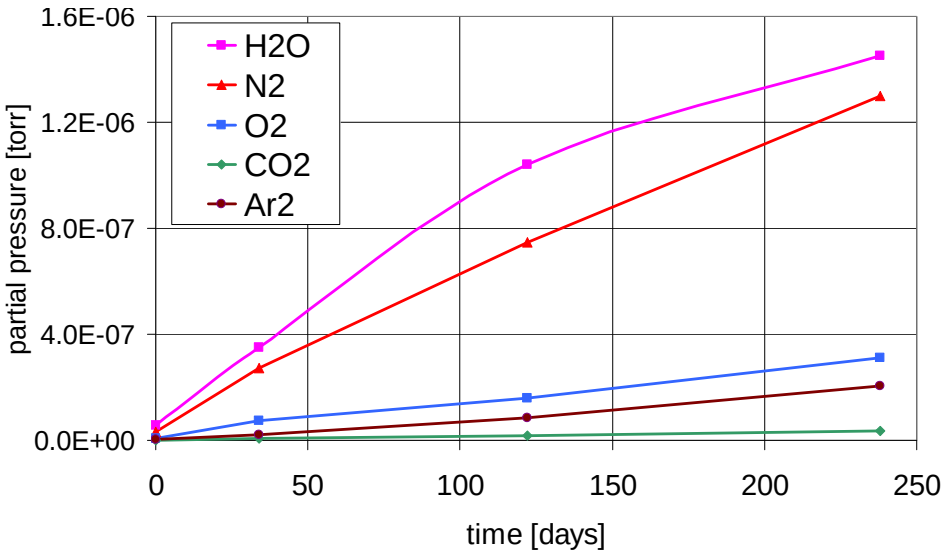

Fig. 29. Accumulation of mass fragments in the outgas chamber.

The other method of outgas identification employed was gas chromatography/mass spectrometry (GC/MS) using dynamic head space analysis (HSA). The dynamic head-space analysis combined with routine GC/MS analysis allows analyses of volatile compounds that could not be directly injected into a gas chromatograph. In HSA, a sample is heated in inert gas as in regular GC/MS analyses. The difference is the method in which outgas is handled. In HSA, outgas is trapped to a filter and then the components trapped in the filter are released by heating the filter material and by using reverse flow to flush the outgas to GC. Then, a routine GC/MS analysis is performed. GC/MS is one of the most widely used measurement techniques to identify the volatile organics, but the accuracy requires stable measurement environment where routine calibration and cross contamination between different sample runs is eliminated. Hence, GC/MS equipment is located in an analytical chemistry lab where the system can be maintained by qualified support staff. For the particular analyses, a Hewlett-Packard 6890 Gas Chromatograph and Hewlett-Packard 5973 Mass Spectrometer were used.

For obtaining the outgas components released at near room temperature, the GC/MS may not be suitable because the sample is heated to high temperature to increase the rate of outgas. If the sample is heated to temperatures above those where real application may not occur, the analysis results may not be relevant to the use of the polymer in the detector. At the same time, there are no readily available, accurate chemical analysis that can be done with samples at room temperature because the samples do not readily give off detectable quantities of outgas products at room temperature. However, for this

research, outgas composition obtained at high temperatures, at which detectors would not likely operate due to polyethylene failure, can serve as the boundary condition. Table 4 shows the components of outgas that are very different from the components identified with an RGA. This is partially due to the nature of GC/MS emphasizing the outgas occurring at high temperature and due to the analysis using an external standard to calibrate the analysis. The GC/MS HSA report indicated that the chamber that contained the sample was heated from 35 to 150 Celcius at a rate of 10 Celcius per minute and from 150 to 300 Celcius at 15 Celcius per minute. Methylene chloride was used as an external standard, and unfortunately, its signature peaks masked those of water. Consequently, water is not accounted for in this result as it tends to be given off in the early period of sample heating. The majority of the outgas components from the sample is in a class of hydrocarbons called alkane and are listed in Table 4. Alkane includes methane, ethane, and many others, including the ones identified by GC/MS HSA. Microscopic concentrations of heavy alkanes such decane and octadecane indicate that the breakdown of polymer structure that can release additives or polymer chains as fragments of heavy alkane hydrocarbon at high temperatures.

Table 4
Outgas composition from GC/MS dynamic head-space analysis

	Decane	Dodecane	Dimethyl-cyclohexane	Tetradecane	1,4-bezenedi-carboxylic acid	Hexadecane	Octadecane
Metalized HDPE sample	4.34 μg 30.46 ppb	12.27 μg 72.03 ppb	2.11 μg 18.80 ppb	15.77 μg 79.49 ppb	8.73 μg 44.95 ppb	<7.91 μg < 34.93 ppb	2.10 μg 8.25 ppb
Bare HDPE sample	19.34 μg 135.9 ppb	18.66 μg 109.6 ppb	NONE	10.18 μg 51.31 ppb	NONE	2.72 μg 12.01 ppb	0.36 μg 1.41 ppb

Fig. 30 is a chromatograph of volatile organics outgassed from a metallized polyethylene sample. This plot is the summary of all outgas peaks detected during the gas chromatography analysis. Using the mass spectrometry and comparing the peaks to the standard library such as one from National Institute of Standards and Technology, different compounds are identified. Fig. 31 is an example of such identification for decane, whose total mass per mole is 142.29 g. The small peak at 142 indicates that

decane, being a long chain of hydrocarbon molecules, seldom retains its complete molecular form. Instead, the molecule is either broken up in the polymer or during the MS analysis such that the compound's mass to charge ratio is distributed into different mass numbers in Fig. 31. The peaks are identified through comparison with standards and their concentration is derived.

In summary, the outgas rate of more than 2 orders of magnitude lower than the published outgas rate of HDPE is obtained, and the outgas composition made up of mostly either environmental components or heavy alkane series were found. The results from the GC/MS HSA are inconclusive about the presence of environmental outgases such as water vapor, nitrogen, etc., since the naturally occurring light elements and compounds were ignored in order to obtain more accurate analyses of heavy, volatile organic compounds. It is believed that the trace amount of volatile organic compounds in the range of 10 ppb does not effect the performance of the detectors.

File : E:\DEC05\K8100-2.D
Operator : XC
Acquired : 23 Dec 2005 7:47 using AcqMethod CDS_XC10
Instrument : GC/MS Ins
Sample Name: Metal covered sample with 600 ng C16
Misc Info : Ch9, 45C, 16 hours
Vial Number: 1

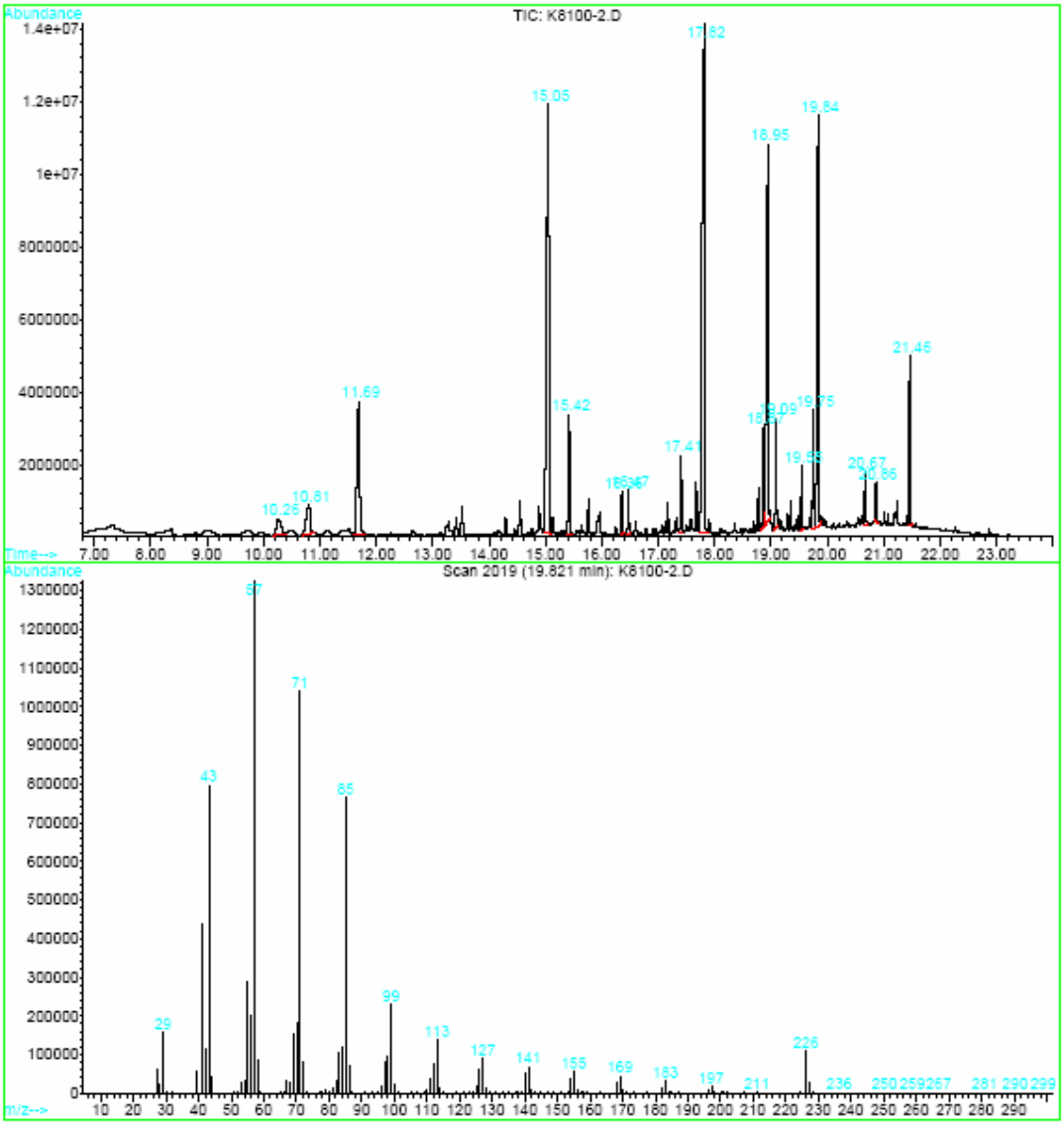

Fig. 30. A gas chromatograph of volatile organics from a metallized polyethylene sample. The bottom graph is the plot of n-hexadecane used as an external standard.

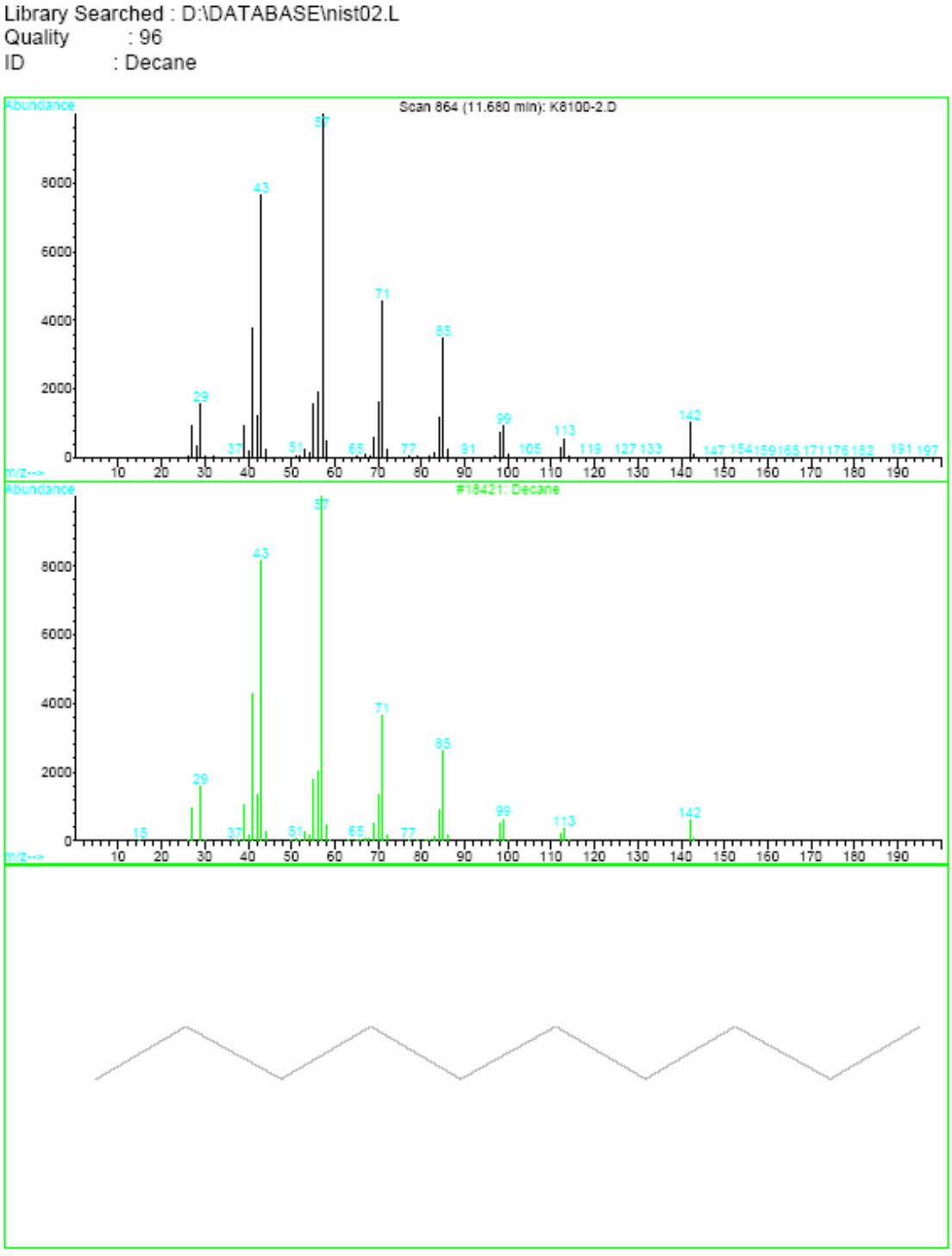

Fig. 31. A gas chromatograph of decane. A standard gas chromatograph of decane in NIST 2002 library is depicted in the middle plot. The bottom plot indicates the skeletal chemical diagram of decane.

The fabrication and testing of a prototype detector array shown in Fig. 32 posed significantly more issues than single-cell prototype detectors due to the size of polyethylene blocks and the complexity of the inner volume of the detector array. The 8-fold increase in the inner surface area and interface increases the overall outgas rate and possibility of microscopic leaks occurring at the interface, risking the long-term fill-gas integrity. While the increased outgas rate may be small, the accumulated and combined effect may shorten detector's continuous operation, requiring more frequent servicing and longer service time for the detectors.

Fig. 32. Machined, bare polyethylene body; 2 lids and 1 middle piece (center).

5.2 Testing of the seal integrity

After polyethylene pieces were machined, as shown in Fig. 32, and their surfaces were metallized (Fig. 33), different types of gaskets were used to test the seal integrity. The total length of seal interface for the polyethylene bodies is approximately 220 cm and the

use of commercial off the shelf (COTS) viton gasket or silicone sheet gaskets resulted in measurable leaks. In the end, custom-made viton o-rings of 55 durometer, 0.53 cm of cross section, and 109.47 cm of developed length prior to the forming of o-ring, were used. Durometer is a unit to measure hardness and follows ASTM D2240 testing method. 'Developed length' is a rubber manufacturing term used to define the length of a rubber cord before it is made into an o-ring. The dimensions of the perimeter groove are 6.1 mm wide and 3.8 mm deep. The o-ring would fill the groove approximately 90% at full compression and would allow small movement in the channel to minimize rubbing, which is necessary to ensure the longevity of the o-ring. The center o-ring was fabricated out of a silicone sheet of similar hardness of 60 durometer. The use of customized, stamped silicone o-rings in the center of the HDPE pieces was necessary because 1.3 cm outer radius for the center groove would not allow gluing of viton cord into an o-ring shape. The heavy use of glue to adhere the viton piece into an o-ring shape cracked under the compression of the HDPE bodies, or inadequate amount of glue left the o-ring in the groove deformed. When a custom seal manufacturing firm, ElastoSeal, Inc., was contacted to make the viton o-rings for the detector array, the company would not guarantee the performance of the o-ring made out of viton for the center groove; instead, the company suggested fabricating a silicone o-ring made out of a silicone sheet. The center o-ring made out of silicone was fabricated in-house using rubber stamping tools.

Fig. 33. Polyethylene body with 8-micro thick nickel and stainless steel metallization.

The o-rings were then lubricated with Dow-Corning High Vacuum Grease (Fig. 34), and the HDPE bodies were assembled together with bolts using a torque wrench set at 1.13 N-m. Seventeen bolts were tightened with a torque wrench in a diagonal order to ensure uniform distribution of pressure across the polyethylene bodies. Using a Pfeiffer Vacuums QualyTest Dry HLT 270 leak detector, the detector array was tested for vacuum integrity. The leak detector can detect trace amount of helium with a sensitivity of 10^{-10} mbar*liter/sec of flow rate, which is more than adequate for detecting leak rates of the detector array. Using a helium spray probe, seal integrity was checked and the entire interface was confirmed to be vacuum-tight. The background flow rate of helium

was recorded as $1.6x10^{-8}$ mBar*liter/sec, which became the practical limit of detection for the experiment conditions. The leak tests were performed on all sides, including valves and signal wire connections, and showed there is no detectable penetration of helium atoms.

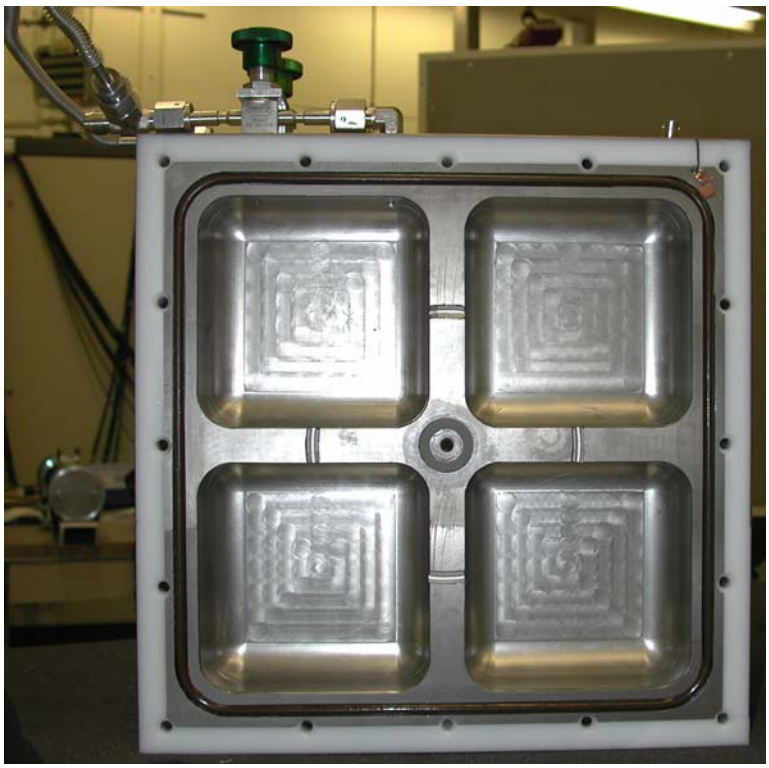

Fig. 34. Close-up of o-ring placement.

This is a significant step in detector development since maintaining gas purity within the design specification is a crucial factor in deciding the lifespan of the detector. Even though helium will not be used in fill-gas and the detector will not operate in vacuum, the leak tests were performed with helium in vacuum condition because of the helium

atoms' small size, low background concentration, ready availability and low reaction rate with surrounding atoms. For example, the atomic radius of a helium atom is 31 picometer, whereas an argon atom's is 71 picometer, effectively giving a helium atom less than a quarter cross section than that of an argon atom. The diffusion coefficients of helium, argon and methane in polyethylene are $57x10^{-7}$, $4.5x10^{-7}$, and $1.9x10^{-7}$ cm^2/sec, respectively (Flaconneche and Klopffer, 2001). The difference in diffusion coefficients shows that the helium atoms are more than 10 times more mobile than argon atoms in polyethylene. This conservative test emphasizes the robustness of the seal of the detector and thereby assures the longevity of the detector operation.

The long-term leak tests saturating the entire detector array in a helium medium were not performed because the mobility and size of the helium atoms would allow penetration eventually through the polyethylene body. The leakage through structural failures at the seal interface would readily show up with short-term helium leak tests. Permeability rate would be analogous to longer-term leak tests because permeation may be considered a long-term, three-stage process that includes absorption, diffusion and desorption. The helium permeability rates through polyethylene and viton are comparable at $2x10^{-7}$ and $1.2x10^{-7}$ $cc/sec/cm^2/cm$ at 1 atmospheric pressure at 25 Celsius (1cc of helium per second per cm^2 of surface area per cm of thickness at 1 atm), respectively. The permeability rate through silicone is $23.8x10^{-7}$ $cc/sec/cm^2/cm$ at 1 atmospheric pressure at 25 Celsius (Varian Associates, 1980). A comparison study of permeability rate showed argon atoms, the main constituent in the fill-gas, at $0.76x10^{-7}$ $cc/sec/cm^2/cm$ at 1

atmospheric pressure at 61 Celsius, while the same study showed 2.1×10^{-7} cc/sec/cm^2/cm at 1 atmospheric pressure at 59 Celsius (Flaconneche and Klopffer, 2001). The permeability rate of methane, which is the other constituent in the fill-gas, was observed at 1.2×10^{-7} cc/sec/cm^2/cm at 1 atmospheric pressure at 60 Celsius (Flaconneche and Klopffer, 2001).

5.3 Gamma sensitivity measurements

Using a single cell detector, gamma sensitivity was measured with a ^{137}Cs source and a ^{252}Cf source. Often neutron sources accompany significant gamma-ray activities. Also, a strong gamma source can be employed to overwhelm a detector to render its response inaccurate or useless. Therefore, it is important to understand how LiPMICs would respond with gamma sources. For the neutron-induced pulse height spectrum depicted in Fig. 35, a ^{252}Cf source was measured for 600 seconds. The sharp peak on the right side of the spectrum is an electronic pulser put in as a cursor for overall electronic health of the system. If the pulser peak broadens it is an indication that electronic noise is being introduced to the system. The effect of the electronic noise is that the baseline of electronic pulses becomes unstable and prone to register false signals. This phenomenon can sometimes happen overwhelmingly so that the detector is unresponsive to real signals. The right side of the pulse height spectrum highlighted in blue is the first 5% of the scale that will be discarded as gamma-induced pulses and electronic noises.

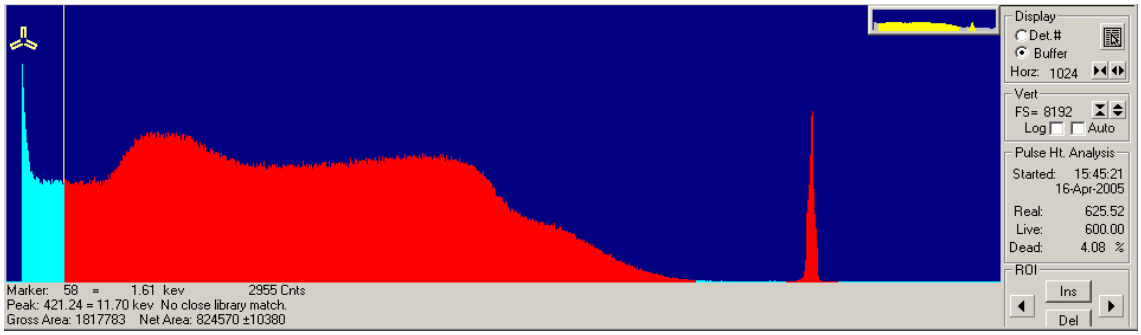

Fig. 35. Neutron induced spectrum using a Cf-252 source.

Under the same measurement conditions, a ^{137}Cs source was measured and the comparison of the two spectra is made in Fig. 36. As stated above, the gamma contribution in the spectrum fall in the first 5% of the scale (less than 2 fC), and can be effectively eliminated in the pulse height spectrum.

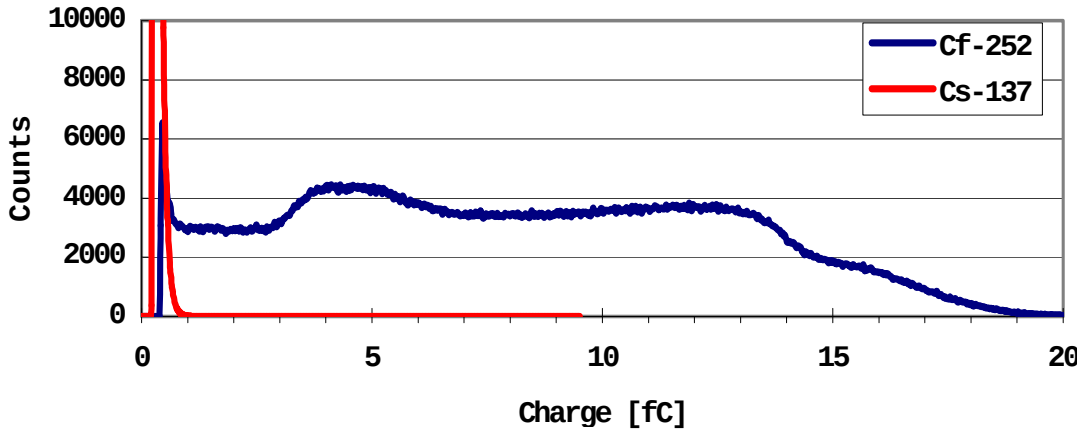

Fig. 36. Overlap of a Cf-252 spectrum with a Cs-137 spectrum. The gamma peak registered 90000 counts. The two measurements were conducted right after the other in identical measurement setup.

5.4 The effects of shaping time and susceptibility to microphonics

Initially, pulses are collected as induced charges on the anode surface. The charges are collected and integrated through a parameter called shaping time constant. Depending on the length of a shaping time constant, pulse height spectrum can take a vastly different shape as shown in Fig. 37. Ideally, one would want to collect full charges; however, this is not practical and necessary. Choosing a shaping time constant is a compromise between charge collection efficiency and reliability since longer shaping time constant can make the detector electronics more susceptible to the microphonic noises. When a longer shaping time constant is chosen, then the induced charge is given longer time to deposit its full charge before the remnant charges are thrown out. The deposition of full charge is indicated by the pulses registering in the higher charge scale in Fig. 37. A pulse height spectrum collected with 10 μsec shaping time constant shows pulses extending to the pulser peak set at 25 fC, whereas a pulse height spectrum collected with 3 μsec shaping time constant is approximately at 13 fC. As the maximum point in the scale shrinks, the more pulses are accumulated in the first 5% in the charge scale where they will be discarded as electronic noises and gamma-induced pulses. Therefore, choosing a short timing constant can significantly reduce the counts and make the detector less efficient.

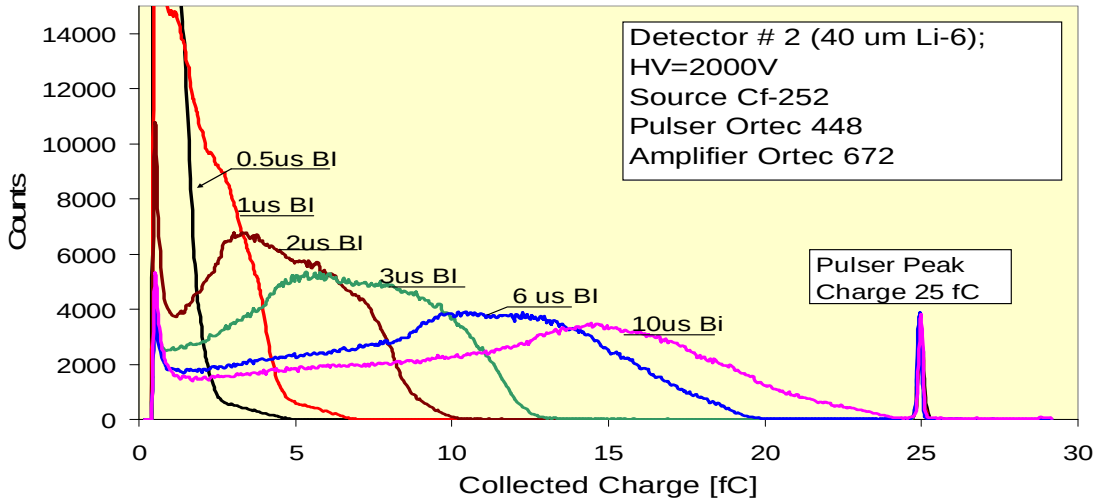

Fig. 37. The effect of shaping time on the shape of pulse height spectrum.

Fig. 38 shows the effect of shaping time in a measurement of a ^{252}Cf sources. Using the same P-10 gas as the fill-gas, three measurements using different shaping time were performed one after the other. From previous study on electric field strength analysis, it has been established that the methane concentration between 4 and 15% percent all electron drift velocity to maintain above the minimal drift velocity. For shaping time constants of 2 and 6 μsec, methane concentration has little effect, as shown in Fig. 38. However, for shaping time constant of 1 μsec, the short shaping time constant requires significant increase of high voltage bias to compensate for the slow drift velocity of the electrons. Only after 400V, 1 μsec shaping time constant can be approximately 87% of the scale normalized to the count rate taken at 800 HV with 6 μsec. On the hand, the effect of change in shaping time constant is minimized in Fig. 39. The spectra taken with various shaping time constants all registered 90% in the scale normalized to a count rate

taken with 800V at 6 μsec. This confirms the simulation results where the electric field strength of 0.065 V/cm/Torr maintains stable electron drift velocity. Fig 39 shows the largest divergence of count rates at 100V quickly diminishes near 200V, which is in close agreement with the simulation results.

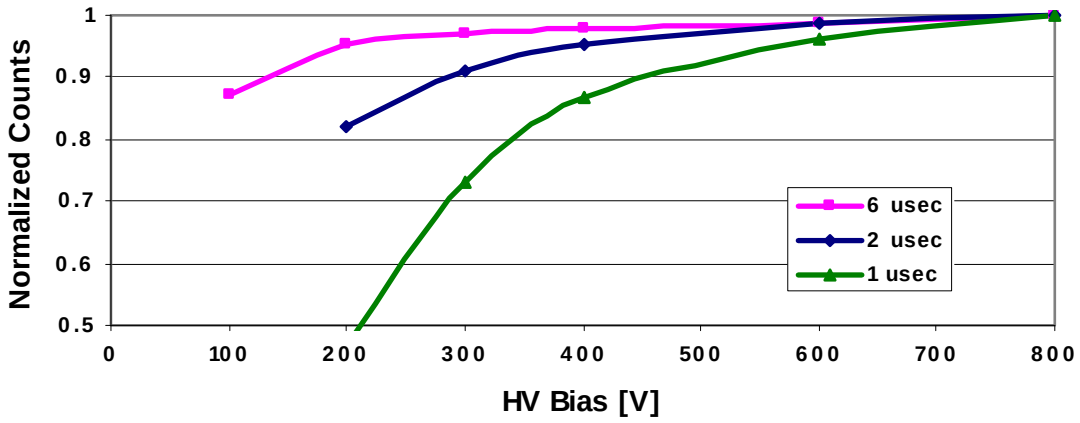

Fig. 38. Effect of shaping time on total counts with 2.5% methane concentration in argon.

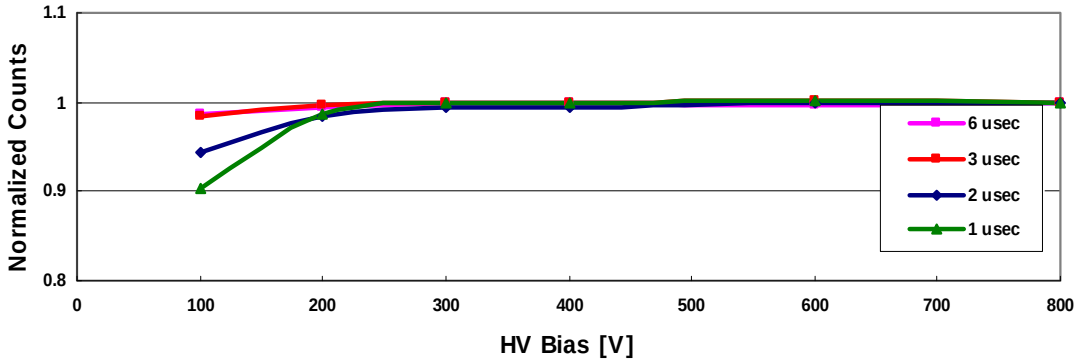

Fig. 39. Effect of shaping time on total counts with 5% methane concentration in argon.

5.5 Additional pulses from anode as a conversion reaction site

An experiment is conducted to obtain additional pulses by painting the anode surface with ^{6}LiF. As one can see in Fig. 40, despite some differences, there are several similarities between the two spectra. Both spectra share a prominent peak in the middle of the spectra. The pulses contributing to the peak are from the tritons and alpha particles that emanate from flat surface of cathode and anodes. These particles travel the similar distance, and deposit same amount of energy before hitting the cathode or anode. This phenomenon is related charged particle spectroscopy where the energy deposition by charged particle is proportional to the range it travels. Anode surface can provide approximately 20% additional pulses when painted with ^{6}LiF or laminated with ^{6}Li.

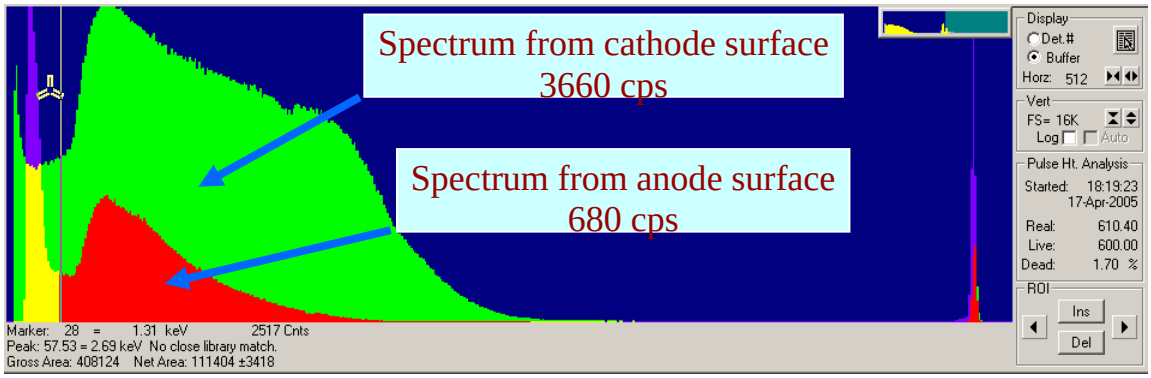

Fig. 40. Additional pulses obtained from anode surface by painting it with ^{6}LiF. The count rate is comparable to the painted surface area.

5.6 Comparison of MCNP results and experiments

MCNP results obtained from simulations performed with single cell detector models are compared (Table 5). Because MCNP does not have energy threshold, the 10% threshold

set for the actual measurements is compensated to the MCNP results by increasing their tallies by 5%. When this correction is made, the difference between MCNP results and measurements is less than 10%. The detector cell painted with LiF has approximately over 20% of relative difference, and this large difference could be attributed to the hand painting of LiF after mixing it with colloidal graphite. The uneven paint thickness could alter the detector response significantly. Overall, the agreement between MCNP results and experiments is reassuring and is a confirmation that the simulations were performed accurately.

Table 5
Comparison of MCNP simulations and measurements

	MCNP	Det.#1 (40μm Li-6)		Det.#2 (60μm Li-6)		TD.#2 (7.8μm LiF)	
Absorber Thickness	Calculated [cps]	95% ROI [cps]	Corrected to 100% [cps]	95% ROI [cps]	Corrected to 100% [cps]	95% ROI [cps]	Corrected to 100% [cps]
30 μm Li-6	1820						
40 μm Li-6	1520	1368	1436.4				
60 μm Li-6	1430			1296	1360.8		
7.8 μm LiF	910					687	722

5.7 Lithium foil lamination and detector matrix assembly

Having quantified the outgas rate and composition, a series of initial measurements were performed to establish the performance of individual detector cells, prior to obtaining the detector matrix performance as a whole. Because the 95% enriched ^{6}Li used in the detector matrix is highly reactive with moisture in the air and was assembled by hand in

a dry room in a lithium battery fabrication facility, the material can not be readily repaired at LANL. Since there was little chance that the chambers would be repaired at LANL, a need was recognized to establish a baseline measurement for each cell so that the individual performance over a period of time can be compared. Side B of the detector array was prepared first with detector electronics and was available for the baseline measurement. Figure 41 shows a can of 95% enriched ^{6}Li foil manufactured in 2003. The can was sealed with argon gas, and was in storage for the past three years.

Fig. 41. Ninety-five percent enriched lithium-6 metallization material.

Fig. 42 shows the interior surface of the detector matrix after lithium foil is manually laid out. The difference in the gleam of the surface when compared to Fig. 42 is not due to difference in lighting. Fig. 43 is the close up of the surface and patchwork of small strips of ^{6}Li foil can be seen. After ^{6}Li lamination work is finished, the detector array is assembled in a dry room (Fig. 44), and prepared for shipping to LANL. Upon arrival at LANL, the exterior of the detector array is visually inspected and was retested with helium leak detector for seal integrity. The detector array passed the test and was prepared with electronics for initial measurements.

Fig. 42. Lithium metallization is applied on the interior surface.

Fig. 43. Close-up of the lithium metallization.

Fig. 44. Fully assembled detector array with detector electronics.

5.8 Baseline measurements with detector matrix

The baseline measurements were conducted in March 2007, when the detector array arrived at LANL. First, the individual gain of the electronic boards and detector cells has been equalized using a potentiometer on the boards. Having verified that the individual detectors have the same gain, initial measurements began. An electronic pulser peak was established at 25 fC as an indicator of electronic noise level. A ^{252}Cf source was placed at the center of detector cells for 20 minutes and the spectra were recorded. Figs. 45 and 46 indicated that the there is some decrease in the charge collection between the spectra taken in March and September of 2007. While the decrease is approximately 3% of the total counts, it is a source of concern because 6 months is only 5% of the projected lifetime of the detector. Further measurements will be needed to assess the progress of contamination.

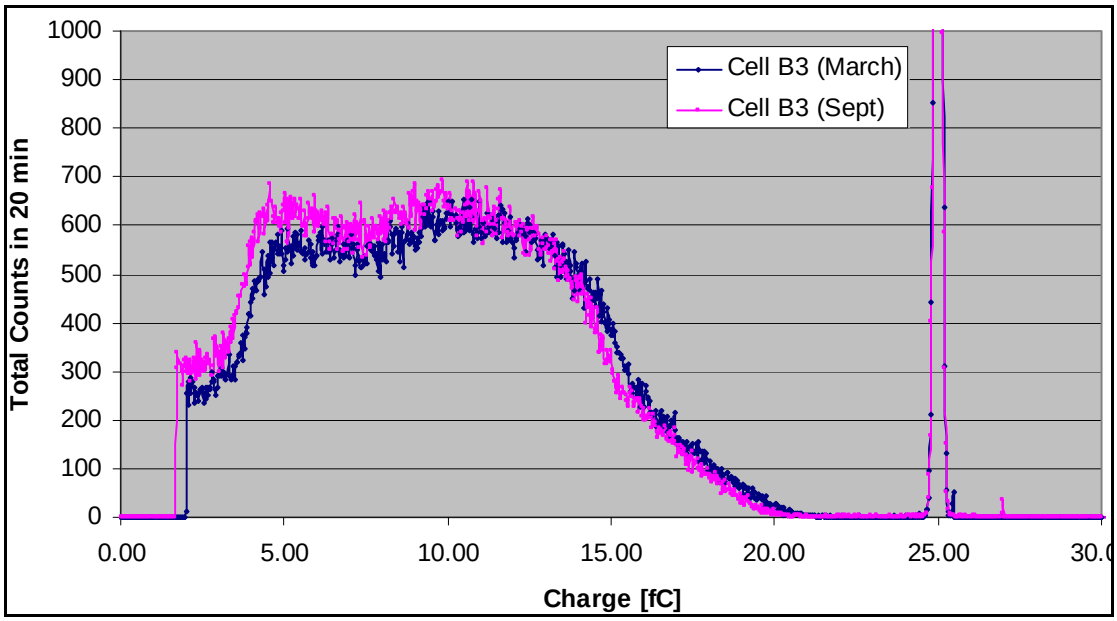

Fig. 45. Six-month comparison of cell B3 spectra.

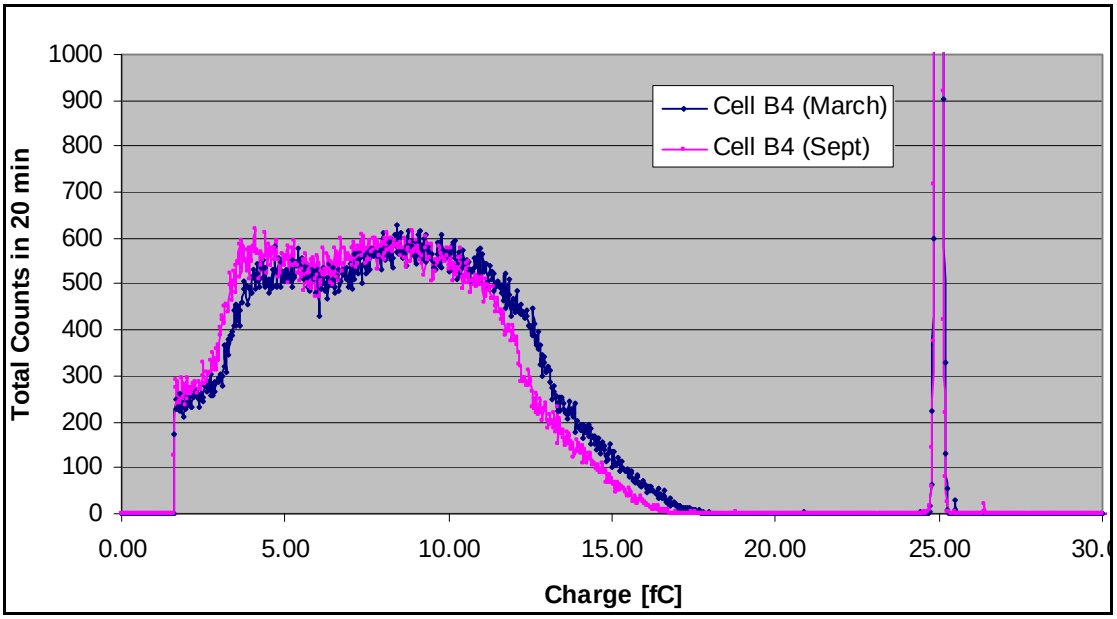

Fig. 46. Six-month comparison of cell B4 spectra.

5.9 Comparison of detector array measurement and MCNPX simulations

In order to compare the simulation results to experiments, a series of measurements were performed. Table 6 lists the data for the 7 measurements and their comparison to the simulation data. For measurements 1 through 4, the same ^{252}Cf point source was placed at the center of cell B1, B2, B3, and B4. In the MCNPX simulation, a point source of equal activity to the physical source used at the time of measurement was placed at the center of individual cells. The measurements 1 through 4 indicated close agreement with their respective simulation counterparts. The ^{252}Cf source was placed at the center of the side B for measurement 5 and for measurement 6 and 7, the source was moved out from the center of side B by 10 cm, and 50 cm, respectively. As the distance between the

source and the detector array became longer, the difference between the simulation results and measurement became more apparent.

Table 6
Comparison of MCNPX simulation and experimental results for detector matrix

No.	Measurement condition	Reaction Rate [/sec] MCNPX)	Relati-ve Error [%]	MCNPX Pulse Counts 90% ROI	Measured pulses background subtracted	Differen-ce [%]
1	Center of B1	0.081513	0.0005	25510684	23922817	6.63
2	Center of B2	0.072087	0.0006	22560657	22378119	0.81
3	Center of B3	0.072124	0.0006	22572131	23654360	-4.34
4	Center of B4	0.072189	0.0006	22592473	23757490	-4.90
5	Center of Side B, on the surface	0.072206	0.0006	22597941	22734459	-0.60
6	Center of Side B, 10 cm from surface	0.035765	0.0008	11193156	12506548	-10.50
7	Center of Side B, 50 cm from surface	0.004712	0.0023	1474809.3	1643931	-10.29

The detector array, which posed more complex problems from machining to ensuring seal integrity was put through machining, metallization, leak test, and ^{6}Li lamination. In the process, the outgas volume and component analyses were performed to ensure continuous operation would be viable. It has been determined that the detector array can operate continuously for 6 months with the outgas volume and the composition. The initial measurements with a ^{252}Cf source revealed that the individual cells had different overall gain, which was equalized with adjustable potentiometers.

Six-month comparison of the individual cells showed that there were some loss in charge collection efficiency in two of 4 cells, and it would be necessary to conduct further test to see if the degradation of the charge collection efficiency will level out in the future. Overall, the verification of MCNPX calculation has been positive, showing good agreement in all of the measurements.

6. CONCLUSIONS

A novel ^{6}Li neutron-capture pulse-mode ionization chamber was designed and optimized to replace ^{3}He proportional counters as more economical neutron detection instrumentation for the homeland security and counter-terrorism application. The novel design incorporated neutron moderator as a physical shell and electrical insulator and removed the clear separation between a neutron moderator and active volume of detectors that exists in the conventional designs of thermal neutron detectors. The separation exists in LiPMICs as an 8-μm metallization layer that serves multi-purposes as an electrode, atomic barrier against the outgas migration, and foundation for the neutron conversion site. Consequently, this brought on a fundamental disadvantage of possibly exposing the ionization chamber to outgas effects from plastic detector components. The design of LiPMIC sought to reduce the outgas effects by relying on the robust design and operating principles. The choice of HDPE as the physical shell is an obvious one because of its outstanding neutronics properties, but HDPE is also one of the most stable polymers with one of the lowest outgas rates. The outgas rate of 9.6×10^{-10} torr-liter/(cm^2-sec) was obtained during an 8-month long data collection experiment. It is approximately 2 orders of magnitude lower than published outgas rate data, 2.6×10^{-7} torr-liter/(cm^2-sec), of bare polyethylene. It is conceivable that the metallization aided in reducing the flow of outgas, but a bulk of credit can be given to the partial pressure of outgas molecules inside the polymer matching the low partial vapor pressure in the vacuum to slow down the diffusion of the outgas components (de Segovia, 1999). The

long-term outgas rate, which reflects the second, stable outgas rate of approximately 0.3 torr/month would allow approximately 10 years of continuous operation when electron dynamics were simulated using GARFIELD (Chung et al., 2005).

The composition of outgas identified with an RGA was mostly environmental species such as oxygen, water, carbon dioxide and nitrogen. The GC/MS analysis indicated there was a 10s ppb level of heavy alkanes present in the outgas. However, due to the high temperature in which the outgas was taken from the solid sample, it is expected that the LiPMIC will not operate in such high temperature nearing the melting point of HDPE.

Simulations were performed using MCNPX, GARFIELD, and OPERA. Electrostatic field configuration, neutron interaction rates, and charged particle transport in gas were the three areas where simulation and modeling were necessary for establishing baseline of research and for comparison with the experimental results. Using MCNPX, the optimized thickness of ^{6}Li metallization layer was found to be 30 μm. After several iterations, the final dimensions of the HDPE matrix thickness were 2 cm front, 8 cm back, 4 cm interlayer, 2 cm of intercell, and 4 cm of edge HDPE thickness. The effectiveness of this set of thicknesses was verified using different neutron energies ranging from 1 keV to ^{252}Cf fission neutrons. The simulation showed that the LiPMIC is equally capable of detecting 1 keV neutrons and ^{252}Cf neutrons. Using GARFIELD, the ion pair production along a triton track, time arrival distribution of electrons, and the

induced charge plots were obtained. These values were applied in setting up the operating parameters for detector electronics. GARFIELD provided critical information to mitigate the outgas effect by setting a combination of operating conditions where detector is less sensitive to the change in fill-gas composition. GARFIELD simulations of electron transport properties inside LiPMIC indicated a convergence of electron drift velocity for different concentration of methane between 0.06 and 0.09 V/cm/Torr. The electron drift velocity between 4% and 15% of methane concentration remains within 20% of 3.5 cm/μsec in the said field strength range. Having found the electric field strength where the electron dynamics were stable despite changing fill-gas composition, OPERA was used to calculate the three-dimensional electric field strength in the non-analytic geometry of LiPMIC. It was calculated that at least 160V of bias voltage would be required to keep the electric field strength above 0.06V/cm/Torr.

As designing and simulation portions of the research were completed, the detector matrix was assembled and prepared for ^{6}Li lamination. First, the machined and metallized HDPE bodies were assembled and tested for leak using ^{4}He leak testers. The detector matrix was cycled through a number of evacuation processes to remove impurities. It was then shipped to a commercial lithium battery factory and was laminated with a 50-μm ^{6}Li metallization layer. The detector matrix was tested for gamma-ray sensitivity and was found to be minimally insensitive to gamma ray sources. The influence of the gamma rays was removed by applying an energy threshold in the

detector electronics that would discard all gamma-ray induced pulses and electronic noises below the energy threshold. The shaping time constants obtain from the GARFIELD simulation results were verified with experiments and found to be in close agreement with the experiment results. With 2.5% of methane concentration in argon, it was clear that the shaping time constant of 1 μsec was not long enough to collect sufficient portion of the charges. For 5% methane concentration in argon, spectra taken with all shaping time constants, ranging from 1 to 6 μsec, had above 90% count rate of the normalized count rate. Additional count rate upto 25% could be incorporated by painting or laminating the anode surface with either ^{6}LiF or ^{6}Li metallization.

A series of long term measurements was attempted with 2 cells in the detector matrix. Cell B3 and B4 showed approximately 3% reduction in total counts over 6-month measurement period. Finally, both MCNP and MCNPX simulations of single-cell and detector matrix, respectively, were compared with measurements. For the single cell simulations, the results were about 5% different from the measurements. For simulations with detector matrix, the discrepancy between the simulations and measurements ranged from 7% to -11%. It is noted that the complexity of the detector matrix having 8 cells within a shell does give much more variation, and overall, the verification of MCNPX calculations for detector matrix has been positive, showing good agreement in all of the measurements.

REFERENCES

American Society for Testing and Materials (ASTM), 2007. Standard Test Method for Total Mass Loss and Collected Volatile Condensable Materials from Outgassing in a Vacuum Environment. ASTM E595-84.

Attix, F.H., 1986. Introduction to Radiological Physics and Radiation Dosimetry. John Wiley & Sons, Inc., New York.

Avallone, E.A., Baumeister, T., III, 1996. Marks' Standard Handbook for Mechanical Engineers, 10th Edition. McGraw-Hill, New York.

Bennett, E., Yule, T., 1972. Response functions for proton-recoil proportional counter spectrometers. Nuclear Instruments and Methods. 98, 393-412.

Biagi. S.F., 1995. Magboltz v7.1. CERN.

Capeans, M., 2003. Aging and materials: lessons for detectors and gas systems. Nuclear Instruments and Methods in Physics Research A. 515, 73-88.

Castro, E., Gonzo, E., Gottifredi, J., 1987. Thermodynamics of the absorption of hydrocarbon vapors in polyethylene films. Journal of Membrane Science. 31, 235-248.

Charpak, G., Fisher, H.G., Gruhn, C.R., Minten, A., Sauli, F., Pich, G., Flugge, G., 1972. Time degeneracy of multiwire proportional chambers. Nuclear Instruments and Methods. 99, 279-284.

Chung, K., Inakiev, K., Swinhoe, M., Makela, M., 2005. Mitigation of outgas effects in the neutron-capture ^{6}Li pulse-mode ionization chamber operation. IEEE Nuclear Science Symposium Conference Record. 3, 1255-1257.

Crank, J., 1975. The Mathematics of Diffusion. Clarendon Press, Oxford, England.

Department of Homeland Security (DHS), 2004a. Securing homeland: U.S. Department of Homeland Security strategic plan. U.S. Department of Homeland Security, Washington, DC. (http://www.dhs.gov/xlibrary/assets/DHS_StratPlan_FINAL_spread.pdf)

Department of Homeland Security (DHS), 2004b. Mission and objectives of the Directorate for Science and Technology. U.S. Department of Homeland Security, Washington, DC. (http://www.dhs.gov/xabout/structure/editorial_0530.shtm)

de Segovia, J., 1999. Physics of Outgassing. CERN Accelerator School:Vacuum Technology. 99-05, 99.

Doong, S., Ho, W.S.W., 1992. Diffusion of hydrocarbons in polyethylene. Industrial & Engineering Chemical Research, 31, 1050-1060.

Duderstadt, J., Hamilton, L., 1976. Nuclear Reactor Analysis, Wiley, New York.

Elias, H., 2003. An Introduction to Plastics, Wiley-VCH, Weinheim, Germany.

Fang, W., Shillor, M., Stahel, E., Epstein, E., Ly, C., McNiel, J., Zaron, E., 1991. A mathematical model for outgassing and contamination. SIAM Journal of Applied Math, 51, 1327-1355.

Ferguson, T., Gavrilov, G., Korytov, A., Krivchitch, A., Kuznetsova, E., Lobachev, E., Mitselmakher, G., Schipunov, L., 2002. Aging studies of CMS muon chamber prototypes. Nuclear Instruments and Methods Physics Research A. 488, 240-257

Firestone, R., Shirley, V., 1996. Table of Isotopes, 7th Edition. John Wiley & Sons, Inc., New York.

Flaconneche, B., Martin, J., Klopffer, M.H., 2001. Permeability, diffusion and solubility of gases in polyethylene, polyamide 11 and poly (vinylidene fluoride). Oil & Gas Science and Technology. 56, 261-278.

Glasstone, S., Sesonske, A., 1967. Nuclear Reactor Engineering., D. Van Nostrand Co., Inc., Princeton, NJ.

Harper, C.A., 2000. Modern Plastics Handbook., McGraw-Hill Professional, New York.

Hendricks, J., McKinney, G., 2005. MCNPX v2.5. Los Alamos National Laboratory.

Ianakiev, K., Swinhoe, M., 2002. An affordable large area neutron detector suitable for mass production. Final report for Laboratory Directed Research Development project 20020342ER, Los Alamos National Laboratory. LA-UR-03-4706.

Ianakiev, K., Swinhoe, M., Chung, K., McKigney, E., 2004. Large area neutron detector based on ^{6}Li ionization chamber with integrated body-moderator of high density polyethylene. IEEE Nuclear Science Symposium.Conference Record. 1, 456-460.

Incropera, F.P., DeWitt, D.P., 2001. Fundamentals of Heat and Mass Transfer, 5th Edition, Wiley, Boston, MA.

ICRU, 1993. Stopping powers and ranges for protons and alpha particles. Report 49, International Commission of Radiation Units and Measurements, Bethesda, MD.

Kaplan, I,, 1962. Nuclear Physics. Addison-Wesley Publishing Company, New York.

Kinsey, D., (Ed.), 1979. Evaluated Nuclear Data File Version B (ENDF/B) summary documentation, 3rd Edition. Brookhaven National Laboratory. BNL-NCS-17541.

Kiparissides, C., Dimos, V., Boultouka, T., Anastasiadis, A., Chasiotis, A., 2002. Experimental and theoretical investigation of solubility and diffusion of ethylene in semicrystalline PE at elevated pressures and temperature, Journal of Applied Polymer Science. 87, 953-966.

Kirk, R., Othmer, D., (Eds.). 2001. Encyclopedia of Chemical Technology. John Wiley & Sons, Inc., New York.

Knoll, G, 2000. Radiation Detection and Measurement. John Wiley & Sons, Inc., New York.

Kouzes, R., 2003. Homeland security instrumentation for radiation detection at seaports. Pacific Northwest National Laboratory Report PNNL-SA-43032.

Krivchitch, A., Ferguson, T., Gavrilov, G., Gratchev, V., Dalin, J.M., Kuznetsova, E., Lebedev, V., Lobachev, E., Polychronakos, V., Schipunov, L., Tchernjatin, V, 2003. Swelling phoemena in anode wires aging under a high accumulated dose., Nuclear Instruments and Methods in Physics Research A. 515, 266-277.

Kulkarni, S., Stern, S., 1983. The diffusion of CO_2, CH_4, and C_3H_8 in polyethylene at elevated pressures. Journal of Polymer Science, Polymer Physics Edition. 21, 441-465.

Lamarsh, J., Baratta, A., 2001. Introduction to Nuclear Engineering., Prentice Hall. New York.

Li, N., Long, R., 1969. Permeation through plastic films. Journal of American Institute of Chemical Engineers. 15, 73-80.

McGregor, D.S., Hammig, M.D., Yang, Y.-H., Gersch, H.K., Klann, R.T., 2003. Design considerations for thin film coated semiconductor thermal neutron detectors – I: basics regarding alpha particle emitting neutron reactive films. Nuclear Instruments and Methods in Physics Research A. 500, 272-308.

Mark, J., E., (Ed.), 1999. Polymer Data Handbook. Oxford University Press, New York.

Michaels, A., Parker, R. Jr., 1959. Sorption and flow of gases in polyethylene. Journal of Polymer Science. 41, 53-71.

Michaels A., Bixler, H., 1961. Flow of gases through polyethylene Journal Polymer Science 50, 413-439.

Michaels, A., Parker, R. Jr., 1961. Solubility of gases in polyethylene. Journal of Polymer Science 50, 393-412.

National Commission on Terrorist Attacks, 2004. The 9/11 Commission Report: Final Report of the National Commission on Terrorist Attacks Upon the United States.W. W. Norton & Company, New York.

National Nuclear Security Administration (NNSA), 2004. Defense nuclear nonproliferation: global initiatives for a more secure future. NNSA.

Neogi, P., (Ed.), 1996. Diffusion in Polymer, Marcel Dekker, Inc., New York.

Pace, R., Datyner, R., 1979a. Statistical mechanical model for diffusion of simple penetrants in polymers. I. Theory. Journal Polymer Science Polymer Physics Edition 12, 437-451.

Pace, R., Datyner, R., 1979b. Statistical mechanical model for diffusion of simple penetrants in polymers. II. Applications. – nonvinyl polymers. Journal Polymer Science Polymer Physics Edition 12, 453-464.

Pace, R., Datyner, R., 1979c. Statistical mechanical model for diffusion of simple penetrants in polymers. III. Applications –vinyl and related polymers. Journal Polymer Science Polymer Physics Edition 12, 465-476.

Peisert, A., Sauli, F., 1984. Drift and diffusion of electrons in gases. CERN Report 84-08.

Reilly, D., Ensslin, N., Smith, H. Jr., Kreiner, S., 1992, Passive Nondestructive Assay of Nuclear Materials, Report NUREG/CR-5550. US Nuclear Regulatory Commission.

Robeson, L., Smith, T., 1968. Permeation of ethane-butane mixtures through polyethylene. Journal Applied Polymer Science 12, 2083-2095.

Rogers, C., Stanett, V., Szwarc, M., 1960. The sorption, diffusion, and permeation of organic vapors in polyethylene. Journal Polymer Science 45, 61-82.

Romaniouk A., Akesson, T., Barberio, E., Bondarenko, V., Capeans, M., Catinaccio, A., Cwetanski, P., Danielsson, H., Dittus, F., Dolgoshein, B., Dressnandt, N., Ebenstein, W.L., Eerola, P., Farthouat, P., Fedin, O., Froidevaux, D., Gavrilenko, I., Grichkevitch, Y., Gagnon, P., Hajduk, Z., Keener, P.T., Kekelidze, G., Konovalov, S., Kowalski, T., Kramarenko, V.A., Laritchev, A., Lichard, P., Lundberg, B., Luehring, F., Markina, I., Manara, A., Mcfarlane, K., Mitsou, V., Muraviev, S., Newcomer, F.M., Ogren, H., Oh, S.H., Olszowska, J., Peshekhonov, V., Rembser, C., Smirnov, S., Smirnova, L.N., Sosnovtsev, V., Sutchkov, S., Tartarelli, F., Tikhomirov, V., Van Berg, R., Vassilieva, L., Wang, C., Williams, H.H., 2003. Aging studies for the ATLAS transition radiation tracker (TRT), Nuclear Instruments and Methods in Physics Research A. 515, 166-179.

Specter, G., McCollum, T., Spowart, A., 1993. Improved terbium-doped, lithium-loaded glass scintillator fibers. Nuclear Instruments and Methods in Physics Research A. 329, 223-226.

Titov, M., 2004. Radiation damage and long-term aging in gas detectors. Proceedings of the 42nd Workshop of the INFN ELOISATRON Project Innovative Detector for Supercolliders. 199-226. (http://dx.doi.org/10.1142/9789812702951_0014).

Va'vra, J., 2003. Physics and chemistry of aging – early developments, Nuclear Instruments and Methods in Physics Research Section A. 515, 1-14.

Varian Associates, Inc., 1980. Introduction to Helium Mass Spectrometer Leak Detection. Varian Associates, Inc., Palo Alto, CA.

Vector Fields, Ltd., 1999. Opera-3D^{TM} v8.7. Aurora, IL.

Veehof, R., 2005. GARFIELD. v8.01. CERN. Geneva, Switzerland.

Wolke, R., L., 1963. Range and stopping cross sections of low-energy tritons. Physics Review. 129, 2591-2596.

APPENDIX A. GARFIELD INPUT FILE

```
*=============================================================*
* GARFIELD input file for parallel plate geometry 6LiF pulse-mode ion
* chamber Kiwhan Chung
*-------------------------------------------------------------*
* Gas Composition
Global ar=95
Global ch4=5
Global gas_file `Ar`/string(ar)/`-methane`/string(ch4)

*-------------------------------------------------------------*
* Primary electron-ion pair creation
Global xori=-3.000
Global yori=0.001
Global tri=300

*-------------------------------------------------------------*
*Description of the ion chamber
&Cell
plane y  7.0  v    0.0 label S
plane y  0.0  v -250.0 label a
cell-id "Parallel Plate Ion Chamber"

*-------------------------------------------------------------*
* Compute drift-velocity, diffusion coefficients, etc.
&Gas
opt gas-plot
plot-opt drift-velocity log-x
Call inquire_file(gas_file, exist)
If exist then
        get {gas_file}
Else
        pressure 760 torr
        temperature 300 K
        magboltz argon {ar} methane {ch4} e-range 1 10000 n-e 30
        write {gas_file}
Endif

add ion-mobility 1.5e-6
heed argon {ar} methane {ch4}

*-------------------------------------------------------------*
```

```
* Plots the field lines
&Drift
int-par max-step 0.1 mc-dist-int 0.1     // integration parameter
Global ne=103053                         // total # of e produced
Global l =6.400                          // Pathlength of triton
Global phi=90.0*pi/180                   // angle of incline
Call book_histogram(ht1,100,0,6)         // tally for hitting anode
Call book_histogram(ht2,100,0,6)         // tally for all others
Call book_histogram(ht3,100,0,6)
Call book_histogram(ht4,100,0,6)
Call book_histogram(ht5,100,0,6)
area -7.5 -1. -7.5 7.5 8. 7.5            // define area of drift
Global plot=true
If plot then call plot_drift_area
For i from 1 to ne Do
   Global j=i*1000
   Global d=l*rnd_uniform
   Global x=xori+d*cos(phi)
   Global y=yori+d*sin(phi)
   call drift_electron_mc(x,y,0)
   If j<=ne then Call plot_drift_line
   Call drift_information(`time`,t,`status-code`,status)
   If status=-4 | status=-14 Then
     Call fill_histogram(ht1,t)
   elseif status=-1 Then
     Call fill_histogram(ht2,t)
   elseif status=-2 Then
     Call fill_histogram(ht3,t)
   elseif status=-3 Then
     Call fill_histogram(ht4,t)
   else
     call fill_histogram(ht5,t)
   endif
Enddo
Global plot=false
Call plot_histogram(ht1,`Time [microsec]`,`Drift time spectrum`)
Call plot_histogram(ht2, `left area`,`leftarea`)
Call plot_histogram(ht3, `too many steps`,`too many steps`)
Call plot_histogram(ht4, `abandoned`,`abandoned`)
Call plot_histogram(ht5, `Time [microsec]`,`other`)
Call plot_end
Call write_histogram(ht1,`5deg-pulse.txt`)
Call fit_gaussian(ht1,a,b,c,ea,eb,ec,`plot`)
&Field
```

```
* plot cont v
&SIGNAL
reset signals
int-par max-step 0.1 mc-dist-int 0.2     // integration parameter
area -7.5 -1. -7.5   7.5 8. 7.5               // define area of drift
select S
resolution 0 5e-3
Global plot=False
If plot then call plot_drift_area
Global l =6.400                          // Pathlength of triton
Global phi=90.0*pi/180                       // angle of incline
For i from 1 to tri Do                // number of tritons
Global d=l*rnd_uniform
Global x=xori+d*cos(phi)
Global y=yori+d*sin(phi)
Global ipn=16.911*d^5-347.03*d^4+2779.8*d^3-11413*d^2+37904*d-853.78
say "ipn: {ipn}"
Global ipnum=entier(ipn)
For ipgen from 1 to ipn do           // number of electrons simulated
call drift_electron_mc(x,y,0)          // for each triton
Call drift_information(`time`, t)
* Say "Drift time: {t} microsec"
If plot Then Call plot_drift_line
Call add_signals
* say "ipgen: {ipgen}"
Enddo
say "iteration: {i} ; {ipnum}; {ipn}"
Enddo
If plot Then Call plot_end
plot-signals
write-signal dataset "better-90deg-signal.txt" wr-if 'time>0.0&time<3.5'
&Main
&Quit
```

APPENDIX B. MCNPX INPUT FILE

```
c matrix simulation
c case 0: front 0.8" back 0.8" intercell 0.8" interlayer 0.77" edge 1.4"
c reference file
c aluminum plates are added
c source at center of cell #1
c
c === Definition of cells
c cell 1:  argon volume
1 1001 -0.0017824 (300 -301 310 -311 320 -321)
    #((310 -311 300 -303 320 -322 331):(310 -311 300 -303 323 -321 332):
    (310 -311 302 -301 320 -322 333):(310 -311 302 -301 323 -321 334):
    (300 -303 310 -312 320 -321 335):(300 -303 313 -311 320 -321 336):
    (302 -301 310 -312 320 -321 337):(302 -301 313 -311 320 -321 338):
    (300 -301 310 -312 320 -322 341):(300 -301 313 -311 320 -322 343):
    (300 -301 310 -312 323 -321 342):(300 -301 313 -311 323 -321 344):
    (300 -303 310 -312 320 -322 350):(300 -303 313 -311 320 -322 351):
    (300 -303 310 -312 323 -321 353):(300 -303 313 -311 323 -321 352):
    (302 -301 310 -312 320 -322 354):(302 -301 313 -311 320 -322 355):
    (302 -301 310 -312 323 -321 357):(302 -301 313 -311 323 -321 356))
c cell 2:  lithium layer
2 1002 -0.4592 (200 -201 210 -211 220 -221)
    #((210 -211 200 -203 220 -222 231):(210 -211 200 -203 223 -221 232):
    (210 -211 202 -201 220 -222 233):(210 -211 202 -201 223 -221 234):
    (200 -203 210 -212 220 -221 235):(200 -203 213 -211 220 -221 236):
    (202 -201 210 -212 220 -221 237):(202 -201 213 -211 220 -221 238):
    (200 -201 210 -212 220 -222 241):(200 -201 213 -211 220 -222 243):
    (200 -201 210 -212 223 -221 242):(200 -201 213 -211 223 -221 244):
    (200 -203 210 -212 220 -222 250):(200 -203 213 -211 220 -222 251):
    (200 -203 210 -212 223 -221 253):(200 -203 213 -211 223 -221 252):
    (202 -201 210 -212 220 -222 254):(202 -201 213 -211 220 -222 255):
    (202 -201 210 -212 223 -221 257):(202 -201 213 -211 223 -221 256))
    #((300 -301 310 -311 320 -321)
    #((310 -311 300 -303 320 -322 331):(310 -311 300 -303 323 -321 332):
    (310 -311 302 -301 320 -322 333):(310 -311 302 -301 323 -321 334):
    (300 -303 310 -312 320 -321 335):(300 -303 313 -311 320 -321 336):
    (302 -301 310 -312 320 -321 337):(302 -301 313 -311 320 -321 338):
    (300 -301 310 -312 320 -322 341):(300 -301 313 -311 320 -322 343):
    (300 -301 310 -312 323 -321 342):(300 -301 313 -311 323 -321 344):
    (300 -303 310 -312 320 -322 350):(300 -303 313 -311 320 -322 351):
    (300 -303 310 -312 323 -321 353):(300 -303 313 -311 323 -321 352):
    (302 -301 310 -312 320 -322 354):(302 -301 313 -311 320 -322 355):
    (302 -301 310 -312 323 -321 357):(302 -301 313 -311 323 -321 356)))
```

```
3 like 1 but trcl=2
4 like 2 but trcl=2
5 like 1 but trcl=3
6 like 2 but trcl=3
7 like 1 but trcl=4
8 like 2 but trcl=4
9 like 1 but trcl=5
10 like 2 but trcl=5
11 like 1 but trcl=6
12 like 2 but trcl=6
13 like 1 but trcl=7
14 like 2 but trcl=7
15 like 1 but trcl=8
16 like 2 but trcl=8
c poly block 1-6
c poly block was disected into 6 different pieces for reaching
c cell definition limitation
40 1004 -0.940 (130 -101 110 -111 120 -122) #1 #2 #3 #4
41 1004 -0.940 (130 -101 110 -111 122 -121) #5 #6 #7 #8
42 1004 -0.940 (100 -130 110 -111 120 -122) #9 #10 #11 #12
43 1004 -0.940 (100 -130 110 -111 122 -121) #13 #14 #15 #16
c air volume (volume that contains source, external to the detector volume)
47 0 (-131 132 110 -111 120 -121)
c aluminum plates
48 1005 -2.700 (101 -132 110 -111 120 -121)
49 1005 -2.700 (133 -100 110 -111 120 -121)
c outer universe (void)
50 0 (-133:131:-110:111:-120:121)

c === Surface cards
c =outer HDPE box
100 pz -15.41780    $ bottom-most PS (poly surface)
101 pz 5.8420     $ top-most PS
110 px -9.9060     $ outer-most PS in -x direction
111 px 24.6380    $ outer-most PS in +x direction
120 py -9.9060     $ outer-most PS in -y direction
121 py 24.6380     $ outer-most PS in +y direction
122 py 7.36600      $ boundary CELL surface in y direction
123 py 24.6380     $ redundant outer-post PS
130 pz -4.7879     $ boundary CELL surface in z direction
131 pz 7.152        $ top surface including the source
132 pz 7.1420      $ Al surface closest to the source
133 pz -16.71780    $ surface of bottom al plate piece
c
```

```
c =surface between HDPE and lithium layer 1
200 pz -3.810
201 pz 3.810
202 pz 2.540 $corner
203 pz -2.540 $corner
210 px -6.350
211 px 6.350
212 px -5.080 $corner
213 px 5.080 $corner
220 py -6.350
221 py 6.350
222 py -5.080 $corner
223 py 5.080 $corner
c cylinder surfaces parallel to x-axis
231 c/x -5.080 -2.540 1.270
232 c/x 5.080 -2.540 1.270
233 c/x -5.080 2.540 1.270
234 c/x 5.080 2.540 1.270
c cylinder surfaces parallel to y-axis
235 c/y -5.080 -2.540 1.270
236 c/y 5.080 -2.540 1.270
237 c/y -5.080 2.540 1.270
238 c/y 5.080 2.540 1.270
c cylinder surfaces parallel to z-axis
241 c/z -5.080 -5.080 1.270
242 c/z -5.080 5.080 1.270
243 c/z 5.080 -5.080 1.270
244 c/z 5.080 5.080 1.270
c spheres
250 s -5.080 -5.080 -2.540 1.270
251 s 5.080 -5.080 -2.540 1.270
252 s 5.080 5.080 -2.540 1.270
253 s -5.080 5.080 -2.540 1.270
254 s -5.080 -5.080 2.540 1.270
255 s 5.080 -5.080 2.540 1.270
256 s 5.080 5.080 2.540 1.270
257 s -5.080 5.080 2.540 1.270
c
c surface between lithium and argon 1
300 pz -3.805
301 pz 3.805
302 pz 2.535 $corner
303 pz -2.535 $corner
310 px -6.345
```

```
311 px 6.345
312 px -5.075 $corner
313 px 5.075 $corner
320 py -6.345
321 py 6.345
322 py -5.075 $corner
323 py 5.075 $corner
c cylinder surfaces parallel to x-axis
331 c/x -5.075 -2.535 1.270
332 c/x 5.075 -2.535 1.270
333 c/x -5.075 2.535 1.270
334 c/x 5.075 2.535 1.270
c cylinder surfaces parallel to y-axis
335 c/y -5.075 -2.535 1.270
336 c/y 5.075 -2.535 1.270
337 c/y -5.075 2.535 1.270
338 c/y 5.075 2.535 1.270
c cylinder surfaces parallel to z-axis
341 c/z -5.075 -5.075 1.270
342 c/z -5.075 5.075 1.270
343 c/z 5.075 -5.075 1.270
344 c/z 5.075 5.075 1.270
c spheres
350 s -5.075 -5.075 -2.535 1.270
351 s 5.075 -5.075 -2.535 1.270
352 s 5.075 5.075 -2.535 1.270
353 s -5.075 5.075 -2.535 1.270
354 s -5.075 -5.075 2.535 1.270
355 s 5.075 -5.075 2.535 1.270
356 s 5.075 5.075 2.535 1.270
357 s -5.075 5.075 2.535 1.270
c

c === transformation
c 'intercell' spacing change requires x and y transformation change
c interlayer spacing change requires z transformation change
c first layer transformation
tr2 14.732 0 0
tr3 0 14.732 0
tr4 14.732 14.732 0
c
c second layer transformation
tr5 0 0 -9.5758
tr6 14.732 0 -9.5758
```

```
tr7 0 14.732 -9.5758
tr8 14.732 14.732 -9.5758
c
c === material ===
M1001 18000 1
M1002 03006 1
c M1003 07000 0.78084
c      08000 0.20946
c     18000 0.00934
M1004 01001 0.66667
     06000 0.33333
M1005 13000 1
c
IMP:n 1 1 1 1 1 1 1 1 1 1 1 1 1 1 1 1 1 1 1 1 0
SDEF pos=0 0 7.1421 ERG=d1 $  vec 0 0 -1 dir 1
SP1 -3 1.18 1.03419
c si2 -7.353 34.765
c sp2  0 1
c si3 -7.353 34.765
c sp3  0 1
F4:N 2 4 6 8 10 12 14 16 T
FM4 -1 1002 105
sd4 1 1 1 1 1 1 1 1
E0 0.1 28I 3.0 100.
c ctme 10
print
NPS 50000000
```

VITA

Name:	Kiwhan Chung
Address:	212 Rover Blvd Los Alamos, NM 87544 USA
Email Address:	kiwhan@gmail.com
Education:	B.A., Physics, Berea College, 1992 M.S., Health Physics, Texas A&M University, 1997 Ph.D., Nuclear Engineering, Texas A&M University, 2008